November 2015

How to Build a Spinal Cord: Exploring Radial Glial Proliferation and their Contribution to Embryonic Neurogenesis

Kimberly A. Johnson
University of Massachusetts - Amherst

HOW TO BUILD A SPINAL CORD: EXPLORING RADIAL GLIAL PROLIFERATION AND THEIR CONTRIBUTION TO EMBRYONIC NEUROGENESIS

A Dissertation Presented

by

KIMBERLY A. JOHNSON

Submitted to the Graduate School of the
University of Massachusetts Amherst in partial fulfillment
of the requirements for the degree of

DOCTOR OF PHILOSOPHY

September 2015

Molecular and Cellular Biology Program

HOW TO BUILD A SPINAL CORD:
EXPLORING RADIAL GLIAL PROLIFERATION AND THEIR CONTRIBUTION TO EMBRYONIC NEUROGENESIS

A Dissertation Presented

by

KIMBERLY A. JOHNSON

Approved as to style and content by:

_____
Michael J.F. Barresi, Chair

_____
Rolf Karlstrom, Member

_____
Gerald Downes, Member

_____
Patricia Wadsworth, Member

_____
Elizabeth Dumont, Director
Interdepartmental Graduate Programs, CNS

ACKNOWLEDGMENTS

I am extremely grateful to my advisor Dr. Michael Barresi for all of his guidance and support throughout my graduate career. Thank you for giving me the opportunity to work in your lab, for believing in me, and for teaching me so much over the years.

The work presented herein would not have been possible without the tremendous contributions from many undergraduate students in the Barresi Lab. Special thanks to Chelsea Moriarty, Alissa Ortman, Kristina DiPietrantonio, Brittany Edens, Jean Eisenman, Sally Krikorian, and Jessica Barragan for their work on the Kif11 project. Special thanks to Sarah Bashiruddin, Jessica Barragan, Carla Vélez, Catalina Sakai, Katrina Anderson, and Rachael Stein for their work on completing the Ablation studies. Thank you to Narendra Pathak and Caitlin Schneider for their contributions and support during the final manuscript process.

I am thankful for our many collaborators over the years that helped make this study successful. Special thanks to Dr. Nessy Tania and Dr. Christophe Golé for generating the Mathematical Model of Neurogenesis, and for the long hours of wonderful conversation spent trying to make sense of our data. Thank you to Rosemarie Doris, Dr. Stephen Devoto, and Dr. Michael Parsons for generating the *gfap:nls-mCherry* and the *gfap:nfsb-mCherry* constructs, which was essential for completing this project. Thank you to Dr. Jeff Mumm for his continued guidance with the *nfsb* constructs and on our publications. Thank you to Dr. Cody Smith and Dr. Sarah Kucenas for collaborating with us and performing the immune cell analyses in the Ablation studies. I would also like to

thank Chelsea Tyrrell and Dr. Gerald Downes for conducting the behavioral analyses affiliated with the Ablation studies.

Thank you to my committee members, Dr. Rolf Karlstrom, Dr. Gerald Downes, and Dr. Patricia Wadsworth for your guidance throughout my graduate career and for my post-graduate decisions. You challenged me to think more critically about the science, and have made me a better researcher because of it.

Finally, I am very thankful to my friends and my family for supporting me throughout my graduate studies. I would not have made it through without you all rooting for me for the last seven years! I am grateful for the support of my parents throughout this process, I know it was a long one but you were there for me the whole way. I am thankful for the support of the wonderful faculty and students from Smith College and Bay Path College. Lastly, I am grateful for Amber Lecistis, Ketan Mathavan, Karan Hingorani, Adam Chu, Jen Lin, and Jesse Angelo, whose friendships have been unparalleled and I wish you all the best!

ABSTRACT

HOW TO BUILD A SPINAL CORD: EXPLORING RADIAL GLIAL PROLIFERATION AND THEIR CONTRIBUTION TO EMBRYONIC NEUROGENESIS

SEPTEMBER 2015

KIMBERLY A. JOHNSON, B.S., BAY PATH COLLEGE

M.S., SMITH COLLEGE

Ph.D., UNIVERSITY OF MASSACHUSETTS AMHERST

Directed by: Dr. Michael J.F. Barresi

During embryonic neural development, the concerted actions of neural stem cells (NSCs) populate and pattern the tissues that will give rise to the brain and spinal cord. This heterogeneous NSC population initially consists of neuroepithelial cells, which will generate the first neurons present in the central nervous system (CNS) prior to transitioning into radial glial cells. Classically, radial glial cells are known to play a wide range of roles during CNS development, from maintaining neuronal homeostasis, as a scaffold for neuronal migration, and as a permissive growth substrate for directed axon pathfinding. Recently, radial glial cells have been proposed to also act as a progenitor population for neuronal and glial progenies. Despite their presumed importance, we still lack a foundational understanding of radial glial development and their requirement during development of the central nervous system (CNS). To answer this, I have used genetic and pharmacological approaches to visualize and manipulate radial glial cells throughout embryonic neurogenesis using the zebrafish model system, which maintains radial glia throughout embryonic and adult life. The results of this study demonstrate that radial glia expressing Glial fibrillary acidic protein (Gfap) additionally express NSC

markers, are proliferative, and are required to generate late-embryonic neurons and glial cells. This study also provided support for a radial glial requirement in proper neuronal and axon patterning, maintenance of the blood brain barrier, and for a novel role in locomotor behavior. Use of the approaches herein also lead to the identification of a novel, non-radial glial NSC population in the embryonic spinal cord that warrants further study. Taken together, our multifaceted approach supports a role for *gfap*+ radial glia representing the major neural stem cell during late embryogenesis for specific lineages, and possessing diverse roles to sustain the structure and function of the spinal cord. We predict that these new tools will additionally prove powerful to both exemplify the important roles astroglia are historically suspected in as well as reveal novel roles during development, physiology, and regeneration.

TABLE OF CONTENTS

Page

LIST OF TABLES

Table Page

LIST OF FIGURES

Figure Page

CHAPTER 1

INTRODUCTION

Development of the central nervous system (CNS) from embryonic tissues into the billions of cells that comprise the adult brain and spinal cord is the result of neural stem cell division (NSC). To do so, NSC division and differentiation must be tightly regulated throughout embryonic development in order to generate the proper amount of neurons and glial cells required to establish a functional nervous system. Understanding regulation of cell division and differentiation is not only applicable to developmental biology, but also to disorders of the CNS. Reductions in NSC divisions are implicated in the developmental origins for microcephaly and schizophrenia, whereas dysregulated NSC divisions is linked developmentally to megalocephaly, autism, and seizure disorders as well as tumorigenesis in congenital and adult neural tissues (Verity et al., 2003; Sanai et al., 2005; Reif et al., 2006; Le Belle et al., 2014). Therefor, it is essential to possess a fundamental understanding of the NSC populations present in the developing CNS, how they develop, and how they are regulated to generate the diverse cell types present throughout neural tissues.

1.1 NSC divisions shape CNS development

CNS development begins through the induction of a flat sheet of neuroectodermal cells to proliferate and undergo morphological changes to convert into a neural tube in a process known as neurulation (Figure 1.1). During the earliest stages of this process the neural tissue is only one cell layer thick and comprised of neuroepithelial cells, which

serve as the first NSC population in the CNS. These cells express the NSC markers Nestin and Sox1/2/3 (Hockfield & McKay 1985; Dahlstrand et al., 1995; Graham et al., 2003; Ellis et al., 2004) and a polarized epithelial morphology, possessing a basal surface contacting the pial surface and an apical endfoot that contacts the lumen or ventricle. The lumen or ventricle is a space centered at the midline of the developing neural tube important for the diffusion of cell signaling molecules into the neural tube by surrounding tissues to regulate neural stem/progenitor cell proliferation and neural tube patterning through generation of region specific progeny. The area surrounding the lumen is termed the ventricular zone, a highly proliferative area where NSC populations are predominantly localized (Ciruna et al., 2006; Copp et al., 2003; Watters, 2006) and the localized environment around the lumen is responsible for maintaining multipotency (Ohnuma & Harris, 2003). Here, morphogen signals secreted through the central canal act directly on cells adjacent to this opening, regulating the duration of their cell cycle and promoting multipotency over differentiation (mechanisms reviewed in Ohnuma & Harris, 2003).

The first rounds of divisions that neuroepithelial cells undergo are unsynchronized symmetric divisions to amplify the progenitor pool and resulting in a densely packed tissue (Tawk et al., 2005; Kriegstein & Alvarez-Buylla, 2009; Latasa et al., 2009). To accommodate the increase in neural progenitors, neuroepithelial cells undergo dynamic cell movements throughout the cell cycle to displace the nucleus basally to allow cells undergoing division at the luminal surface in a process termed interkinetic nuclear migration (Latasa et al., 2009). These stereotyped movements span the apical-basal boundaries of the neural tissue as it forms the neural plate, placing the neuroepithelial

nucleus at the pial surface during S-phase and migrating back towards the lumen for M-phase (Figure1.3) (Alexandre et al., 2010; Latasa et al., 2009; Leung et al., 2011). Once the progenitor pool is established, neuroepithelial cells initiate neurogenesis by producing the first neuronal populations throughout the CNS (Figure 1.2; reviewed in Kriegstein & Alvarez-Buylla, 2009).

Following the initiation of neurogenesis, neuroepithelial cells transform directly into radial glial cells through upregulation of glial markers such as glial fibrillary acidic protein (Gfap), brain lipid binding protein (BLBP) or the glutamate aspartate transporter (GLAST) (Bignami & Dahl, 1977; Zhang, 2001; reviewed in Gotz & Huttner, 2005; Kriegstein & Alvarez-Buylla, 2009). Radial glia conserve many characteristics of their neuroepithelial progenitors, such as retention of neural progenitor markers (Lam et al., 2009; Jao et al., 2012; Briona & Dorsky 2014), maintenance of apical-basal polarity (Gotz & Huttner, 2005), and display interkinetic nuclear migration to the luminal surface prior to division (Alexandre et al., 2010; Gotz & Huttner, 2005; Leung et al., 2011). Unlike neuroepithelial cells, radial glial nuclei are confined to the ventricular zone (an area adjacent to the lumen or ventricle) instead of spanning the full width of the neural tissue.

After neuroepithelial cells have generated the first set of neurons, radial glia will then act as a main multipotent progenitor for the duration of embryonic neurogenesis (Figure 1.2, 1.4A). Radial glial cells have the capacity to self-renew as well as producing either a differentiated neuronal daughter or an intermediate progenitor cell that will ultimately generate a neuronal fate (nIPC; Figure 1.2; reviewed in Kriegstein & Alvarez-Buylla, 2009). Following cessation of embryonic neurogenesis, radial glial cells become

gliogenic and generate a variety of glial populations in the CNS, such as astrocytes or oligodendrocytes (Barry & McDermott, 2005; Hirano & Goldman, 1988; Choi & Kim 1985; Fogarty et al., 2005; Kim H et al., 2008b). Much like neurogenesis, radial glia can contribute to gliogenesis directly (direct transitioning into astrocytes) or indirectly into oligodendrocytes through generation of oligodendrocyte progenitor cells (OPCs) (Kim et al., 2008b). These glial populations serve neuroprotective roles during CNS development, either by promoting homeostasis and mediating synaptic output (astrocytes) or by myelination of neuronal axons to promote signal transduction (oligodendrocytes) (Ullian et al., 2001; Demerens et al., 1996). Following cessation of embryonic development, radial glia transition into astrocytes, ependymal cells, or B cells, which will then act as the NSC population throughout adult life in most vertebrates (Figure 1.2) (Kriegstein & Alvarez-Buylla, 2009).

1.2 Defining radial glia as a NSC population

In order to be defined as a neural stem population, a cell must be able to display several characteristics of traditional stem cells; NSCs should have the capacity to proliferate and self renew, and exhibit multipotency through generating multiple cell types within neural tissue (Pevny & Nicolis, 2010). Confirmation of a multipotent fate for radial glia was first determined through fluorescent activated cell sorting (FACS) of murine cells expressing human GFP-tagged radial glial marker Gfap and identified that small clonal populations of Gfap-expressing radial glia had the ability to generate neurons and astrocytes (Malatesta et al., 2000). Since then, astroglial populations (comprised of radial glia and astrocytes) in the cerebral cortex have been well defined as

self-renewing stem cells with neurogenic and gliogenic potential (Figure 1.4A) (Malatesta et al., 2000; Noctor et al., 2002; and reviewed in Ihrie and Alvarez-Buylla, 2008; Pinto and Gotz, 2007).

Despite this evidence, defining radial glia as a progenitor population has been a challenge, and a unified hypothesis on radial glial roles in neural development throughout vertebrate species is still lacking. This is due largely to the availability of markers to distinguish between embryonic and mature radial glia and regional differences in neurogenesis throughout the neural tube. In the mouse spinal cord, appearance of Gfap+ radial glia was found after the first neurons were produced, reaffirming the notion that spinal cord radial glia do not participate in spinal cord neurogenesis (Barry & McDermott, 2005). Instead, Gfap+ radial glia in the spinal cord were demonstrated to be exclusively gliogenic and solely produced oligodendrocytes and astrocytes (Choi et al., 1985; Leber & Sanes, 1995; Hirano & Goldman 1988; Fogarty et al., 2005). Challenges to this dogma have arisen in recent years, where use of more sophisticated fate mapping using Cre-recombinase identified *blbp*+, *nestin*+ radial glial populations are present throughout the brain and spinal cord during neurogenesis in mice (Anthony et al, 2004), suggesting that radial glia are present at the right time in development to be contribute to neurogenesis. Therefor, a comprehensive analysis of radial glial biology including timing of emergence, regulation of division, and a test of multipotency is required to further our understanding of NSCs and CNS development.

1.3 Structural roles of astroglia

Classically, radial glia have been best characterized for their roles as a structural support and patterning element of the neural tube. In the cerebral cortex, radial glial cells are present during or after neurogenesis to support the migration of newly born neurons radially out of the ventricular zone and towards the pial surface (Figure 1.4B) (Gasser & Hatten, 1990; Noctor et al., 2002; Barry et al., 2014). During commissure formation, subsets of radial glia act as a permissive growth substrate for growing axons in the forebrain (Marcus & Easter 1995, Barresi et al., 2005). In the spinal cord, BLBP+ radial glial fibers actively restrict and guide developing corticospinal axons, acting as functional barriers to prevent crossing into the other side of the spinal cord (Barry et al., 2013) or as highly organized structural "corridors" to direct and manage developing corticospinal axon tracts (Figure 1.4C,D) (Brusco et al., 1995; Barry et al., 2013). Electron microscopy techniques have observed growth cones of pioneering corticospinal axons interacting directly with radial glial fibers, suggesting a chemical guidance system as well as a structural role (Joosten & Gribnau, 1989). These programs can be upregulated in postembryonic tissue following injury, where radial glia have been shown to facilitate regeneration forming radial glial scaffolds to promote axonal regeneration and neurogenesis in the brain and spinal cord (Briona & Dorsky 2014, Goldshmit et al 2012, Kroehne et al., 2011).

Additionally, radial glia maintain neuronal health and homeostasis by regulating formation and function of the blood brain barrier (BBB). Embryonic radial glia directly contact and provide tracts to guide angiogenic sprouts to help form the BBB (Gerhardt et al., 2004; Noctor et al., 2001) and regulate vascular proliferation, angiogenesis, and functional integrity throughout development into adulthood (McCarty et al., 2005;

reviewed in Alvarez, 2013). In the developing mouse brain, radial glia were shown to directly regulate angiogenesis through inhibition of Wnt signaling in endothelial cells of blood vessels to ultimately shape the developing vascular network of the blood brain barrier (Ma et al., 2013). Disruptions in these radial glial-vascular connections during neurogenesis were shown to lead to hemorrhagic lesions throughout the embryonic brain and spinal cord, motor defects, axonal deterioration in the brain and spinal cord, ataxia and death (McCarty et al., 2005; Ma et al., 2013).

1.4 A model system for studying radial glial dynamics during neural development

Testing a requirement of radial glia for these diverse functions presents a challenge and necessitates the use of a well-established organism of vertebrate neural development. The zebrafish, *Danio rerio*, is a robust model system with a highly simplified CNS containing many of the same NSC, neuronal, and glial populations as mammals (Appel & Chitnis, 1995; Lewis and Eisen, 2003). Neurogenesis is exceptionally quick in zebrafish, with induction of neural tissue by 6hpf (hours post fertilization) to a fully functioning nervous system by 24hpf (reviewed in Schmidt et al., 2013). Importantly, zebrafish not only possess radial glia throughout embryonic development but also retain radial glia into adult life, with little evidence supporting that they generate astrocytes in adult zebrafish (Grandel & Brand 2013; Suter et al., 2009, Kawai et al., 2001).

Although zebrafish neural development shares many of the same characteristics as mammalian counterparts, the cellular markers used to differentiate embryonic NSC populations differs quite dramatically. In zebrafish, there is currently no marker specific

to neuroepithelial cells, as both radial glia and neuroepithelial cells have been shown to share some of the earliest NSC markers Nestin and Sox2/3 (Lam et al., 2009; Briona & Dorsky 2014, Briona et al., 2015). Neuroepithelial cells instead have been identified through retention of a columnar morphology using general markers labeling membranes (Alexandre et al., 2010; Tawk et al 2007), instead of the elongated, bipolar morphology typical of radial glia. Radial glia, however, can be identified through many of the standard markers observed in mammalian systems, although expression of these markers happens considerable earlier in zebrafish neural development. The best-characterized marker in zebrafish is Gfap, and expression of this marker has been viewed as early as 10hpf by *in situ* hybridization and transgenic expression by fusion to GFP (Kim et al., 2008b; Bernardos & Raymond, 2006) and coincident with the generation of the first neuronal populations in the CNS (Lewis et al., 2003). Expression of additional radial glial markers (*blbp*, *slc1a3a/glast*, *s100β* and *vimentin*) have been demonstrated to be present throughout the embryonic zebrafish CNS at 24hpf (Thisse & Thisse, 2008; Kim et al., 2008a; Rauch et al., 2003), however earlier expression patterns have not been observed. Regardless, observations made in zebrafish support that radial glia are present in the nervous system at a time that would support a role in neurogenesis as similarly observed in mouse (Anthony et al., 2004), and a wealth of markers/transgenic lines exist to further test the roles of radial glia on neural development.

Within the last decade, several studies have been conducted in zebrafish to determine the roles radial glia maintain during embryonic CNS development. Support for structural roles have been demonstrated through the direct interactions of neuronal axons and radial glial fibers. In the embryonic forebrain, formation of a Gfap+ radial glial

"bridge" spanning the midline of the forebrain precedes axon pathfinding events, and promote commissure formation to connect the two halves of the CNS (Barresi et al., 2005). Studies utilizing transgenic lines to labeling radial populations globally (*gfap*; Bernardos & Raymond, 2006) or in specific domains along the dorsoventral axis (*dbx1a*; Briona & Dorsky, 2014; *olig2*; Shin et al., 2003) have observed retention of the transgene in differentiated neuronal and oligodendroglial cells, supporting a role for radial glia acting as a multipotent cell type in the embryonic CNS. Recently, several zebrafish mutants have been identified that significantly impact radial glial organization, number, or patterning with affiliated axon defects, suggesting a novel pool of genes that potentially regulate radial glial development and function (Barresi et al., 2010). Adult and larval injury models have further demonstrated that radial glia act as a reactive proliferative population in the telencephalon and spinal cord (Briona & Dorsky 2014, Goldschmidt et al., 2012), suggesting this population retains stem-like capabilities as well as structural roles well into adult life. Support for this stems from the observations that in response to injury, radial glia respond by upregulating the NSC markers Nestin and Sox2, actively proliferate, and bridge the regenerating tissue to promote axon regrowth (Briona & Dorsky 2014, Goldschmidt et al., 2012). The observations in these studies support a role for radial glia as a structural and stem cell population during embryonic development and maintenance of the CNS following injury, and further demonstrate how powerful the zebrafish model system is for studying radial glial biology.

1.5 Statement of Dissertation

Radial glial cells are implicated in a wide range of roles during vertebrate central nervous system (CNS) development, including maintaining neuronal homeostasis, providing a scaffold for neuronal migration and axon guidance, and serving as progenitor cells for specific neuronal and glial lineages. Surprisingly while these roles of radial glia are generally supported, little work has been done to directly test the requirement of radial glia for these and other processes during CNS development or for its function. Their role in spinal cord development is less understood as compared to development of the brain, and much still remains to be discovered about the mechanisms controlling radial glial proliferation and the specific neuronal and glial cell lineages radial glia create.

In Chapter 2 of this dissertation, the timing and requirement for radial glial divisions during neural tube development will be explored. Here, loss of the mitotic kinesin Kif11 will be presented as a novel tool to disrupt radial glial divisions and investigate the impact loss of division has on neural development. Furthermore, our findings will propose an indirect role for radial glia as a progenitor population in the spinal cord. In subsequent chapters, the direct roles of radial glia will be assayed through development and characterization of two novel radial glial transgenic lines. In Chapter 3, development of a nuclear-localized radial glial transgenic will be used to investigate stem-like characteristics, such as proliferation and multipotency, of the radial glial population. The findings in this chapter will also have implications on radial glial development during maturation of the zebrafish spinal cord. In Chapter 4, the direct requirement for radial glial cells during neural development will be assayed. Here, generation of a novel radial glial ablation line will be characterized on its ability to remove radial glial cells from the neural tube, and changes in NSC populations, lineage,

and spinal cord structure will be assayed. The final chapter will relate the findings of each chapter together to provide a foundational understanding of radial glial development and their requirement during development of the CNS, and further discuss how these tools will impact future studies of radial glial development.

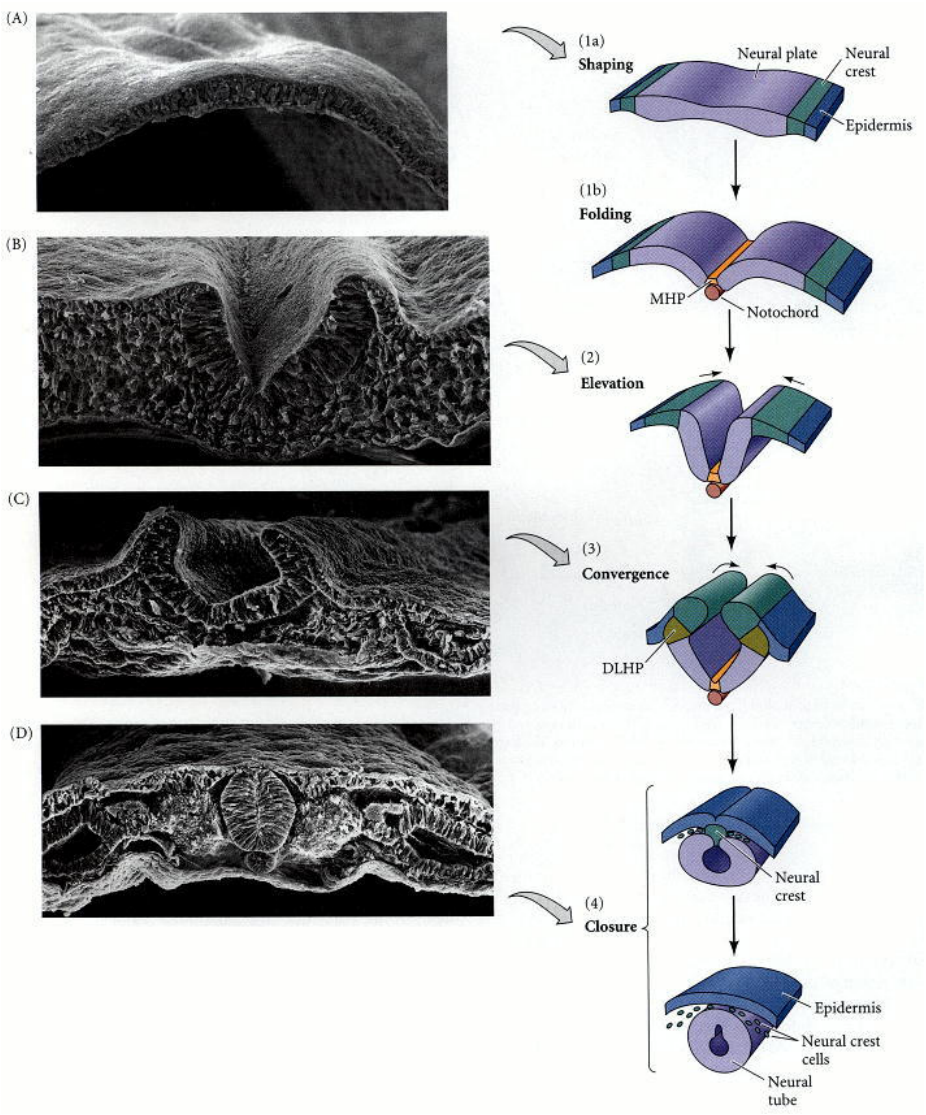

Figure 1.1. Formation of the embryonic neural tube. (A-D) SEM images of primary neurulation in the chick embryo (left) with corresponding schematics (right). (A,1) Neurulation begins with initiation of a flat sheet of neural tissue (neural plate) dorsal to the notochord to fold along the medial hinge point (MHP). (B,2) The neural folds elevate and continue to move towards the midline. (C,3) The neural folds converge due to formation of the dorsolateral hinge point (DLHP). (D,4) Neural folds contact one another and form the neural tube. Neural crest cells delaminate and separate the outer ectoderm from the neural tube. Figure from Gilbert SF, Developmental Biology, 6th Edition, 2000.

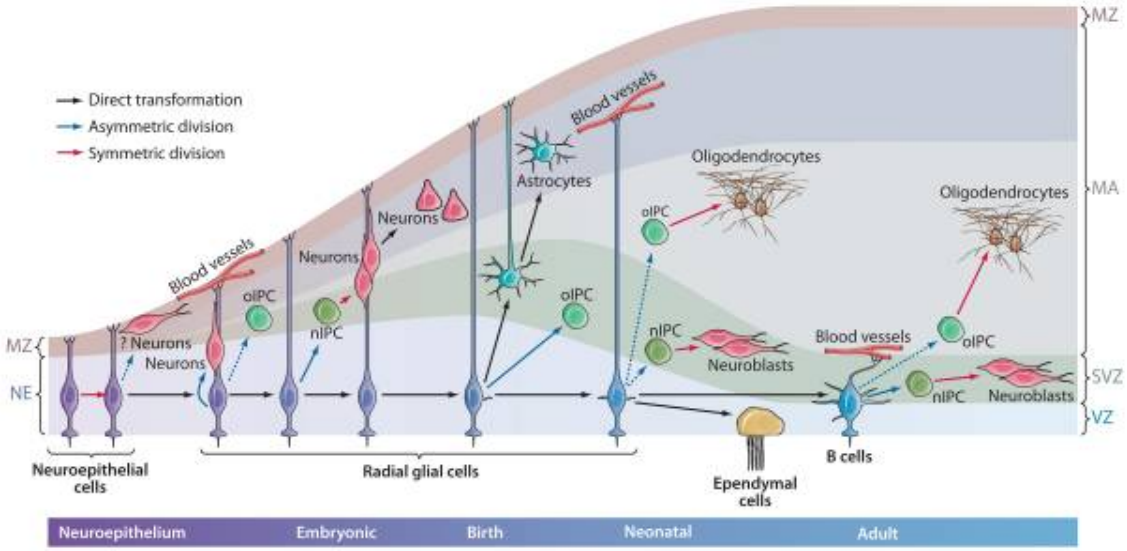

Figure 1.2. Schematic illustrating neural stem cells and progeny generated during vertebrate development. Neuroepithelial cells (purple) first undergo symmetric division to self amplify prior to generating the first neurons (pink) in the nervous system through asymmetric division. Neuroepithelial cells then directly transform into radial glial cells (dark blue), whose cell body is maintained in the ventricular zone (VZ) while extending a long pial fiber that contacts the pial surface and interacts with blood vessels. Radial glia are multipotent and undergo several divisions to self renew, generate neurons, and produce intermediate progenitor cells (IPC) for either oligodendroglial (oIPC, teal) or neuronal (nIPC, green) lineages. In postembryonic stages, radial glia undergo gliogenesis and either continue to give rise to oIPCs which generate oligodendrocytes (brown), or transform directly into astrocytes (light blue), ependymal cells (ciliated, yellow), or B cells (blue). B cells represent adult neural stem cells in subventricular zones (SVZ), maintain contact with blood vessels, and continue to produce IPCs to generate oligodendrocytes and neurons in adult neural tissues. Figure from Kriegstein & Alvarez-Buylla, 2009.

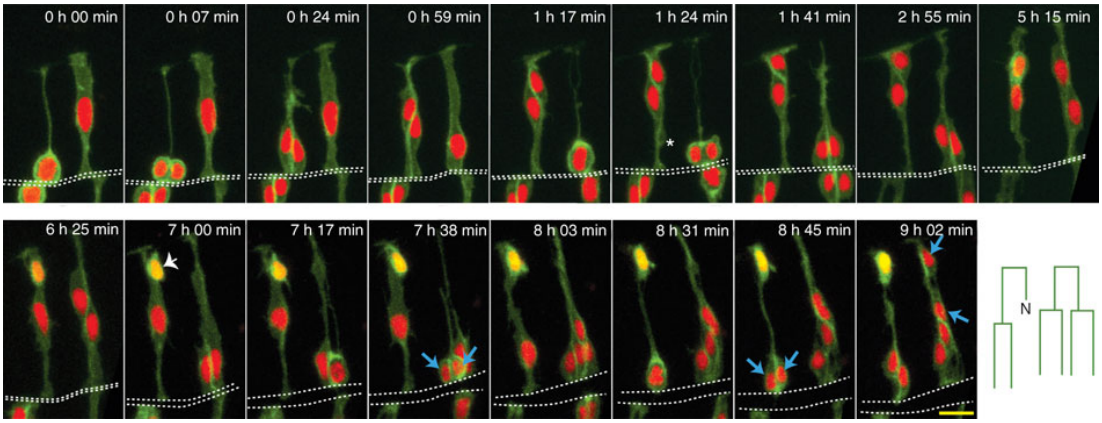

Figure 1.3. Neural stem cells undergo interkinetic nuclear migration prior to division. Selected frames from a time-lapse movie on a dorsal view of the zebrafish hindbrain focused on two neural stem cells (0h 00min) labeled with membrane-GFP (cell morphology) and H2B-RFP (nucleus) undergoing two different types of division. The apical surface (lumen) of the neural tube is outlined with a white dotted line. The progenitor cell on the left, whose nucleus is already at the lumen, undergoes asymmetric division to produce a neuron expressing *huC:GFP* (white arrow, 7h 00min) and a progenitor, which can divide again (8h 31 min – 9h 02min). The progenitor cell on the right at the beginning of the time-lapse translocates its nucleus to the lumen and undergoes symmetric division to produce two progenitors who both divide again (one symmetrically, blue arrows; one asymmetrically) by the end of the time lapse (9h 02min). Lineage trees for the two original progenitors are schematized on the right (N = neuron). Figure from Alexandre et al., 2010.

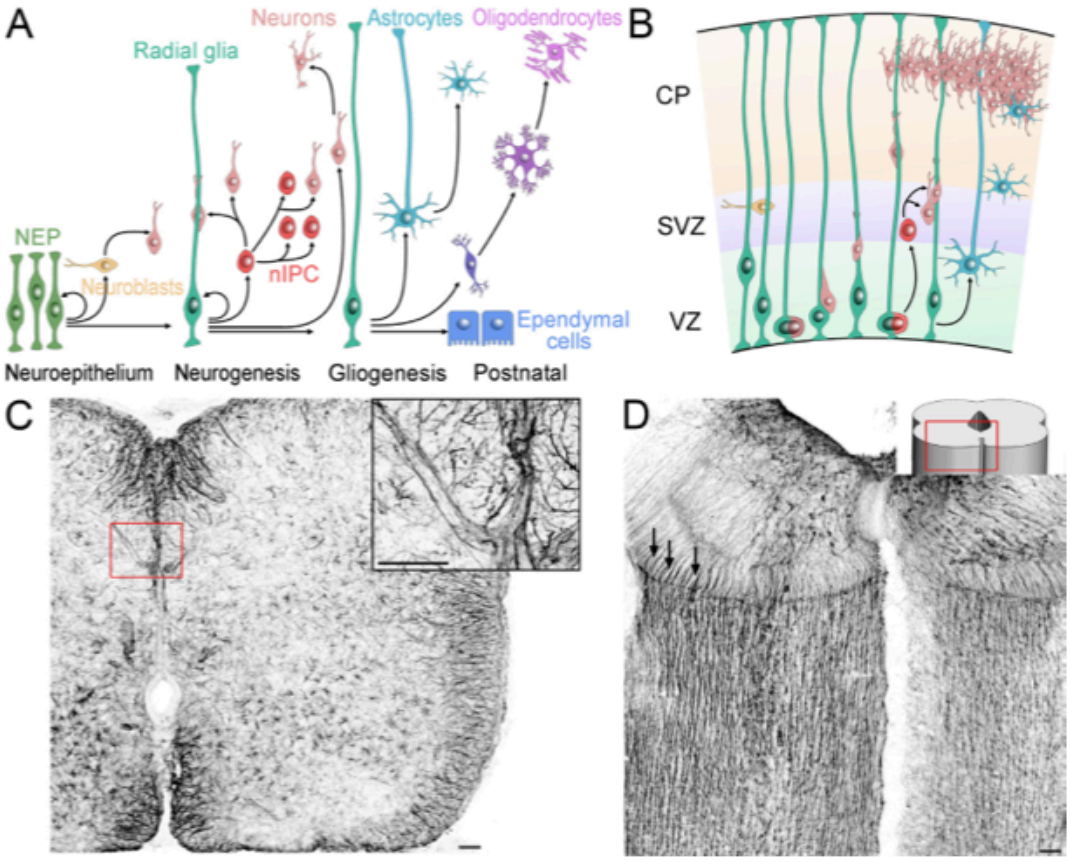

Figure 1.4. Proposed roles of radial glial cells during neural development. A) Multipotent neuroepithelial cells transform into radial glia, which contribute to the generation of neurons during neurogenesis prior to switching to a primarily gliogenic role to produce astrocytes, oligodendrocyte lineage cells, and ependymal cells. B) Radial glia undergo interkinetic nuclear migration in the VZ to generate a neuronal daughter cell, which then migrate along the parental pial fiber towards the cortical plate (CP) prior to differentiation into mature neurons. C) Cross section of mouse embryonic spinal cord stained with BLBP to label radial glial processes that form structural boundaries in the dorsal columns (enlarged in inset) to organize spinal axons within these tracts and prevent them from crossing into the other half of the spinal cord. D) Three-dimensional cross section view of the embryonic mouse spinal cord labeled with BLBP to illustrate columns formed by radial glial fibers to guide growing corticospinal axon tracts. Scale bars = 50mm. Figure from Barry et al., 2014.

CHAPTER 2

KIF11 DEPENDENT CELL CYCLE PROGRESSION IN RADIAL GLIAL CELLS IS REQUIRED FOR PROPER NEUROGENESIS IN THE ZEBRAFISH NEURAL TUBE

Sections contained within this chapter are adapted from the original research article: Johnson K, Moriarty C, Tania N, Ortman A, DiPietrantonio K, Edens B, Eisenman J, Ok D, Krikorian S, Barragan J, Gole C, Barresi MJ. Kif11 dependent cell cycle progression in radial glial cells is required for proper neurogenesis in the zebrafish neural tube. *Dev Biol.* 2014. Mar 1;387(1):73-92.

2.1 Introduction

Neurogenesis relies on precise cell cycle control of stem cell and progenitor cell proliferation mediated through an array of extrinsic and intrinsic molecular mechanisms (Demir et al., 2009; Sommer and Rao, 2002; Takahashi et al., 1995). Neuroepithelial cells serve as the first neural stem cell population in the vertebrate CNS, initially undergoing symmetrical self renewal cell divisions to amplify the progenitor pool (Hollyday, 2001; Kriegstein and Alvarez-Buylla, 2009; Tawk et al., 2007), proceeding to primarily asymmetric divisions to contribute to the first stages of neurogenesis (Kriegstein & Alvarez-Buylla, 2009). Neuroepithelial cells eventually transform into radial glial cells through upregulation of glial markers such as glial fibrillary acidic protein (Gfap), BLBP or GLAST, and by exchanging columnar morphology to a slender pial fiber (reviewed in Gotz & Huttner, 2005). Importantly, both neuroepithelial and radial glial cells divide similarly through a mechanism known as interkinetic nuclear migration, in which the nucleus translocates to the luminal surface during mitosis and migrates away following successful division (Alexandre et al., 2010; Gotz and Huttner, 2005; Leung et al., 2011).

Quite recently, radial glial cells have been accepted to function as self-renewing stem cells with neurogenic and gliogenic potential, acting as a main NSC population for the duration of embryonic neurogenesis (Malatesta et al., 2000; Noctor et al., 2002; and reviewed in Ihrie and Alvarez-Buylla, 2008; Pinto and Gotz, 2007). Radial glial cells are a transient population present in mammalian development and eventually transition into astrocytes; however radial glia continue to serve as the main neural stem cell population throughout life in zebrafish (Grandel and Brand, 2013; Kriegstein and Alvarez-Buylla, 2009; Suter et al., 2009). In zebrafish, it has been suggested that radial glia give rise to motorneurons and oligodendrocytes through the creation of a common progenitor cell population called oligodendrocyte progenitor cells (OPCs) (Kim et al., 2008). Under the influence of external signaling systems such as the Notch and Hedgehog pathways, OPCs contribute to the creation of oligodendrocytes and both primary and secondary motorneurons (Huang et al., 2012; Kim et al., 2008; Park et al., 2002, 2004; Shin et al., 2007). However, much still remains to be discovered about the mechanisms controlling radial glial proliferation and the neuronal and glial cell lineages radial glia create.

The zebrafish has emerged as a powerful genetic model system for the study of cell cycle control during vertebrate neurogenesis. Mutant loss of function analyses have uncovered essential cell cycle genes that range from regulating cell division throughout the embryo (*futile cycle*, Dekens et al., 2003; *crash&burn*, Shepard et al., 2005; *cassiopeia*, Pfaff et al., 2007), to more neural restricted control (*curly fry*, Song et al., 2004; *cug2*, Kim et al., 2011). Recently, we took part in a screen of zebrafish mutants that were originally isolated during a forward genetic insertional mutagenesis screen (Amsterdam et al., 2004), and identified a class of genes necessary for the proper number

and patterning of radial glial cells in the spinal cord (Barresi et al., 2010). An allele of the kinesin family member 11 gene (*kif11*^{hi3112a}) displayed a dramatic increase in the number of radial glial somas throughout the spinal cord (Barresi et al., 2010). Whether this increase was due to changes in radial glial proliferation rates, defects in the mechanisms of cell division, or impairments in proper interkinetic nuclear migration remained to be investigated.

Kif11, also known as Eg5 (Bim-C class of kinesins), is a plus-end directed heterotetrameric motor protein capable of simultaneously moving along two microtubules (Kapitein et al., 2005; Krzysiak et al., 2008; Sawin and Mitchison, 1995; Valentine et al., 2006a, 2006b). Eg5 has been shown to be directly associate with the anti-parallel, interpole microtubules of the mitotic spindle and generate the necessary bipolar forces to push centrosomes away from one another (Uzbekov et al., 1999; Valentine et al., 2006a). In support of this proposed function for Kif11/Eg5, pharmacological inhibition of Eg5 in *Xenopus* egg cultures causes mitotic arrest by preventing chromo- some segregation through the reduction of the bipolar spindle into a monopolar or monoaster spindle (Cochran et al., 2005; Gartner et al., 2005; Gruber et al., 2005; Kapoor et al., 2000; Mayer et al., 1999; Miyamoto et al., 2004; Muller et al., 2007; Sarli and Giannis, 2006). *eg5* is expressed in the mouse blastula and *eg5* knockout mice die prior to gastrulation, which demonstrates that Eg5 is required for early cleavage events in the mouse (Castillo and Justice, 2007; Chauviere et al., 2008; Ferhat et al., 1998). Unfortunately, the early lethality of *eg5* knockout mice makes it impossible to investigate the in vivo role of *kif11/eg5* during the later developmental events of embryogenesis and beyond.

In this study, we characterized the in vivo role of the kinesin motor protein Kif11,

and defined a specific role for Kif11 in early neural stem cell division and neurogenesis in the zebrafish spinal cord. Loss of Kif11 caused the progressive accumulation of mitotically arrested radial glial somas at the ventricular zone of the spinal cord. We experimentally supported the predictions made by mathematical modeling that severely delayed mitotic exit, reduced cell cycle entry, and increased programmed cell death are all critical factors that influence Kif11-dependent radial glial proliferation. Using loss of Kif11 as a method for indirect lineage analysis, we showed specific reductions in secondary neuronal cell types and maturing oligodendroglial cells. We propose that *kif11* plays a critical role in facilitating the separation of the mitotic spindle in radial glia, which has both direct and indirect implications for proper neurogenesis in the developing zebrafish neural tube.

2.2 Experimental Strategy

In this study, we combined using the *kif11*^{hi3112a} insertional mutant line with the use of pharmacological inhibitors of Kif11 (Supplemental Figure 2.1) to understand how loss of Kif11 regulates radial glial cell number in the zebrafish spinal cord. Using these approaches, we investigated how Kif11 was required during radial glial division throughout embryonic neurogenesis. To guide our experimental directions, we built a mathematical model of neural stem cell division to theoretically test our observations on radial glial division over time and predict neural stem cell dynamics during neurogenesis. Using our two loss of function approaches, we additionally identified differentiated neuronal and glial populations dependent on Kif11-mediated divisions to generate a working model for radial glial derived lineages in the embryonic zebrafish spinal cord.

2.3 Results

2.3.1 *kif11* is expressed by radial glial cells and is required for the correct number of luminal radial glial somas

As part of a large screen of insertional mutants, we identified *kif11*^{hi3112a} to be in a class of genes required for proper radial glial development in the zebrafish spinal cord (Barresi et al., 2010). Expanding on our previous characterization, homozygous *kif11*^{hi3112a} mutants exhibited an eight-fold increase in the number of Gfap+ radial glial somas that were all concentrated at the luminal surface of the ventricular zone (Figure 2.1A-E; wt avg. = 10.8±0.54, n=40; *kif11*$^{-/-}$ avg. = 81.1±4.34, n=24, $p<0.0001$). Quantification of the total number of nuclei in neural tube cross sections at three different axial positions showed no statistically significant difference between *kif11*^{hi3112a} mutants and wild type siblings (Figure 2.1E; wt avg. = 58.4±4.89, n=11; *kif11*$^{-/-}$ avg. = 58.2±6.85, n=19, $p>0.88$), suggesting that the increase in Gfap+ somas in *kif11*^{hi3112a} mutants is not the result of an increase in the number of cells in the neural tube.

The two recessive alleles of the *kif11* mutant, *kif11*^{hi486} and *kif11*^{hi3112a}, contain viral insertions within the second intron, and the *kif11*^{hi486} loci has been shown result in a 90% reduction in *kif11* gene expression (Amsterdam et al., 2002). Similarly, reverse transcriptase (RT) PCR analysis of 48hpf *kif11*^{hi3112a} homozygous mutants displayed a severe reduction in *kif11* transcripts as compared with their wild type siblings (Figure 2.1F). This suggests that while the *kif11* alleles do not cause null mutations, they do represent a significant knockdown of *kif11* transcript that results in embryonic lethality by 5dpf (Amsterdam et al., 2004; our own observations). All analyses of the *kif11* mutation throughout this study were performed on the *kif11*^{hi3112a} allele.

We hypothesized that if any residual Kif11 activity remained in the *kif11* mutant, additional methods to knock down its function may result in more severe phenotypes. We tested the efficacy of three known pharmacological inhibitors of Eg5 on zebrafish: Monastrol, Dimethylenastron (DME), and S-trityl-L-cysteine (STLC) (DeBonis et al., 2004; Gartner et al., 2005; Kapoor et al., 2000; Kozielski et al., 2008; Mayer et al., 1999; Muller et al., 2007). Comprehensive dose response analysis in wild type (AB) embryos revealed that a concentration of 0.875mM STLC yielded maximal effects that phenocopied the mutant and did not cause any additional gross morphological malformations to the neural tube (Supplemental Figure 2.1A-K). Using STLC as a working pharmacological inhibitor in zebrafish, we next tested if the remaining *kif11* transcript in *kif11* mutants (Figure 2.1F) contributes to radial glial development. Homozygous *kif11*$^{+/+}$ wild type, heterozygous *kif11*$^{+/-}$ siblings, and homozygous *kif11*$^{-/-}$ mutants treated with 0.875mM STLC from 5hpf to 30hpf showed the same increase in the number of Gfap+ somas as *kif11*$^{-/-}$ mutants treated with the DMSO vehicle control, and importantly, no statistically significant difference was seen between any of the treated groups (Supplemental Figure 2.1L). This result confirmed that homozygous *kif11* mutants represent a phenotypically null mutation and that heterozygous genotypes possess no phenotypic consequence. Lastly, while we did determine through RT-PCR that *kif11* is maternally expressed from the one-cell-stage and retained throughout embryogenesis (data not shown), lack of phenotypic change following STLC treatment in *kif11* mutants also demonstrates that there is little to no compensation from these maternal contributions on the radial glial population.

We further investigated the role Kif11 plays in radial glial development by examining the pattern of *kif11* transcript expression throughout the embryonic CNS. Whole-mount *in situ* hybridization on wild type (AB) tissue revealed concentrated *kif11* expression throughout the ventricular zone of the brain and spinal cord extending from the roofplate to the floorplate at 27hpf (Figure 2.1G-J, arrows). *kif11* expression was also detected outside the nervous system in the eye and ventral portions of the trunk (Figure 2.1H-J). Fluorescent *in situ* hybridization of *kif11* expression showed higher levels of expression in the dorsal two-thirds of the neural tube, but was consistently detected throughout the ventricular zone and floorplate (Figure 2.1J, inset; K, inset). *kif11* transcript was detected in radial glial cells as determined by overlapping expression with Green Fluorescent Protein (GFP) positive cells in *tg(gfap:eGFP)* transgenic embryos (Figure 2.K-M).

2.3.2 Loss of *kif11* causes an accumulation of M-phase arrested radial glia over time

In *kif11* mutants, the increase in the number of Gfap+ somas at the luminal surface was seen without a change in overall number of nuclei at 30hpf, which suggested that the proportion of radial glia attempting division might be altered in *kif11* mutants. We labeled *kif11* siblings for the M-phase marker anti-Phosphohistone H3 (PH3) and anti-Gfap to determine if Gfap+ radial glial somas were actively undergoing mitosis at any time throughout embryonic neurogenesis (Pfaff et al., 2007; Shepard et al., 2005). Between the ages of 15 and 72hpf, a majority of Gfap+ somas in wild type siblings and nearly all in *kif11* mutants were positive for PH3 (wt mean, 83.5%; *kif11*$^{-/-}$ mean, 98.9%; Figure 2.2A,E insets). These results suggest that with our labeling method, most Gfap+

somas assayed were undergoing mitosis in both wild type and *kif11* mutants. It is important to note that while the anti-Gfap antibodies we are using label all astroglial processes, we only observed subcellular expression within the cell body during the process of division (Figures 2.2, 2.3). Such a change in Gfap protein localization within a dividing cell has been described for cells in culture, in which the phosphorylation state of Gfap can influence its differential positioning at the cleavage furrow ((Inagaki et al., 1994; Yasui et al., 1998); reviewed in (Middeldorp and Hol, 2011)).

Quantitative analysis of the mitotic index in *kif11* wild type and mutant siblings showed different patterns of M-phase cells over time. The number of M-phase radial glia recorded in wild type siblings remained constant at approximately 10 cells between 15hpf and 36hpf, after which mitotically active cells declined gradually to near zero by 72hpf (Figure 2.2A-D, I, hatched black line, J, white and grey bars). In contrast, *kif11* mutants showed significantly more Gfap+ cells in M-phase at 15hpf (wt avg. = 11.16±0.72, n=13; *kif11*$^{-/-}$ avg. = 27.83±3.23, n=23, $p<0.0001$) that increased steadily at an average rate of 16 cells per hour (Figure 2.2E-H, I, red line, J, black and hatched bars) until 48hpf, which was followed by a dramatic drop in the number of PH3+ radial glia and total PH3+ cells (Figure 2.2I,J). Additionally, there were a significant percentage of PH3+ nuclei that did not co-express Gfap, which were consistently present in both wild type and *kif11* mutants at all ages examined (wt avg. = 55.5%; *kif11*$^{-/-}$ avg. = 29.2%).

Since Kif11/Eg5 has a known role in mitotic spindle function, we next sought to determine if the accumulation of M-phase radial glia in *kif11* mutants was due to a mechanistic failure of mitotic spindle separation. We labeled *kif11* siblings for anti-alpha-Tubulin and anti-Gfap to visualize spindle morphology in radial glial cells (Figure 2.3).

Wild type spindle morphologies were unperturbed, showing microtubule arrangements consistent with metaphase, anaphase or telophase (Figure 2.3A-D; not all spindle morphologies shown). In contrast, *kif11* mutants showed Gfap+ cell somas exhibiting a single monoastral spindle phenotype (Figure 2.3E-H). Previous cell culture studies using Eg5 specific pharmacological inhibitors have shown similar monoaster spindle formation that results in mitotic arrest (DeBonis et al., 2004; Kapoor et al., 2000; Muller et al., 2007; Valensin et al., 2009). To confirm that our previous pharmacological inhibition assay also results in monoaster spindle formation in radial glia, vehicle control and STLC treated wild type (AB) embryos were also assayed for anti-alpha-Tubulin and anti-Gfap. Similar to *kif11* mutants, STLC treated wild type embryos displayed a single monoastral spindle phenotype within Gfap+ cells as compared to the unaffected spindles of DMSO control treated embryos (Figure 2.3I-P). These data indicate that the loss of Kif11 causes defective mitotic spindle formation, which potentially leads to mitotic arrest and the accumulation of radial glial somas at the ventricular zone.

2.3.3 Mathematical modeling reveals *kif11*-dependent changes in cell cycle rate and cell survival

We next employed mathematical modeling to theoretically test whether accumulation of mitotically arrested cells alone can fully account for the number of radial glial somas we have quantified, or predict whether additional parameters of cell division are also impacted by the loss of *kif11.* We generated a differential equations model for radial glial cell division that considered several influencing parameters: the radial glial generating potential of neuroepithelial cells over time $R_{in}(t)$, non-dividing radial glial

cells *G(t),* and radial glial cells in S-phase *S(t)* or in mitosis *M(t)* (Figure 2.4A). Performing data fitting on this model yielded a close fit to the wild type raw data with robust parameter estimation as indicated by the 95% confidence interval (Figure 2.4B; Table 1). According to our model, the resulting best-fit parameter values indicated that neuroepithelial proliferation ends after ~48hpf. In addition, radial glial cell division is dominated by differentiation, such that only 9% (~0.18/2) of daughter cells remain as radial glial cells while the rest become progenitors.

We next applied this mathematical model towards testing whether simple mitotic arrest alone could account for the apparent accumulation of M-phase radial glia in *kif11* mutants (Figure 2.2). When manipulating k_{out} to simulate a full mitotic arrest or a 5x or 10x delay in the rate of mitotic exit (decrease in k_{out}), accumulation alone does not fit the quantification seen in *kif11* mutants (Figure 2.4C). Rather our model predicted that a greater number of radial glial cells should be present at each time point for accumulation alone to be valid (Figure 2.4C), suggesting that additional parameters are impacting the dynamics (number and/or rate) of radial glia in mitosis.

It is known that cells arrested in mitosis for a prolonged period of time can trigger apoptosis (Kozielski et al., 2008; Marcus et al., 2005); therefore, we next evaluated a constant rate of cell death for cells that are in the mitotic phase of the cell cycle ($k_{death}M$). The population of apoptotic cells, *D(t)*, is assumed to be cleared within a time-scale of 3 hours (k_{clear}) in the embryonic spinal cord (Bashiruddin and Barresi, unpublished observations). Taking these two processes into account, we then varied the values of k_{out} to achieve a 5x, 10x, or 20x delay in mitosis exit and k_{death} to reflect cells dying at a rate of either 10% or 50% per hour (Figure 2.4D). Simulating an increase in cell death caused

the number of cells to decrease, however this resulted in a poor fit to the *kif11* mutant data at later time points. Further investigation by varying these two parameters (k_{out} and k_{death}) never produced an accurate fit to the *kif11* mutant data (Figure 2.4D). Increasing the delay of mitotic exit by 10x (decreasing k_{out}) did increase the number of cells that produced a better fit to the *kif11* mutant data at earlier time points as opposed to only a 5x delay, but this simulation still poorly fit the later time points. An even longer delay in mitotic exit (20x) paired with either a 10% or 20% cell death of radial glia improved the fit to the *kif11* mutant M-phase radial glial data at the later time points yet worsened the fit for the earlier data points. These results allow us to conclude that delays in mitosis exit and subsequent cell death cannot fully explain the experimental data.

We next considered whether reducing the proliferation rate of radial glia in addition to mitotic exit delay and cell death would best fit the M-phase radial population captured in *kif11* mutants. To theoretically test this we simulated a lengthening of the G1-phase of the cell cycle (reducing the value of k_s) and performed data fitting to find the best-fit value for the parameters k_{out}, k_{death}, and k_m (Table 2.2). This model, called Model Variant 1, predicted that the radial glial population has an approximate 9x lengthening of the G1-phase of the cell cycle to obtain a well aligned fit of *M(t)* to the *kif11* mutant data. This slower rate of cell cycle entry was obtained as a best fit together with an average ~15x longer stay in M-phase and ~2% of those cells in mitosis undergoing cell death per hour (Figure 2.4E).

Our mathematical Model Variant 1 suggested that the accumulated M-phase radial glia in the *kif11* mutant was the combined result of cell death, delayed cell cycle entry, and significant mitotic exit delay. To biologically verify these predictions, we first

quantified the number of cells undergoing apoptosis in the neural tube through anti-activated Caspase-3 labeling. Increased cell death was detected at 15hpf in the neural tube of *kif11* mutants as compared with wild type siblings (wt avg. = 2.15±0.9, n=20; *kif11*$^{-/-}$ avg. = 15.4±5.9, n=16, $p<0.05$) and the number of apoptotic cells significantly increased by 20hpf to a level that remained relatively constant throughout the time course (1.33±0.54, n=48; *kif11*$^{-/-}$ avg. = 54.69±6.75, n=29, $p<0.001$; Figure 2.5A,B,E). To determine if loss of *kif11* causes a delay in cell cycle entry, we next assayed the number of cells entering S-phase through BrdU pulse-fix labeling. *Kif11* siblings were briefly exposed to BrdU at different developmental stages and fixed immediately after treatment to capture all cells in the neural tube undergoing DNA replication at that stage. Quantification of BrdU incorporation at 15hpf, 20hpf, 25hpf, 30hpf and 36hpf revealed that cells in the neural tube of *kif11* mutants did not show any change at 15hpf (wt avg. = 186.3 cells±7.6, n=15; *kif11*$^{-/-}$, avg. 181.5 cells±6.0. n=15; $p=0.62$), but did show an approximately 24% reduction at each later time point as compared with wild type siblings (Pooled averages for 20hpf to 36hpf: wt avg. = 214.6 cells, n=57; *kif11*$^{-/-}$ avg. = 163.8 cells, n=58; $p<0.0001$; Figure 2.5C-E). As predicted by our mathematical model, these results confirm that cell cycle entry and apoptosis are parameters also affected by the loss of *kif11*.

2.3.4 Mitotic arrest and progressive cell death determine cell number in *kif11* neural tubes

If our mathematical model is accurately capturing all the parameters of neural stem cell division, then the quantitative measures of BrdU incorporation and apoptosis

should be comparable to the representative trends of *S(t)* and *D(t)* respectively in this model. Comparing to the wild type BrdU data, *S(t)* matches the temporal dynamics of the data, but is approximately 20% lower in magnitude (Supplemental Figure 2.2A). A lower value is to be expected, since the collected data represents the total number of cells in S-phase at a given time post-fertilization, whereas our model is only considering radial glial cells in division. Performing the same comparison for the *kif11* mutant yielded outputs from Model Variant 1 that failed to capture many aspects of the new experimental measurements of BrdU incorporation and cell death. First, the dynamics of *S(t)* were too slow as compared with the BrdU data collected in *kif11* mutants, such that, a peak was obtained approximately 20 hours later than that observed in the raw BrdU data set (Supplemental Figure 2.2B). Second, the level of cell death *D(t)* obtained was also far too low in comparison to the counted number of apoptotic cells in the *kif11* mutant over time (Supplemental Figure 2.2C). Although we successfully performed data fitting for *M(t)* using Model Variant 1, we dispensed this model and sought to incorporate other critical factors to be incorporated into the mathematical model.

By examining the difference in the number of BrdU positive cells and apoptotic cells between wild type and *kif11* mutants, we observed that the proportion of cells in the mutant positive for activated Caspase-3 is similar to the proportion of cells that should be experiencing S-phase according to the wild type data (Figure 2.5E; means = 45.7 act. Caspase-3+ cells in $kif11^{-/-}$/wt and 41.6 BrdU+ cells in wt/$kif11^{-/-}$). Moreover, the trend of these difference curves suggested an inverse relationship between cell death and proliferation; such that, a peak in cell death is followed by a subsequent drop in BrdU incorporation and later observed drops in cell death were similarly followed by relative

increases in BrdU incorporation (Figure 2.5F). This data analysis suggests that the presumed mitotic arrest-induced cell death may progressively establish an unhealthy environment in the neural tube, which results in more extensive cell death at all stages of the cell cycle that could in turn influence the rate or number of cells actively proliferating.

Previously, we found using Model Variant 1 that the level of cell death is far too low in comparison to the observed experimental data (only 2% of mitotic radial glia undergo apoptosis per hour in Model Variant 1). To theoretically test whether cell death occurring at all stages of the cell cycle could better represent the dynamics of radial glial cell division in *kif11* mutants we generated Model Variant 2 for best fit analysis (Figure 2.6A). In Model Variant 2, we divided cell death parameters into k_{death1} and k_{death2}, which represent the cell death due to a potentially toxic environment and due to mitotic arrest respectively (Figure 2.6A). k_{death1} occurs during the G1 and S-phases of the cell cycle while k_{death2} is during M-phase. To focus on the impact of cell death as a driving force, no delays in cell cycle entry were factored into this Model Variant 2. As before, we performed data fitting on *M(t)* to find the best-fit value for the following parameters: k_{out}, k_{death}, and k_{death2}, as listed in Table 2.3. Data fitting for *M(t)* using Model Variant 2 obtained a close fit to the *kif11* mutant mitotic radial glial data (Figure 2.6B). Importantly this model yielded outputs that were more closely aligned to the BrdU and activated Caspase-3 data for both wild type and *kif11* mutants (Figure 2.6C-E) as compared with the simulations obtained using Model Variant 1. Specifically, Model Variant 2 showed improved *S(t)* temporal correspondence with the BrdU data, however it was still significantly lower in magnitude (Figure 2.6E). Similarly, *D(t)* obtained from Model

Variant 2 was now well aligned with the cell death data in both magnitude and temporal correspondence from 15 to 36hpf; however, the resulting *D(t)* curve failed to capture an observed secondary peak in cell death at 48hpf (Figure 2.6C). While Model Variant 2 does not completely capture all aspects seen in all the raw data collected, simulations obtained using best-fit parameter values suggest that a near mitotic arrest of radial glial cells paired with two rates of cell death during the different phases of the cell cycle are sufficient to explain most of the dynamics witnessed in the *kif11* mutant.

2.3.5 Cell density is maintained in *kif11* mutants

Due to the cell death and changes in cell cycle dynamics seen in *kif11* mutants, we revisited our earlier observation that the total number of cells in the neural tube remains unchanged between *kif11* siblings at 30hpf (Figure 2.1E). We extended this data by quantifying the total cell density of the neural tube over time in wild type and *kif11* mutants. Similar to our previous results, the average number of total nuclei was not statistically different between wild type and *kif11* mutants with the exception of slight decreases at 25hpf and 48hpf in *kif11* mutants (Supplemental Figure 2.3A,B). At no time was the area of the neural tube significantly different (Supplemental Figure 2.3A,C). Importantly, the calculated cell densities (cells/μm^2) within wild type and *kif11* mutant neural tubes showed remarkably little variation from 15hpf to 72hpf (Supplemental Figure 2.3D). Although, due to the significant differences seen in the total number of nuclei at 25hpf and 48hpf, their corresponding cell densities recorded as statistically different. However, from a biological perspective, the unchanged nature of nuclei number, area, and resulting density in *kif11* mutants paired with the similar proportions

and behavioral trends of BrdU incorporation and cell death over time (Figure 2.5F) implies there is a tight level of compensatory regulation between these processes to maintain overall proportions in the neural tube.

2.3.6 Kif11 has two temporal phases of mitotic influence

A steady increase in the number of M-phase radial glia in *kif11* mutants suggests Kif11 may exhibit a temporally consistent influence over neurogenesis. To test if there were temporal changes in the requirement of Kif11 for the radial glial population, we treated wild type (AB) embryos with 0.875mM STLC or DMSO starting at different ages (5, 10, 15, 20, and 25hpf; Figure 2.7A). Embryos remained in their treatment until 30hpf and were immunolabeled for anti-Gfap and anti-PH3 to assay for mitotic radial glia. No change in the number of M-phase radial glia was seen across vehicle control treated embryos (Figure 2.7B-D, H, white and grey bars). In contrast, all ages treated with STLC prior to 25hpf displayed dramatic increases in the number of M-phase radial glia with respect to their controls (Figure 2.7E-G, H, hatched and black bars; $p<0.0001$). Comparison of experimental groups indicated they were also statistically significant to each other with the exception of 10 and 15hpf, where no significant change in the number of PH3+ cells alone ($p=0.88$) or double labeled with Gfap in the soma ($p=0.5$) was seen (Figure 2.7H, bracket). The difference in mitotic index between 5 and 10hpf indicated that an average of 46.7 PH3+ cells had accumulated (cells per laterally imaged neural tube between somites 9 and 13), 65.2% of which were co-expressing Gfap (Figure 2.7H). A similar increase in the mitotic index of on average 43.7 PH3+ cells was additionally recorded between 15 and 20hpf, 85.8% of which were co-labeled for Gfap. The number

of mitotic cells continued to increase between 20 and 25hpf, yet at a reduced amount compared with earlier time periods (13.81 PH3+; 9.31 Gfap+). Given the assumption in these calculations that no PH3+ cells are progressing though mitosis, these data suggest that Kif11 is not required between 10 and 15hpf but does play a significant role in cell division of neural stem cells during an early phase (5-10hpf) and a later phase (15-25hpf).

2.3.7 Loss of Kif11 causes reductions in secondary interneurons and motorneurons

Arresting key progenitor populations in mitosis could have severe consequences for the proper generation of neuronal and glial cell fates during neurogenesis. We hypothesized that Kif11 deficient embryos could be used as a novel tool to determine which neuronal and glial cell types may rely specifically on Kif11-dependent radial glia as their stem cell population. To determine whether any neuronal populations in the spinal cord were affected following loss of Kif11, we labeled for interneurons, sensory and motor neurons using anti-GABA and anti-Islet-1 (Isl) antibodies (Appel and Eisen, 1998; Bernhardt et al., 1992; Myers et al., 1986; Park et al., 2004). GABA labeling within vehicle control and wild type *kif11* siblings identified four classes of interneurons (dorsal longitudinal ascending (DoLA), commissural secondary ascending (CoSA), ventral longitudinal descending (VeLD), and Kolmer–Agduhr (KA)) with distinct dorsoventral domains throughout the neural tube (Figure 2.8A,E (Appel and Eisen, 1998; Bernhardt et al., 1992)); however, certain interneuron populations showed unique phenotypes following loss of Kif11 function at 30hpf (Figure 2.8B,F). Specifically, both *kif11* mutants and STLC treated embryos displayed a disorganized CoSA interneuron domain, along with VeLD and KA interneurons that frequently exhibited aberrant, dorsally

growing axonal pathfinding errors (Figure 2.8B,F, arrowheads). Quantitative analysis of the total number of GABA+ interneurons showed a 22% decrease in *kif11* mutants (wt avg. = 53.02±0.95, n=43; *kif11*$^{-/-}$ avg. = 41.3±1.04, n=37; $p<0.0001$) and a 28% decrease in STLC treated embryos (DMSO avg. = 55.81±0.86; n=43; STLC avg. = 40.02±1.21, n=41; $p<0.0001$; Figure 2.8I). Quantification of specific GABA+ interneuronal cell types revealed a clear and specific reduction of CoSA interneurons in *kif11* mutants (*kif11*$^{-/-}$ avg. = 13.41±0.68; $p<0.0001$) and STLC treated embryos (STLC avg. = 12.27±0.88; $p<0.0001$) as compared with their respective controls (wt avg. = 23.19±0.58; DMSO avg. = 25.84±0.57) (Figure 2.8I). These results suggest that the significant loss of CoSA interneurons nearly accounts for the total number of GABAergic interneurons lost in *kif11* mutants or STLC treated embryos. Importantly, analysis of GABA+ immunolabeling over time from 24hpf to 36hpf in *kif11* mutants and STLC treated embryos revealed a consistent deficit in the CoSA population of interneurons relative to wild type and control embryos (Figure 2.8J), while DoLA, VeLD, and KA showed no significant reduction in number over this same time span (Supplemental Figure 2.4). The lack of a phenotype or change in number over time in these other interneuronal populations provides confidence that the CoSA cell reductions (and other phenotypes described here) are specific and not due to any general developmental delay.

Islet-1 labeling at 30hpf in wild type sibling or DMSO control treated embryos clearly distinguishes dorsally positioned Rohon Beard sensory neurons (wt avg. = 24.9±0.69, n=32; DMSO avg. = 22.49±0.56, n=35) from the more ventrally positioned motor neuron (MN) populations (wt avg. = 67.47±6.45; DMSO avg. = 78.91±2.56) (Figure 2.8C,G; Song et al., 2004). These neuronal populations were both present in

30hpf *kif11* mutants and STLC treated embryos (Figure 2.8D, H); however, while the number of Rohon Beard sensory neurons was largely unaffected (*kif11*$^{-/-}$ avg. = 26.1±1.16, n=25, p>0.29; STLC avg. = 20.5±0.96, n=26, p>0.06), Isl+ motorneurons were significantly decreased by 23% in *kif11* mutants (*kif11*$^{-/-}$ avg. = 52.16±4.13, p<0.01) and 45% in STLC treated embryos (STLC avg. = 43.65±2.32, p<0.0001) (Figure 2.8I). Because the Islet-1 antibody cannot differentiate between primary and secondary motorneurons (Appel et al., 1995; Hutchinson and Eisen, 2006), therefore we treated *tg(mnx1:GFP)* and *tg(gata2:EGFP)* embryos with STLC starting at 5hpf (Figure 2.9). Examination of *tg(mnx1:GFP)* transgenic embryos at early somitogenesis stages can show the formation of primary motorneurons over time (Flanagan-Steet et al., 2005, Seredick et al., 2012). Treatment of *tg(mnx1:GFP)* transgenic embryos with STLC from 5hpf to 18, 24 or 30hpf did not reveal any qualitative loss in primary motorneurons (Figure 2.9A-F). In contrast, *gata2* drives expression of GFP in secondary motorneurons and a small population of interneurons at 48hpf (Meng et al., 1997). A severe reduction in *gata2* driven expression of GFP positive cells (58% loss) was detected in the spinal cords of 5-48hpf STLC treated embryos relative to DMSO treated control embryos (DMSO avg. = 186.62±4.05, n=34; STLC avg. = 78.52±5.16, n=25; p<0.0001; Figure 2.9G-I). These results suggest that secondary motorneurons, as opposed to primary motorneurons, are most affected following loss of Kif11-dependent radial glial division.

2.3.8 Kif11 is necessary for the development of radial glial derived oligodendrocytes

To determine whether Kif11 mediated radial glial division is necessary for different stages of oligodendrocyte development, *tg(olig2:EGFP)* embryos were treated

with 0.875mM STLC at 5hpf and remained in treatment until fixation at 24hpf (initiation of *olig2* expression), 36hpf (specification of OPCs), or 72hpf (oligodendrocyte maturation and axon myelination) (Kirby et al., 2006; Shin et al., 2003) (Figure 2.10). At 24hpf there was no change to the pattern or number of GFP expressing cells in the ventral OPC layer between treatment groups ($p>0.33$; Figure 2.10A,E,I); however, the number of dorsally migrating OPCs in the 5-36hpf treatment group was reduced compared with controls (DMSO avg. = 18.93±1.24, n=33; STLC avg. = 7.17±0.88, n=23; $p<0.0001$; Figure 2.10B,F,I). This trend was consistent in the 5-72hpf treatment group (DMSO avg. = 14.93±1.32, n=23; STLC avg. = 8.54±1.15, n=19; $p<0.0001$; Figure 2.10C,G,I) with no statistically significant difference seen in the reduction of dorsal migrating OPCs between the 5-36hpf and 5-72hpf treatment groups (Figure 2.10I; $p>0.98$). Importantly, some GFP+ cells exhibited morphologies characteristic of cell death (Figure 2.10G, arrowhead), and the presence of these irregular GFP+ cells increased with each older treatment group. We confirmed that these irregular GFP+ cells co-express anti-activated Caspase-3 in *tg(olig2:EGFP)* embryos treated with STLC from 5 to 72hpf, indicating these cells are undergoing apoptosis (Figure 2.10G, inset). These irregularly shaped cells were not included in the above quantification of migrating OPCs. Lastly, *tg(olig2:EGFP)* embryos were also treated with STLC from 24-72hpf to discern whether changes in the Olig2+ populations were the result of a requirement for Kif11 function after *olig2* expression and OPC specification (Kirby et al., 2006; Park et al., 2007; Shin et al., 2003). No difference in the number of migrating OPCs was seen following a 24 to 72hpf STLC treatment (Figure 2.8D,H,I). These data suggest that the loss of early Kif11 function causes significant reductions in migrating OPCs and oligodendrocytes.

To determine how Kif11 may be influencing oligodendroglial development, we performed whole mount *in situ* hybridization for *kif11* in 30hpf *tg(olig2:EGFP)* embryos. We detected a subset of GFP+ cells expressing *kif11* transcript that were restricted to the luminal surface (Figure 2.10J, inset), which is consistent with the location of proliferating progenitor populations (Kirby et al., 2006; Park et al., 2007; Shin et al., 2003). Assays for anti-Gfap and anti-PH3 antibody expression in STLC treated *tg(olig2:EGFP)* embryos revealed that nearly all mitotic *olig2:*EGFP+ cells were also Gfap+ (Figure 2.10A,E inset; full qualitative data not shown; K, grey and black bars). Furthermore, while no difference in the OPC migratory pattern was seen at 24hpf, there was a significant increase in the number of mitotic OPCs in this STLC treatment group (DMSO avg. = 3.41±0.27, n=27; STLC avg. = 9.55±0.26, n=18; $p<0.0001$; Figure 2.10K). The number of M-phase OPCs increased greater than 2-fold in the 5-36hpf treatment group compared with the 5-24hpf treatment group (DMSO avg. = 5.58±0.45; STLC avg. = 23.65±0.4; $p<0.0001$; Figure 2.10K). While the longest treatment period of 5-72hpf still showed significant increases in the number of M-phase OPCs as compared with DMSO treated controls (DMSO avg. = 0.125±0.13; STLC avg. = 12.18±0.13; $p<0.0001$), this increase was not statistically significant from the 5-24hpf treatment group ($p>0.2$). Lastly, while no defects were detected in oligodendrocyte differentiation in the 24-72hpf STLC treatment group (Figure 2.7D,H,K), there was still a substantial increase in the number of M-phase OPCs (DMSO avg. = 0.09±0.05, n=40; STLC avg. = 5.22±0.01, n=37; $p<0.0001$; Figure 2.10K). This temporal manipulation of Kif11 lends support to a radial glial origin for OPCs, and suggests that OPCs require Kif11 for proper maturation into oligodendrocytes.

2.4 Discussion

In this study, we explored the role of the kinesin motor protein Kif11 in mediating radial glial cell division and the impact its loss may have on neurogenesis during the development of the zebrafish spinal cord. We present a model whereby Kif11 functions to mediate spindle pole separation in radial glial cells of the developing neural tube. Loss of Kif11 function causes mitotic arrest in radial glial cells leading to increases in cell death and subsequent reductions in cell proliferation (Figure 2.11A). In addition, there are indirect lineage consequences resulting from mitotically arrested radial glia that support a specific dependence on radial glial origin by later-born secondary motorneurons, CoSA interneurons, and oligodendrocytes (Figure 2.11B). Lastly, despite all the changes in cell cycle dynamics, cell numbers and cell survival, the appropriate cell density within the neural tube is maintained over the course of neurogenesis, which suggests the presence of a currently unidentified mechanism of compensatory regulation. This investigation demonstrates a clear cell biological role for Kif11 in the division of stem cell populations *in vivo* during neural development, and it has revealed the presence of a remarkably robust mechanism to maintain size and cell densities in the neural tube.

2.4.1 Mathematical modeling of neurogenesis

We employed mathematical modeling to help identify and better understand the cellular and developmental processes potentially impacted by the loss of *kif11*. We constructed a mathematical model that only tracks changes in the population of radial glia at different stages of the cell cycle. The models were built to test out the most probable,

biologically relevant effects of *kif11* mutations, namely changes in proliferation and mitotic arrest that may then lead to cell death. However, due to a lack of existing and completely applicable quantitative measures related to neurogenesis in zebrafish, our models are currently constructed in the most simplistic form. Limitations of the current model include a coarse representation of the temporal changes in the neuroepithelial population (represented as a linear decrease from 10hpf). Additionally, stem and progenitor cell renewal and differentiation may variably change over time, and these temporal changes to the division types and differentiation of radial glia and their progeny over time is not represented in our model. Despite these and likely other potential limitations, comparison between the output of the mathematical model in its current simplified form and the experimental data has already revealed that mitotic arrest, toxicity-induced cell death, and reduced cell cycle entry are possible additional effects of a loss of Kif11 function. Incorporating a more realistic neuroepithelial and radial glia maturation as well as testing out different feedback mechanisms for the regulation of cell proliferation and differentiation form a promising future direction.

2.4.2 Kif11 is required for radial glial cell progression through mitosis

Our analysis of Kif11 function in the developing zebrafish nervous system provides in vivo confirmation of past cell culture studies to dissect Eg5 function in cell division and it also reveals broader implications of the role this kinesin plays in neurogenesis. Plus-end directed tetrameric kinesins exert forces that slide interpole microtubules toward the centrosomes, which contribute to spindle pole and chromosome separation (Sawin and Mitchison, 1990, 1991; Sawin et al., 1992). Loss of Eg5 function

in cultured *Xenopus* oocytes and human cancer cells causes monoaster spindle formation leading to mitotic arrest in these cells (Kapoor et al., 2000; Miyamoto et al., 2004; Sawin and Mitchison, 1995). We show that in fact radial glial cells display similar monoaster spindles at the ventricular zone in *kif11* mutants (Figure 2.3). Therefore, we propose that as a radial glial cell enters the cell cycle its nucleus migrates to the ventricular zone where the mitotic spindle collapses inward forming monoaster microtubule morphology during M-phase. This disruption of radial glial mitotic spindles causes significant delays in exiting mitosis, which likely represents a full mitotic arrest in these cells leading to the progressive accumulation of radial glial somas at the ventricular zone over time.

The *kif11* zebrafish mutant offers a unique tool to assay radial glial development throughout embryonic neurogenesis. Eg5 knockout is lethal in mice prior to gastrulation (Castillo and Justice, 2007; Chauviere et al., 2008); in contrast, *kif11* zebrafish mutants progress through the early stages of gastrulation and demonstrate distinct later phases of Kif11 dependence. We did verify that maternal contributions of *kif11* are present in wild type, and, because *kif11*^{hi3112} is a recessive mutation, similar maternal contributions of Kif11 may partially support early embryonic development in *kif11* mutants. However, earlier inhibition of Kif11 by STLC treatment in *kif11* siblings did not alter radial glial number (Supplemental Figure 2.1L), indicating that any maternally expressed *kif11* does not play a significant functional role in early CNS development. Proteins redundant with Kif11 mitotic function, such as the Kif15/Hklp2 motor protein in HeLa cells (Tanenbaum et al., 2009) and the Ncd motor protein in Drosophila embryos, have been documented previously (Sharp et al., 1999; Wilson et al., 2004); however, whether compensation by another molecular motor for Kif11 exists in zebrafish remains to be elucidated. Based on

these and our data we propose that cell division in the early zebrafish embryo either operates in a *kif11*-independent manner or uses redundant motor proteins that functionally compensate for deficiencies in Kif11, whereas later cell divisions during neurogenesis are dependent on Kif11 function.

2.4.3 Loss of Kif11 has consequences to overall cell cycle regulation in the neural tube

Mathematical modeling predicted that delays in mitotic exit alone could not account for the number of accumulating mitotic radial glial somas in *kif11* mutants. Our initial mathematical Model Variant 1 predicted that increases in the rate of cell death and decreases in the rate of cell cycle entry both paired with near mitotic arrest appropriately captured the number of M-phase radial glia in *kif11* mutants (Figure 2.4). While we did experimentally confirm the presence of increased apoptosis and decreased S-phase cells in *kif11* mutants (Figure 2.5), Model Variant 1 failed to capture S-phase and cell death data (Supplemental Figure 2.2). Mathematical Model Variant 2 was able to reproduce not only the mitotic radial glial data but also partially fit the collected BrdU and activated Caspase-3 data (Figure 2.6). Model Variant 2 predicted that a mitotic arrest characterized by a 226 (94 h) delay in completing mitosis with two forms of cell death (1% cell death due to mitotic arrest and 44% death due to worsening environmental conditions) together were the primary influencing factors for the number of M-phase radial glia during neurogenesis in *kif11* mutants (Figure 2.6B). A logical next step analysis would be to mathematically model the multiple cell death modes but paired with a slowing of cell cycle entry. We completed this analysis, and while it improved slightly the data fitting to

S(t), it worsened the data fitting to *M(t)* and *D(t)* as compared with either Model Variant 1 or 2 (data not shown). This lends greater support to our conclusion that mitotic arrest paired with cell death present across all the stages of the cell cycle governs the number of M- phase radial glia in *kif11* mutants.

Increased apoptosis is a logical predication of our model, as mitotic arrest due to loss of Eg5 function has been shown to lead to cell death (Kozielski et al., 2008; Marcus et al., 2005). We hypothesize that as mitosis arrested cells undergo cell death a progressively toxic environment will be generated over time, which could reduce the survivability of cells at all stages of the cell cycle. We propose that the reductions in the number of cells positive for BrdU incorporation are represented by the loss of cells due to death. Radial glial mitotic arrest and subsequent cell death could reduce the number of proliferating daughter cells (radial glial self-renewal or progenitor cell), which would show less BrdU uptake over time. This speculation is supported by the similar proportion and inverse relationship of cells undergoing death and simultaneously failing to enter S-phase over time (Figure 2.5E,F).

As supported by our mathematical Model Variant 2, we favor the interpretation that decreases in the number of cells in S-phase in *kif11* mutants is the result of less cells due to increased cell death; however, we cannot rule out the possibility that cell cycle entry is being directly altered by changes in cell signaling. Examination of Notch signaling in the outer subventricular zone of the mouse cortex provides some support for a mechanism of daughter-derived mitogenic signaling. Continued proliferation of outer radial glial (oRG) cells through activation of Notch depends on Delta mediated signaling from their daughter cells called intermediate progenitors (Kawaguchi et al., 2008a,

2008b; Shitamukai et al., 2011; Yoon et al., 2008; Zhang et al., 2007). Notch signaling has been demonstrated in the zebrafish neural tube to regulate neuronal and glial cell fate decisions, and asymmetric expression of the Notch signaling regulator Numb is seen in the developing neural progenitor during radial glial division in the mouse cortex (Alexandre et al., 2010; Kim et al., 2008). Therefore it is possible that changes in the number of radial glial derived progenitor cells could alter important daughter-derived signals that serve to maintain the rate of division in the parent stem cell population in the zebrafish spinal cord.

2.4.4 Maintaining size and cell density in the neural tube

If increases in cell death and reductions in proliferation were the only parameters involved, then there should be a reduction in the total number of cells in the neural tube. Interestingly, we showed that the total number of cells, the cross-sectional area of, and resulting cell density within the neural tube were largely unchanged in *kif11* mutants over time as compared with wild type embryos (Figs. 2.1E and Supplemental Figure 2.3). These conflicting results suggest that some compensatory mechanism is actively maintaining neural tube size and cell density. One possible contribution for compensation is the potential for an M-phase cell to actually exit mitosis and undergo cytokinesis. The number of cells in M-phase in *kif11* mutants begins to plateau at 36hpf and then drops after 48hpf (Figure 2.2I). While constant cell death represents a major factor in interpreting cell number in the neural tube of *kif11* mutants, it is possible that some small portion of neural stem cells delayed in M-phase are still successfully completing mitosis and contribute to neurogenesis. However, it is unlikely that a small contribution of successful mitoses can completely account for the maintenance of correct cell densities

particularly over the entire time course.

An active mechanism of feedback regulation may exist to maintain the overall size and proportion of cells that make up the neural tube. Mitotic delays and cell death might logically employ a strategy to increase proliferation in *kif11* mutants, perhaps through a similar mechanism of Notch mediated signaling as described above. However, we documented a decrease in the number of cells in S-phase (Figure 2.5C,D). Alternatively, compensation might be achieved in *kif11* mutants by extending the period of time in which the parental neuroepithelial cell type is maintained for sustained self-renewing symmetrical divisions. We did mathematically model a specific increase in the proliferation of the neuroepithelial population (R_{in}) to theoretically test whether specific alterations to the population of early stem cells might better fit the data; while increases to R_{in} did yield a much closer fit to the magnitude of BrdU positive cell counts, it failed to fit the raw data for mitotic radial glia and cell death (data not shown). An additional, and not necessarily mutually exclusive, mechanism of feedback regulation might involve alterations to cell movement in response to biomechanical changes at the cellular and tissue level. For instance, as cells die in *kif11* mutants, it may change the cell-to-cell forces inside the neural tube in a manner that could reduce the migration of progenitor cells fated to leave the neural tube, such as the dorsally migrating neural crest cells or ventrally exiting perineurial glia (Kucenas et al., 2008; Kuo and Erickson, 2010; Raible et al., 1992). Quantification and live cell imaging of such migratory cell types in and out of the neural tube would be required to test this hypothesized model of altered cell movement due to changes in the physical forces of the developing neural tube.

2.4.5 The timing of Kif11 function during neurogenesis

Although we present evidence that *kif11* is necessary for the mitotic progression of radial glia throughout neurogenesis, it was unclear whether the requirement of Kif11 function varies over this period of development. Using STLC to pharmacologically inhibit Kif11 during different periods of development, we discovered a critical requirement for Kif11 in M-phase radial glial cells between 5 and 10hpf and again between 15 and 20hpf (Figure 2.7). As defined in previous studies, *gfap* expressing radial glia are not present prior to 10hpf in zebrafish (Bernardos and Raymond, 2006; Marcus and Easter, 1995), yet inhibition of Kif11 from 5 to 30hpf with STLC does cause significantly more mitotic arrest in radial glial cells as opposed to the 15–30hpf treatment. These results suggest that at least some aspect of neuroepithelial cell development requires Kif11 for proper cell division. Therefore it is plausible that our time course of Kif11 inhibition captured a pause in observable proliferation that may occur during the natural transition from neuroepithelial cell to radial glial cell development, as opposed to specific temporal changes in Kif11 dependence. Thus, we interpret our temporal analysis of Kif11 function to suggest that Kif11 is consistently required over the course of neural development. To support this idea, a closer examination of cell type specific proliferation rates during the transition of neuroepithelial to radial glial cell development would be required.

2.4.6 Loss of *kif11* provides indirect analysis of the radial glial lineage

Because loss of *kif11* results in arrested radial glial cells that ultimately undergo apoptosis, we hypothesized that we could use these mutants and STLC treated embryos as a system to indirectly determine the neuronal and glial cell types that depend on radial

glia for their generation. Our math model predicts that radial glial cell division is normally dominated by differentiation, such that only ~9% of daughter cells remain as proliferating radial glia while the rest become committed progenitor cells (Table 2.1, 0.182 cells/2 possible outcomes). If a cell type is derived from radial glia, then it should be reduced in number following Kif11 loss. We found that three specific cell populations were reduced in number: secondary motorneurons, commissural secondary ascending (CoSA) interneurons, and oligodendrocyte lineage cells (Figs. 2.8–10). Therefore, we propose that at least a portion of these three cell populations originate from radial glial cells.

In zebrafish, the developing neural tube is composed of both primary neurons and later developing secondary neurons that are temporally regulated and have specific functions (Lewis and Eisen, 2003). Primary neurons are large, born early (9–10hpf), and consist of Rohon Beard sensory neurons, interneurons, and primary motorneurons, whereas secondary neurons are smaller, born later (13–14hpf), and are predominantly composed of interneurons and secondary motorneurons (Beattie et al., 1997; Bernhardt et al., 1990; Kimmel et al., 1994; Lewis and Eisen, 2003; Myers et al., 1986). Labeling for Gfap has shown that radial glia are not specified in the neural tube until 10–12hpf (Bernardos and Raymond, 2006; Marcus and Easter, 1995), suggesting that radial glia in the zebrafish may not significantly contribute to primary neuron populations. Loss of Kif11 supports this later cell fate dependence on radial glia, as early born neuronal populations assayed at 30hpf (Rohon Beard cells, DoLA, VeLD and KA interneurons, and *tg(mnx:GFP)*+ motorneurons) were unaffected, whereas the secondary neuronal cell types assayed (CoSA, and *tg(gata2:GFP)*+ secondary motorneurons) and later-born glial

populations (*olig2*+ dorsal migrating OPCs and oligodendrocytes) were all significantly reduced (Figs. 2.8–10). Importantly, the significant loss of CoSA interneurons nearly matches the total number of GABA+ interneurons lost in *kif11* mutants or STLC treated embryos, suggesting that CoSA interneurons are the only GABA+ interneuron cell type that may be derived from radial glial precursors at these stages. This interpretation is strengthened not only by the consistent proportion of CoSA interneurons being lost over time, but also by the consistent number of DoLA, VeLD and KA interneurons completely unaffected over time (Figs. 2.8 and Supplemental Figure 2.4). Interestingly, while VeLD and KA interneurons were present in correct numbers, we did observe some axonal pathfinding errors by these neurons (Figure 2.8B,F). Increasing evidence is lending support to a distinct role for *kif11/eg5* in axonal growth (Myers and Baas, 2007; Nader et al., 2008, 2012; Barresi, 2010). However, whether the disruption in proper KA and VeLD axonal anatomy is indirectly related to an unhealthy guidance environment or due more specifically to a required role of Kif11 in cytoskeletal dynamics during axonal growth remains to be determined.

OPCs represent an important progenitor cell population for both motorneurons and oligodendrocytes. While we show that *kif11* is co-expressed in a subset of OPCs present at the lumen, we suggest they were originally derived from radial glia. In our assay, nearly all *olig2*+ cells undergoing mitosis were also simultaneously expressing Gfap (Figure 2.10); therefore, we hypothesize that the reduction in dorsal migrating OPCs was most likely due to arrested radial glia that serve to generate OPCs destined for oligodendroglia. These results further support previous studies that suggest a significant portion of oligodendroglial cells have a radial glial origin (Kim et al., 2008; Kirby et al.,

2006; Kriegstein and Alvarez-Buylla, 2009; Park et al., 2004). Furthermore, STLC drug treatments initiated at 24hpf and sustained until 72hpf showed that Kif11-dependent progenitors dividing later in development did not significantly contribute to dorsal migrating OPCs (Figure 2.10D,H,I,K). This suggests that the portion of *olig2*+ cells reduced following our earlier STLC treatment assays originated from radial glial-derived OPCs prior to 24hpf. Based on the cell type markers we have examined, it is possible that proper radial glial development is ultimately required for all later born, secondary neuronal and glial lineages; a speculation that can be tested as additional cell type specific makers become available.

Interestingly, approximately 30–60% of proliferating cells in the neural tube of both wild type and Kif11-deficient embryos did not express Gfap (Figure 2.2G). These non-Gfap-expressing proliferative cells likely represent neuroepithelial or progenitor cells caught in our quantitative analyses. The persistence of these mitotic, non-Gfap-expressing cells following later stage inhibition of Kif11 suggests that potentially some progenitor or transient amplifying cells still require *kif11* for proper progression through mitosis. More detailed marker and lineage analyses are needed to verify and characterize the origin of these *kif11* dependent, Gfap-negative cells.

Our findings identify Kif11/Eg5 as essential for neural stem cells to progress through mitosis during neural tube development in zebrafish. Characterizing mitotic arrest of radial glial cells has revealed critical consequences to cell survival, cell cycle rates, the maintenance of cell density in the neural tube, and the development of secondary neuronal and glial lineages. In addition, the approach of this study demonstrates the predictive powers mathematical modeling can bare on our

understanding of neural development. Further refinement of this model with greater quantitative data about the parameters influencing neural stem cell development will serve to strengthen the accuracy of its predictions and potentially broaden its applicability to other stem cell niches. Lastly, our characterization of the neuronal and glial cell types affected by the loss of Kif11 and subsequent mitotic arrest of radial glia has contributed to our understanding of radial glial derived lineages. It will be important to further this lineage analysis with more direct approaches as well as directly testing the requirement of radial glial cells to the development of certain cell types. Such continued studies of the relatively simple zebrafish neural tube can move the field closer to establishing a comprehensive model of vertebrate neurogenesis.

2.5 Materials and Methods

2.5.1 Zebrafish husbandry and lines used

Zebrafish were maintained according to Smith College Institutional Animal Care and Use Committee (IACUC) and Association for Assessment and Accreditation of Laboratory Animal Care (AAALAC) regulations. Adult fish experienced a 12h light-dark cycle, maintained at ~28°C, and fed a daily diet of live brine shrimp and Gemma Micro (GM) 300 dry mix (Skretting/Bio-Oregon). Embryos were maintained at a constant temperature of 28.5°C in E3 embryo medium according to highly accepted procedures for zebrafish care ((Westerfield, 2007); Zebrafish International Resource Center, ZIRC). Lines utilized in this study were *kif11*^{hi3112a} (provided by N. Hopkins, MIT), AB (wild type) (provided by C. Lawrence, Harvard University), *gfap:EGFP* (provided by P. Raymond, University of Michigan), *olig2:EGFP* (provided by B. Appel, University of

Colorado), *gata2:EGFP* (provided by S. Lin, UCLA), and *mnx1:EGFP* (obtained from ZIRC).

To identify *kif11* mutants, head tissue from labeled *kif11*^{hi3112a} embryos was digested overnight in Proteinase K in TE and genotyped using the Multiplex PCR Kit (Qiagen). The following primers were used: forward 5'-GCA GCC ACT CAC TTT TAA AGT ATG AC-3', reverse 5'-GTG CAG TCC TAA CTA TTG AGT -3', and viral reverse 5'-TCA GTT CGC TTC TCG CTT C-3'.

2.5.2 Reverse-transcriptase PCR

For RT-PCR analysis, *kif11*^{hi3112a} embryos were staged to 48hpf and anesthetized in 4.2% Tricaine methanesulfonate (Argent Chemical Laboratories, MS-222) in E3 (Westerfield, 2007). Tail tissue was preserved in RNAlater (Qiagen, cat. no: 1017980) at -20°C, while remaining tissue was digested overnight in 10mg/mL Proteinase K in TE and processed for embryonic genotyping. Corresponding tail tissue was then processed for RNA isolation and RNA cleanup as previously described (Peterson and Freeman, 2009). RNA cleanup and cDNA synthesis were performed using the Qiagen RNEasy Protect Mini Kit (cat. no. 74124) and the Qiagen QuantiTect Reverse Transcription Kit (cat. no. 205311) respectively per manufacturer instruction and as described (Peterson and Freeman, 2009). PCR on cDNA was performed using the following *kif11* primers: forward 5'-GGT CTA CTC TTA AGC AAG ATC GGC-3' and reverse 5'-CTT CAA TTT GTT TGG CAG AAG GGC-3'. *b-actin* was used as a control: forward 5'-TGG TAT TGT GAT GGA CTC TGG-3' and reverse 5'-AGC ACT GTG TTG GCA TAC AGG-3'.

2.5.3 Pharmacological inhibition of Kif11

S-trityl-L-cysteine (MP Biomedicals), Dimethylenastron (Alexis Biochemicals), and Monastrol (Tocris Bioscience) were each dissolved to 100mM in Dimethyl sulfoxide (DMSO) (Fisher Scientific) and further diluted to 10μM, 100μM, 0.5mM, 0.625mM, 0.75mM, 0.875mM, and 1.0mM in embryo medium (E3). Experimental Kif11 inhibitor and vehicle control (DMSO) embryos were treated at 5hpf and incubated at 28.5˚C until desired age.

2.5.4 *In situ* hybridization and immunohistochemistry

Whole mount and fluorescent *in situ* hybridizations were conducted on 27hpf using the *cb1* probe conjugated to *kif11 (eg5)* mRNA (ZIRC) using published protocols (Jowett, 1997; Thisse & Thisse, 2008). Whole mount immunohistochemistry was conducted as previously described (Barresi et al., 2010) with some modifications. To study neuronal populations (anti-GABA and anti-Islet-1), embryos were fixed in 4% formaldehyde, 0.05% glutaraldehyde, 5mM EGTA, 5mM MgSO4, 0.1% Triton-X in Phosphate buffer (PB) for 1 hour (Dekens et al., 2003). All other antibody labeling was conducted in embryos fixed in 4% paraformaldehyde (Ted Pella) in PB for 2 hours at room temperature or overnight at 4C. The following primary antibodies were used: rabbit anti-goldfish GFAP (1:400, generously donated by Dr. Samuel Nona), mouse anti-acetylated Tubulin (1:800, Sigma), mouse anti-Zrf1 (1:4, ZIRC), mouse anti-phosphohistone H3 (1:1000, Cell Signaling), mouse anti-Islet-1 (39.4D5, 1:200, DSHB), rabbit anti-GABA (1:1000, Sigma), mouse anti-α-Tubulin (1:500, Sigma), mouse anti-

BrdU (G3G4, 5ug/mL, DSHB), and rabbit anti-active Caspase-3 (1:500, BD Pharmingen). Tissue sections were obtained at 14µm thickness with a Leica cryostat and processed for labeling per (Devoto et al., 1996). DNA was visualized in sectioned tissue with Hoechst stain (1:30,000, Invitrogen).

2.5.5 S-phase labeling with BrdU

Embryos were treated with 5-bromo-2'-deoxyuridine (BrdU) as previously described (Kim et al., 2011; Shepard et al., 2004) with slight modifications. Manually dechorionated *kif11*^{hi3112a} embryos were incubated in E3 medium on ice for 5 minutes and then incubated in 10mM BrdU (Sigma, catalog no: B9285) in 15% DMSO/E3 medium for 20 minutes on ice. Embryos were then fixed using 4% paraformaldehyde for 2 hours at room temperature. BrdU detection was performed using anti-G3G4 (anti-BrdU, 5µg/mL, DSHB) as described (Shepard et al., 2004).

2.5.6 Mathematical modeling

Nessy Tania and Christophe Gole, Department of Mathematics, Smith College conducted mathematical modeling. To investigate the difference in the cell division process occurring in wild-type neural tubes as compared with *kif11* mutants, we built and analyzed ordinary differential equation models consisting of three dynamic variables reflecting the number of radial glia cells at different stages of the cell cycle:

- *G(t),* the number of quiescent (non-dividing) radial glial cells at time *t*,
- *S(t)*, the number of radial glia in S-phase at time *t*, and
- *M(t)*, the population of radial glial cells undergoing mitosis at time *t*.

The starting model, built to reflect the dynamics for the wild-type population, is schematically illustrated in the Figure 4A with the exclusion of the cell death variable *(D(t))* used to evaluate *kif11* mutant cell dynamics. Resulting parameter values are presented in Table 1.

The following underlying assumptions were used in constructing the model:

1. We assume that, starting from t_{init} = 10hpf to an ending time t_{end} hpf, neuroepithelial cells generate radial glial cells at a linearly decreasing rate of the form $R_{in}\ (1-t/\ t_{end}\ )$ during that period. At t_{init}, the rate of generation of glial cells is at its highest value, $R_{in}\ (1-t_{init}/\ t_{end}\ ),$ and then begins to decrease, reaching zero at $t_{end.}$ We assume prior to t_{init} = 10hpf, the neuroepithelial population builds up and reaches its peak at 10hpf. The neuroepithelial population then began to decrease by differentiating after 10hpf, which marks the first signs of any *gfap* expression (Bernardos and Raymond, 2006). In our model after t_{end}, we assume most (if not all) neuroepithelial cells have differentiated and do not continue to generate radial glia.

2. In radial glial cells, the cell division process occurs with fixed constant rates. That is, each radial glial cell completes each stage of the cell cycle in a fixed period of time. The following rates used were based on previous measurements of neural stem cell cycle progression in the zebrafish hindbrain (Leung et al., 2011):

$$k_s = \frac{1}{\text{time spent in G1}} \approx \frac{1}{90\ \text{minutes}} \approx 0.667/\text{hour}$$

$$k_m = \frac{1}{\text{time spent in S and G2}} \approx \frac{1}{350\ \text{minutes}} \approx 0.171/\text{hour}$$

$$k_{ou} = \frac{1}{\text{time to complete mitosis}} \approx \frac{1}{25 \text{ minutes}} \approx 2.4/\text{hour}$$

3. Following a cell division, the two resulting daughter cells can turn into progenitor cells or radial glial cells. We assume that asymmetric division occurs with probability *p,* and symmetric differentiation (producing two progenitor cells) occurs with probability q. The remainder of the time, symmetric renewal can also occur (with two radial glial cells produced) with probability *1-p-q*.

Based on these assumptions, the dynamics of the cell populations follow the differential equations:

$$\frac{dG}{dt} = R_{in}\left(1 - \frac{\mathrm{t}}{t_{end}}\right) - k_s G + \phi . k_{out} M,$$
$$\frac{dS}{dt} = k_s G - k_m S,$$
$$\frac{dM}{dt} = k_m S - k_{out} M,$$

where $\phi = [2 - (p + 2q)]$, reflecting the average number of daughter cells (from a radial glial division) that either continue the generation of radial glial cells or become progenitor cells. The value of *f* is restricted between 0 and 2. When $0 \leq \phi < 1$, most daughter cells turn into progenitors. Full asymmetric division corresponds to $\phi = 1$, and if $\phi > 1$, most daughter cells remains as radial glial cells.

Unknown parameter values for this model are obtained by data fitting. The best-fit parameter set, $\bar{p} = \{R_{in}, \phi, t_{end}\}$, is obtained in the least-square sense. That is, given a data set consisting of the number of mitotic radial glial cells at different time points, *(t_i, m_i),* the following objective function is minimized:

$F(\bar{p}) = \sum_i (M(t_i; \bar{p}) - m_i)^2$,

where $M(t_i; \bar{p})$ is obtained by solving the differential equations above at time t_i using the parameter values $\bar{p}$. The least-square problem is numerically solved using a standard constrained optimization package (specifically fmincon in MATLAB). The parameter values are constrained to be positive with further restriction of $0 < \phi < 2$, and $t_{end} > t_{init}$ (as discussed above). We also performed bootstrapping to obtain the 95% confidence interval for each parameter values. 100 data sets were generated by sampling from the Gfap and PH3 double positive raw data presented in Figure 2I. For each data set, constrained least-square optimization was performed; each final parameter value was obtained by taking the mean and the 95% confidence interval was computed.

Table 2.1 – Parameter values characterizing radial glia division in wild type.

Parameter	Definition	Values	95% Interval*
R_{in}	Maximum numbers of radial glia generated by neuroepithelial cells	49.93 cells/hr	47.86 - 52.01
f	Average number of daughter cells that remains as radial glial cells	0.182	0.140 – 0.223
t_{end}	Time at which neuroepithelial cells are fully differentiated	46.15 hpf	44.55-47.75
k_s	Rate of entry into S-phase	0.667/hr	
k_m	Rate of glia entry into M-phase	0.171/hr	
k_{out}	Rate of exit from mitosis	2.4/hr	

*95% confident intervals are given for parameter values obtained from data fitting.

We performed the same procedure to analyze the *kif11*$^{-/-}$ data. We first assumed that the mutation causes a delay in mitotic exit, which was done by decreasing the value of the mitosis exit rate k_{out}. All other parameter values are assumed to remain the same during the acquisition of these models. In addition, we further tested the possibility of changes in the rate of cell death (both Model Variant 1 and 2) and entry into the cell cycle (only Model Variant 1) as important parameters influencing the number of cells seen in *kif11* mutants. To account for potential increases in apoptosis of cells *following mitotic arrest only* (Figure 4A), we added an additional term to the equation for *M(t)*:

$$\frac{dM}{dt} = k_m S - k_{out} M - k_{death} M,$$

and a variable *D(t)*, representing the turnover of the population of dying/dead cells

$$\frac{d\square}{dt} = k_{death} M - k_{clear} D.$$

Here we assumed that a single dead cell is cleared within 3 hours (k_{clear} = 1/3 hr = 0.33/hr), which is based on live cell recordings of apoptotic induced cell death in radial glial cells within the ~48hpf spinal cord (Bashiruddin and Barresi, unpublished observations).

In Model Variant 1, we also evaluated potential reductions in the proliferation rate for radial glia. To do this we allowed the possibility that the G1 phase might be lengthened (reducing the value of k_s). Data fitting was performed to find the best-fit value for all parameters (Table 2).

Table 2.2 – Best-fit parameter values for *kif11* data under Model Variant 1: Mitotic exit delay leading to cell death and reduced cell cycle entry.

Parameter	WT Values	*kif11*$^{-/-}$ Values	Parameter	WT Values	*kif11*$^{-/-}$ Values	*kif11*$^{-/-}$ 95% Interval
R_{in}	49.93 cells/hr	49.93 cells/hr	k_s	0.667/hr	0.0731/hr	0.0667 - 0.0794
f	0.182	0.182	k_{out}	2.4/hr	0.1562/hr	0.1400 - 0.1724
t_{end}	46.15 hpf	46.15 hpf	k_{death}	0	0.0261/hr	0.0163 - 0.0359
k_m	0.171/hr	0.171/hr	k_{clear}	-	0.33/hr	-

Kif11 Model Variant 2 was designed to analyze whether the *kif11*$^{-/-}$ data could be explained by delayed mitotic exit with increased cell death occurring at all stages of the cell cycle (Figure 6A), however this model lacks any slowing of cell cycle entry. To account for additional cell death occurring at G-phase, S-phase, and M-phase, the following terms were added to this model:

$$\frac{dG}{dt} = R_{in}\left(1 - \frac{\mathrm{t}}{t_{end}}\right) - k_s G + \phi . k_{out} M - k_{death1}\, G,$$

$$\frac{dS}{dt} = \square_s G - k_m S - k_{death1}\, S,$$

$$\frac{dM}{dt} = k_m S - k_{out} M - k_{death2}\, M,$$

$$\frac{dD}{dt} = k_{death1}(G + S) + k_{death2}\, M - k_{clear} D.$$

Here k_{death2} corresponds to the death rate due to mitotic arrests while k_{death1} represents the death rate due to other processes (e.g. cell cycle check points or toxicity-induced-death from neighboring apoptotic cells). Data fitting was again performed to find the best-fit value for all parameters under Model Variant 2 (Table 3).

Table 2.3 – Best-fit parameter values for *kif11* data under Model Variant 2: Mitotic exit delay leading to two modes of cell death and no change in cell cycle entry.

Parameter	WT Values	*kif11*$^{-/-}$ Values	Parameter	WT Values	*kif11*$^{-/-}$ Values	95% Interval
R_{in}	49.93 cells/hr	49.93 cells/hr	k_{out}	2.4/hr	0.0106/hr	0.0086 - 0.0127
f	0.182	0.182	k_{death1}	0	0.4372/hr	0.4244 - 0.4499
t_{end}	46.15 hpf	46.15 hpf	k_{death2}	0	0.009/hr	0.0071 - 0.0108
k_s	0.667/hr	0.667/hr	k_{clear}	-	0.33/hr	
k_m	0.171/hr	0.171/hr				

2.5.7 imaging, Quantification and Statistics

Imaging was conducted using structural illumination with the AxioImager Z1 equipped with ApoTome (Zeiss). Z-stacks were collected at an optical slice thickness of 0.53µm at 400X magnification and 0.31µm at 630X magnification for all whole mounts and all sections respectively. All neural tube imaging was performed between somite regions 9 through 13. Images for glial proliferation were captured by an average of 55 optical sections (0.53µm per slice) centered on the midline acquired from a lateral view of the neural tube. Gfap+ somas were identified by their characteristic spherical shape, and secondarily confirmed with colocalization with PH3 and/or Hoechst labeling

depending on the experiment. Data for neuronal populations, BrdU+ nuclei, and activated Caspase-3+ cells were derived from a lateral view of the full Z-stack of the neural tube. Blind cell counts of 3-dimensional Z-stacks and/or maximum intensity projections were conducted manually using the Adobe Photoshop counting tool. Specific neurons in anti-GABA+ and anti-ISL+ populations were identified by location along the D/V axis, soma size, and axon trajectory (Appel and Chitnis, 2002; Appel and Eisen, 1998; Bernhardt et al., 1992; Lewis and Eisen, 2003; Song et al., 2004). Oligodendrocyte progenitor cells visualized with *olig2:eGFP* transgenic embryos were counted at different stages of their development; immature OPCs in the ventral column of the spinal cord showed extensive overlapping GFP expression, therefore they were only counted as either double labeled for PH3 or triple labeled with PH3 and Gfap. However, once a*n olig2*+ cell had begun to emerge from the ventral column and become positioned more dorsally we counted these as "migratory OPCs". All values obtained were conveyed as the mean ± standard error of the mean. Significance of the results was reported using two-tailed t-tests assuming equal variance at an alpha level of 0.05.

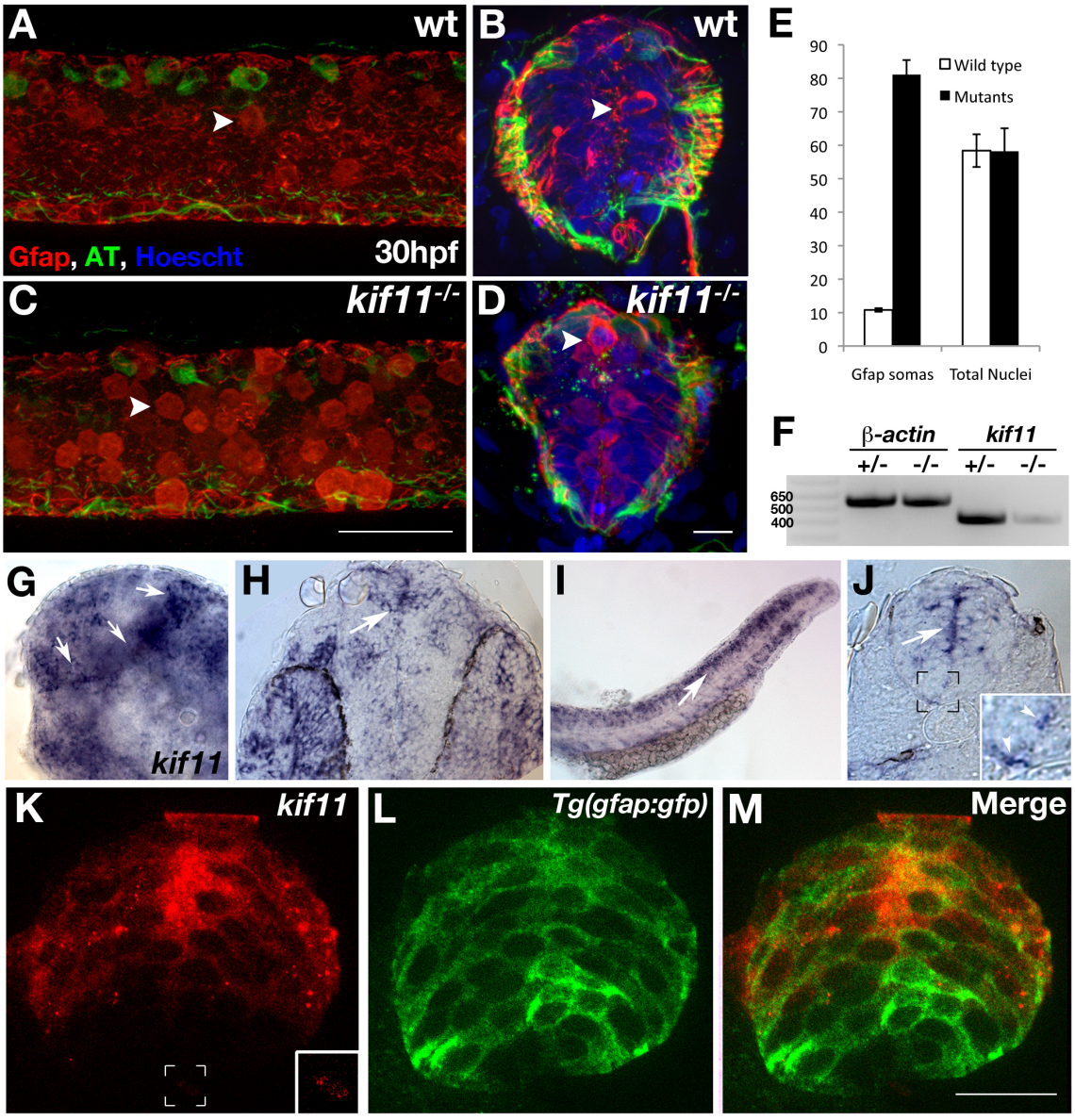

Figure 2.1: Characterization of *kif11* expression in radial glia and its effect on radial glial soma localization. (A-D) *Kif11* siblings were grown to 30hpf and labeled for radial glia (Gfap) and acetylated tubulin (AT) to identify glial and axon defects. In wild type siblings a small population of Gfap+ radial glial somas can be visualized at the luminal surface in a maximum intensity projection of optical sections along the parasagittal plane that encompass the ventricular zone (A) as well as in cross section of the neural tube (B). An increase in the number of radial glial somas can be seen the neural tube of *kif11*$^{-/-}$ mutants (C,D) Scale bar in C = 50μm, scale bar in D = 20μm. (E) Quantification of Gfap+ somas counted from maximum intensity projections of parasagittal optical slices within the neural tube and the total number of nuclei in transverse cross sections of the neural tube showed an 8-fold increase in the number of Gfap+ cell bodies in *kif11*$^{-/-}$ mutants, but no change in the number of total nuclei between siblings. (F) RT-PCR analysis of *kif11* expression between pooled wild type/heterozygote siblings and *kif11*$^{-/-}$ at 48hpf. *β-actin* was used as a loading control. (G-M) Wild type *kif11* mRNA was present

throughout the forebrain (G, lateral; H, dorsal) and trunk (I, J-M) at 27hpf, concentrated at the luminal surface of the VZ (J,K) and into the floor plate (J,K, insets). (K-M) Fluorescent *kif11* detection (K) within a *tg(gfap:EGFP)* embryo (L) shows that *kif11* mRNA is present down the length of the ventricular zone and colocalizes with cells expressing GFP associated with the lumen of the VZ (M). Scale bar = 50μm.

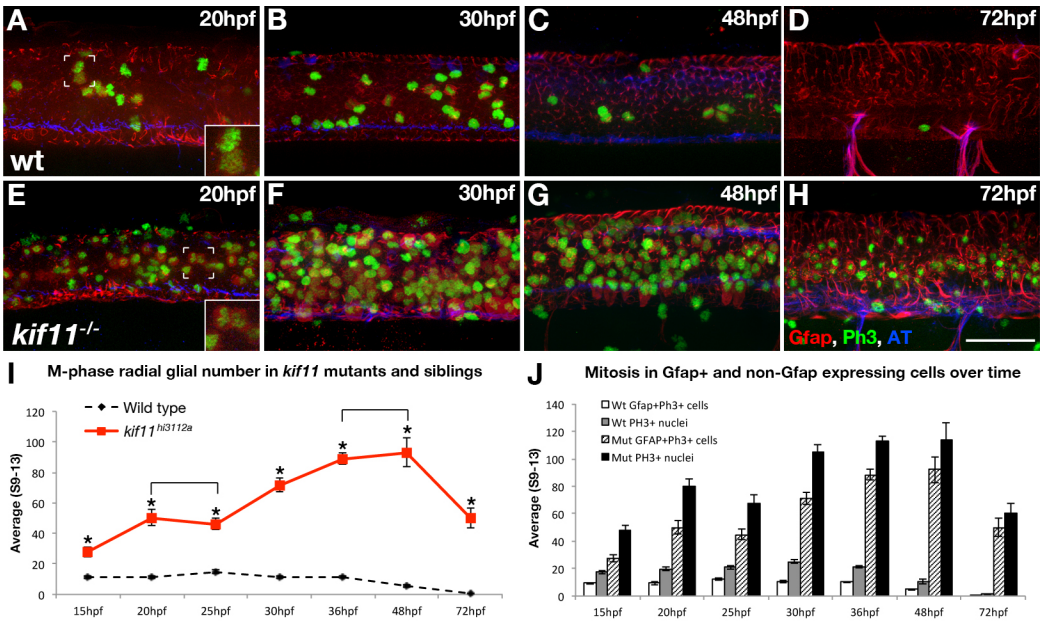

Figure 2.2: Loss of *kif11* causes an accumulation of radial glia in mitosis. (A-H) Lateral views of *kif11*$^{-/-}$ sibling neural tubes fixed at time points throughout neurogenesis and labeled for radial glia (Gfap), anti-phosphohistone H3 (PH3) and acetylated tubulin (AT). Within all siblings, most Gfap+ cells labeled with our antibody were PH3+, indicating these cells were actively proliferating at the time of fixation (A,E insets). At all time points assayed, there were significantly more Gfap+/PH3+ cells in *kif11*$^{-/-}$ embryos compared with wild type siblings (E-H, quantified in I, asterisks), as well as more PH3+ nuclei (J, shaded and black bars). No change in the number of Gfap+ cells was seen between 20-25hpf and 36-48hpf within *kif11*$^{-/-}$ (I, brackets). Of all proliferating cells (J), it was noted that an unidentified population (PH3+, Gfap-) is also *kif11* dependent in both wild type and *kif11*$^{-/-}$ neural tubes. Error bars delineate the standard error of the mean. Asterisks indicate a statistical significance (t-test, two tailed, assuming equal variances, $p<0.05$). Scale bar = 50μm.

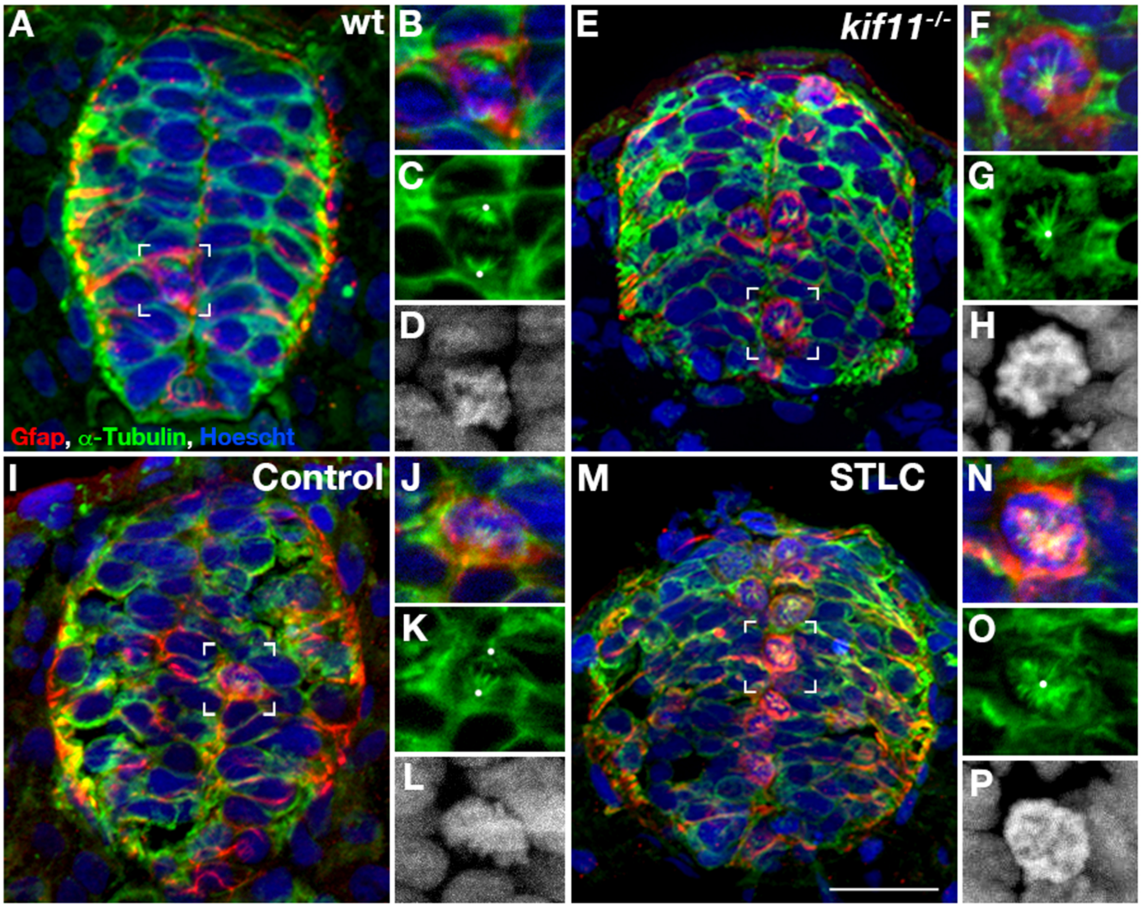

Figure 2.3: **Loss of Kif11 causes monoaster spindle formation in radial glial cells during division.** *Kif11* siblings and wild type embryos treated with either STLC or DMSO control from 5-30hpf were labeled for radial glia (Gfap), microtubules (α-Tubulin) (microtubules), and histones (Hoechst stain) to identify mitotic spindle phenotypes. (A) *Kif11* wild type siblings and (I) vehicle control (DMSO) treated embryos exhibit normal spindles in M-phase (enlarged in B-D and J-L, respectively) while (E) *kif11*$^{-/-}$ mutants and (M) STLC treated embryos display monoastral spindles characteristic of mitotic arrest (enlarged in F-H and N-P, respectively). White dots designate presumptive locations of centrosomes. For greater clarity Hoechst is displayed as a greyscale image in the enlargements (D, H, L, P). Scale bar = 50μm.

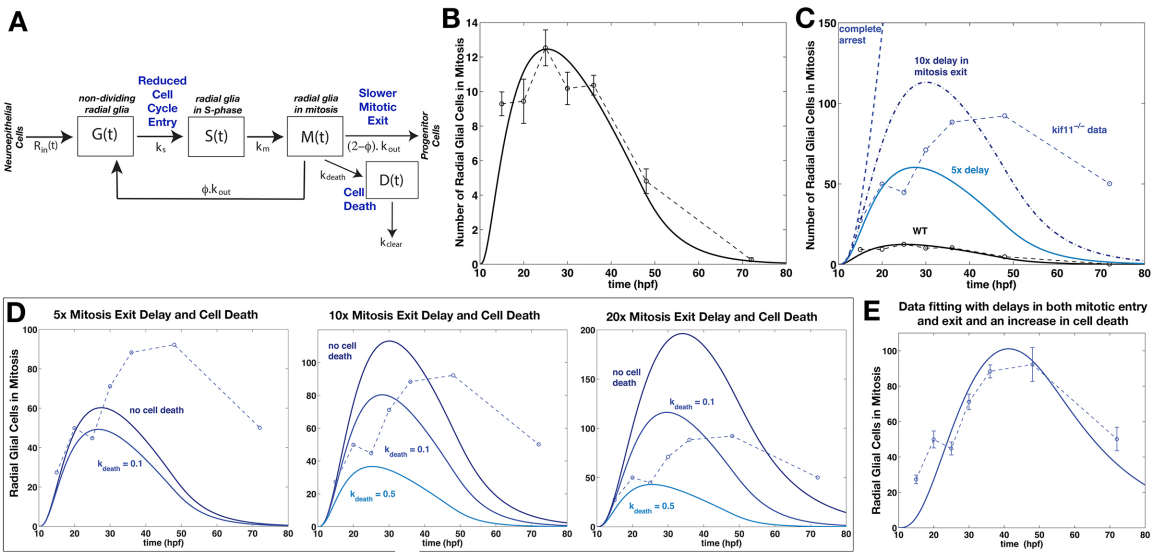

Figure 2.4. Mathematical Model Variant 1 predicts arrested mitosis, cell death, and reduced entry into the cell cycle in *kif11*$^{-/-}$ mutants. (A) Schematic of radial glial cell division through mitosis under Model Variant 1. Assumed changes in *kif11*$^{-/-}$ are shown in blue. Parameter values and their definition are listed in Table 1 (for wild-type) and Table 2 (for *kif11*$^{-/-}$). (B) Best-fit simulation result from the mathematical model showing the dynamics of M-phase radial glia in wild type. (C) Mathematical model testing whether simple accumulation of the number of wild type PH3 positive radial glia can account for the number of mitotic radial glia in *kif11*$^{-/-}$ mutants. Simulation results fail to capture *kif11*$^{-/-}$ data with complete mitotic arrest or a 5x or 10x delay in mitosis exit. (D) Mathematical model testing the combined effects of a 5x, 10x, or 20x delay in mitosis exit with 0%, 10% or 50% cell death occurring in M-phase cells. Mitotic exit delay and cell death alone also fail to capture the full dynamics of *kif11*$^{-/-}$ data. (E) Mathematical modeling of mitosis exit delay with cell death and reduced entry into S-phase achieves a good fit to the *kif11*$^{-/-}$ M-phase radial glial data. (B-E) Raw data is displayed as dashed lines while data fitting curves are represented as solid lines.

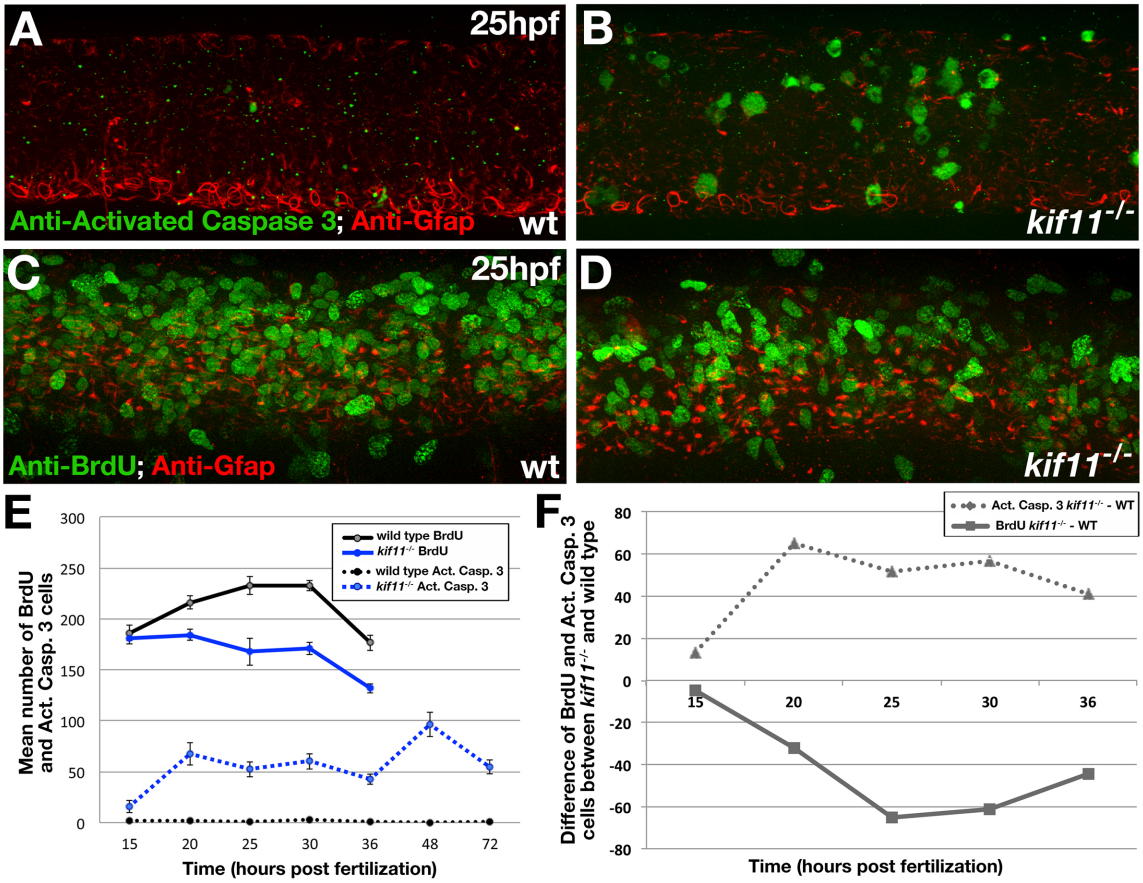

Figure 2.5. *kif11* mutants have inversely proportional changes to the number of cells dying and proliferating. (A,B) Lateral view of the 25hpf neural tube labeled for anti-activated Caspase-3 (green) and anti-Gfap (red) antibodies in wild type (A) and *kif11*$^{-/-}$ mutants (B). (C,D) Lateral view of the 25hpf neural tube labeled for anti-BrdU (green) and anti-Gfap (red) antibodies in wild type (C) and *kif11*$^{-/-}$ (D). (E) Quantification of cell death (dashed lines) and BrdU incorporation (solid lines). Anti-activated Caspase-3 labeling was increased in *kif11*$^{-/-}$ mutants from 15hpf to 72hpf (E, dashed blue line), whereas the number of cells in S-phase was reduced from 20hpf to 36hpf in *kif11*$^{-/-}$ mutants (E, solid black line) as compared with wild type embryos (black lines). (F) Graphical representation of the difference between the amount of dying cells (dashed line) or BrdU positive (solid line) between *kif11* siblings.

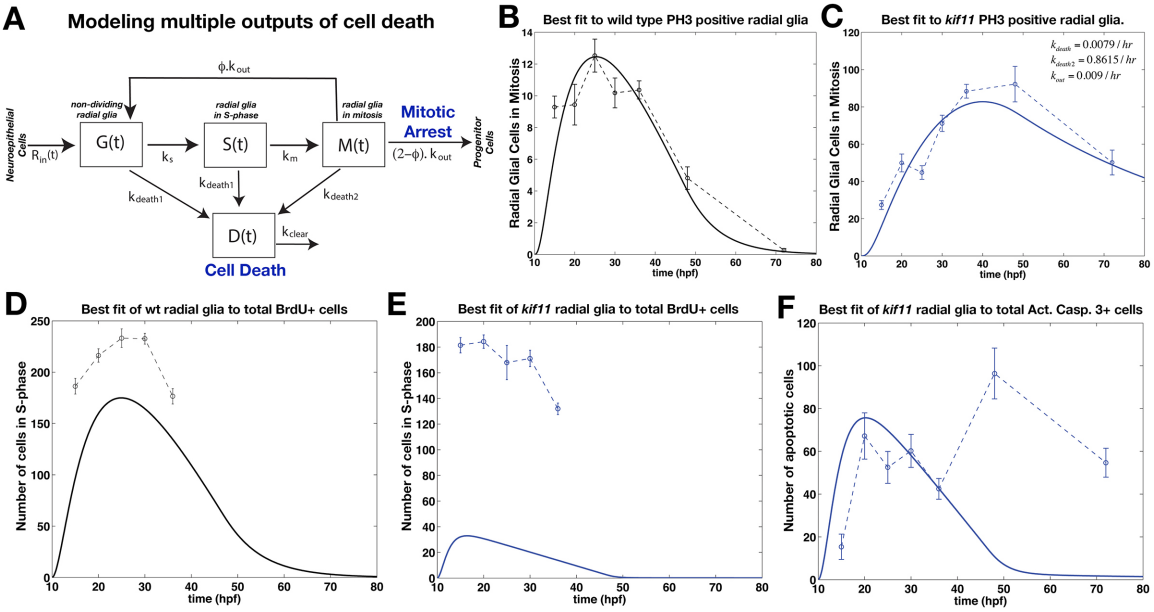

Figure 2.6. Mathematical Model Variant 2 predicts arrested mitosis and two modes of cell death drive the number of M-phase radial glia in *kif11*$^{-/-}$ mutants. Assumed changes impacting *kif11*$^{-/-}$ are shown in blue. (A) Schematic of radial glial cell division through mitosis under Model Variant 2. (B) Mathematical modeling of significant mitosis exit delay with cell death occurring at all stages of the cell cycle achieves a good fit to the *kif11*$^{-/-}$ M-phase radial glial data. (C) Application of the radial glial cell division mathematical Model Variant 2 for data fitting of total cell counts for anti-Activated Caspase-3 positive cells in *kif11*$^{-/-}$ mutants. (D, E) Application of the radial glial cell division mathematical Model Variant 2 for data fitting of total cell counts for BrdU incorporation in wild type (D) and *kif11*$^{-/-}$ (E). (B-E) Raw data is displayed as dashed lines while data fitting curves are represented as solid lines.

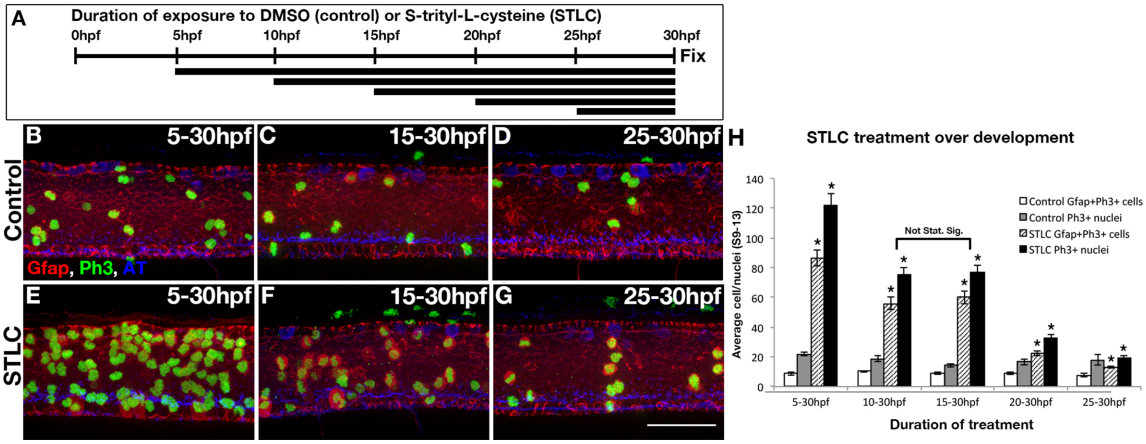

Figure 2.7: Kif11 function is most required during two distinct periods for proper cell division. (A) Schematic illustrating time of exposure to S-trityl-L-cysteine (STLC) or vehicle control (dimethyl sulfoxide) and duration of treatment between groups. (B-G) Lateral views of post-treatment embryos labeled for radial glia (Gfap), Ph3 and AT. (H) In all test groups, there were significantly more Gfap+/Ph3+ and Gfap-/Ph3+ cells in STLC treated embryos (E-G) compared with their controls (B-D) at 5-30hpf, 10-30hpf, 15-30hpf, 20-30hpf, and 25-30hpf. Error bars delineate the standard error of the mean. Asterisks indicate a statistical significance (t-test, two tailed, assuming equal variances, $p<0.05$). Scale bar = 50μm.

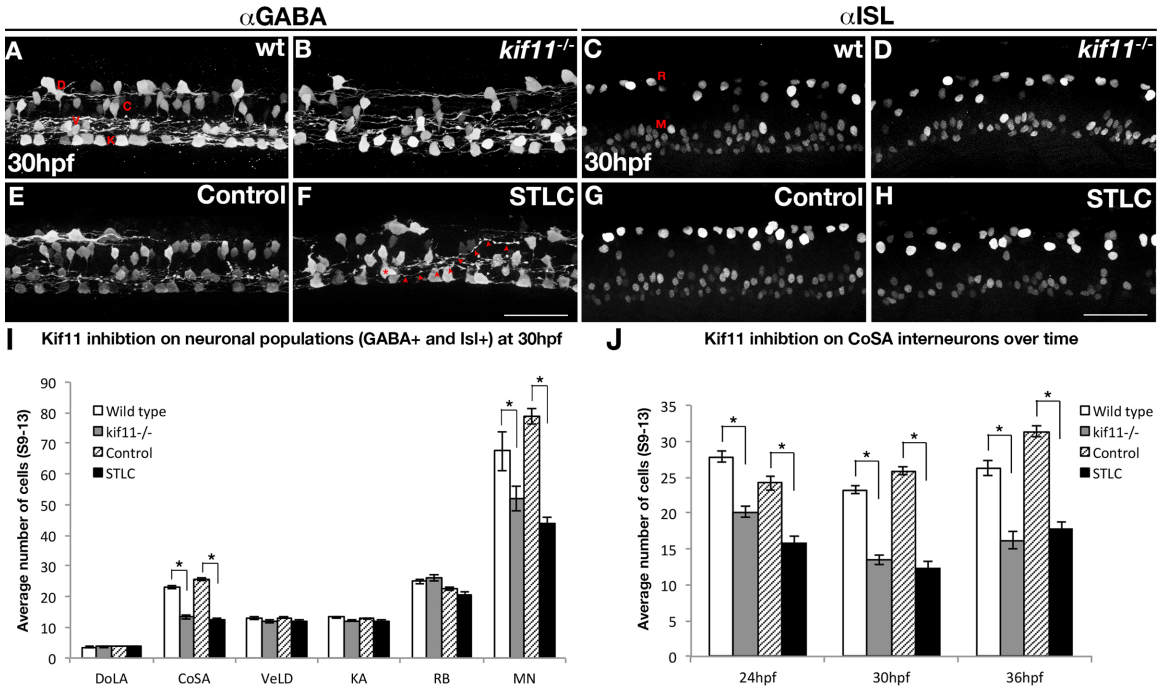

Figure 2.8: Kif11 is required for motorneurons and CoSA interneurons. Wild type/vehicle control (A,C,E,G) and *kif11*$^{-/-}$/STLC treated embryos (B,D,F,H) were labeled for anti-GABA (A,B,E,F) to label distinct DoLA, CoSA, VeLD, and KA interneurons (denoted D,C,V, and K, respectively), as well as anti-ISL (C,D,G,H) to label Rohon Beard sensory neurons and motor neurons (denoted R and M, respectively). Decreases in GABA+ cell populations as well as axon pathfinding errors were found in Kif11 deficient embryos as compared with controls (asterisks in B and F label cell body, arrowheads mark axon trajectory). (I) Quantification of neuronal populations identified decreases specifically in CoSA and MN populations within Kif11 deficient embryos (asterisks, $p<0.05$) as compared with controls. (J) Time course analysis of GABA+ cell types at 24hpf, 30hpf and 36hpf shows a consistent number of GABA+ cells both lost and retained over time in *kif11* mutants and STLC treated embryos. Scale bar = 50μm.

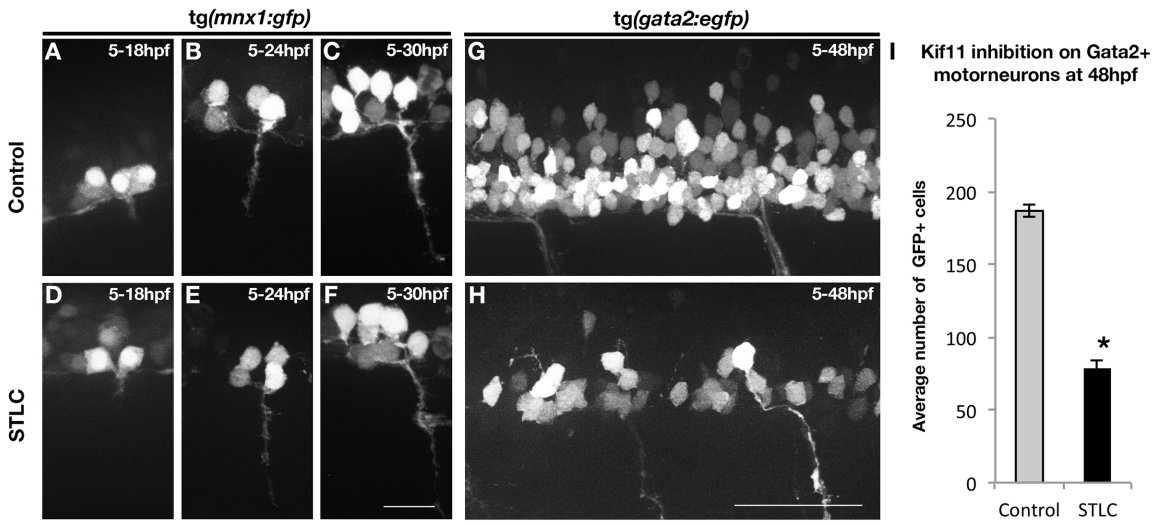

Figure 2.9: Kif11 is required for secondary motorneurons but not primary motorneurons. (A-F) Visualization of primary motorneuron development in somite 11 over time using the *tg(mnx1:GFP)* transgenic line. No difference in the formation of primary motorneurons was observed in STLC treated *tg(mnx1:GFP)* transgenic embryos (D-F) as compared to control DMSO treated embryos (A-C). Scale bar = 20μm. (G,H) Lateral view of the neural tube of *tg(gata2:EGFP)* transgenic embryos at 48hpf to assess secondary motorneurons in control DMSO treated (G) or STLC treated transgenic embryos from 5-48hpf (H). (I) A significant decrease in GFP+ neurons was seen in STLC treated *tg(gata2:EGFP)* embryos. Error bars delineate the standard error of the mean. Asterisks indicate a statistical significance (t-test, two tailed, assuming equal variances, $p<0.05$). Scale bar = 50μm.

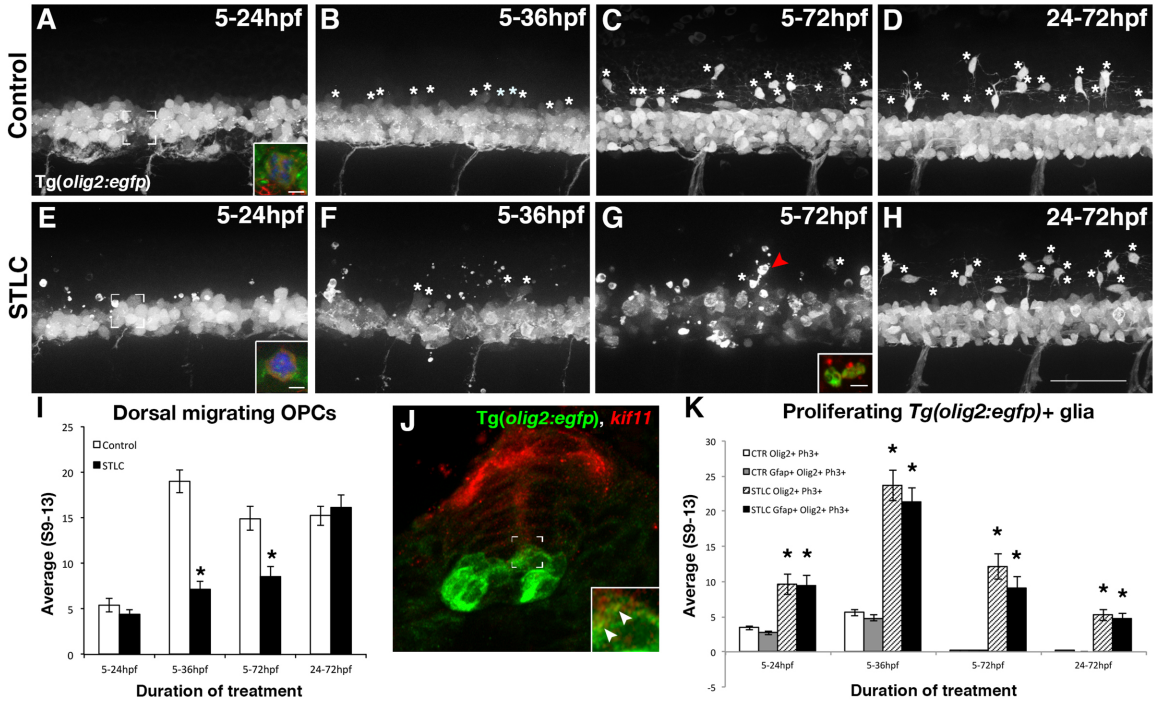

Figure 2.10: Kif11 is required for oligodendrocyte development. Lateral views of *tg(olig2:EGFP)* embryos treated with either vehicle control (A-D) or STLC (E-H) at 5hpf and fixed at time points critical for oligodendrocyte development (5-24hpf, 5-36hpf, 5-72hpf, and 24-72hpf). Dorsal migrating OPCs (white asterisks) were present in control embryos older than 24hpf (B-D), which were significantly reduced in STLC treated groups (F-H, quantified in I, black asterisks $p>0.05$), except when treated from 24-72hpf (no statistical significance from the vehicle control, $p>0.51$). Irregular GFP+ fragments (G arrowhead) co-labeled with anti-Activated Caspase-3 (G, inset, red fluorescence) indicative of cell death. (J) *Kif11* mRNA detection within 27hpf *tg(olig2:EGFP)* embryos indicated that a small portion of *olig2* cells associated with the ventricular zone colocalize with *kif11* expression (J inset, arrowheads). Triple-labeled (GFP+, Ph3+, Gfap+) cells were identified in most control and treatment groups (A,E brackets; insets are maximum intensity projection of extracted Z-stack series in A,E; quantified in K), and were significantly increased in all STLC treated groups (K, asterisks). Error bars delineate the standard error of the mean. Asterisks indicate a statistical significance (t-test, two tailed, assuming equal variances, $p<0.05$). Scale bar in H = 50μm, scale bar in insets of E,G = 5μm.

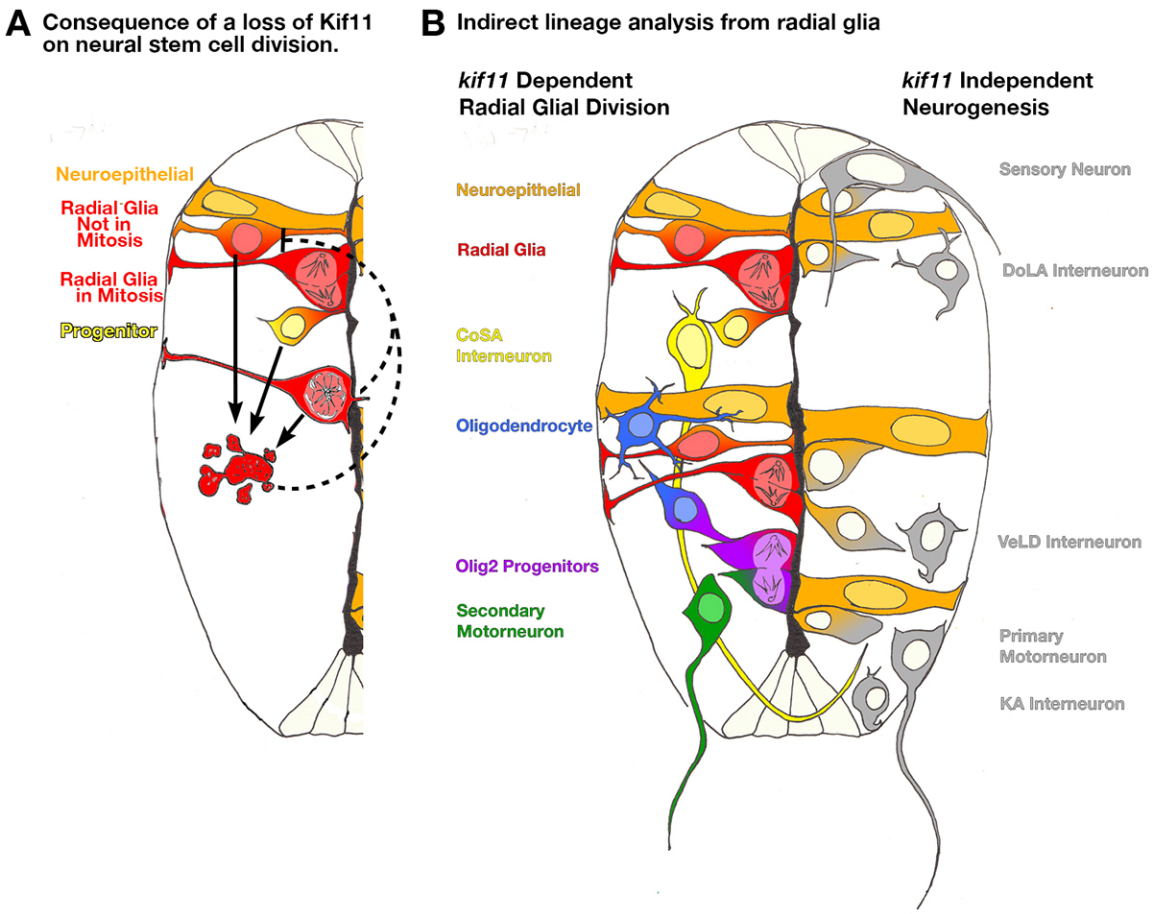

Figure 2.11. Model of the role Kif11 plays in neural stem cell division and neurogenesis. (A) Illustration of one half of the neural tube depicting the consequences of a loss of *kif11* to neural stem cell division. Neuroepithelial cells (orange) transition into radial glial cells (orange/red) that undergo division at the ventricular surface to generate progenitor cells (yellow) and/or additional radial glia (red). Upon loss of *kif11,* radial glia cells arrest in mitosis (lower red cell with monoaster spindle), which leads to increases in cell death (red apoptotic cell exhibiting cell blebbing). We propose that cell death is progressively initiated in cells at all stages of the cell cycle as opposed to cells just arrested in mitosis (three arrows). Moreover we propose that the consequential loss of cells by apoptosis will show reductions in the number of cells entering S-phase; however, we cannot rule out that negative feedback on neighboring parental stem cell populations signals a slow down in cell cycle entry (dashed inhibitory lines). (B) Examination of neuronal and glial cell fates in *kif11*$^{-/-}$ mutants provides an indirect method of lineage tracing from radial glial cells. Along the left side of this illustrated spinal cord shows the cell types that require Kif11 function, and therefore likely possess radial glial origins. Cell types that were patterned normally in the absence of functional Kif11 are illustrated along the right side of this spinal cord, and thus likely are not derived from radial glia.

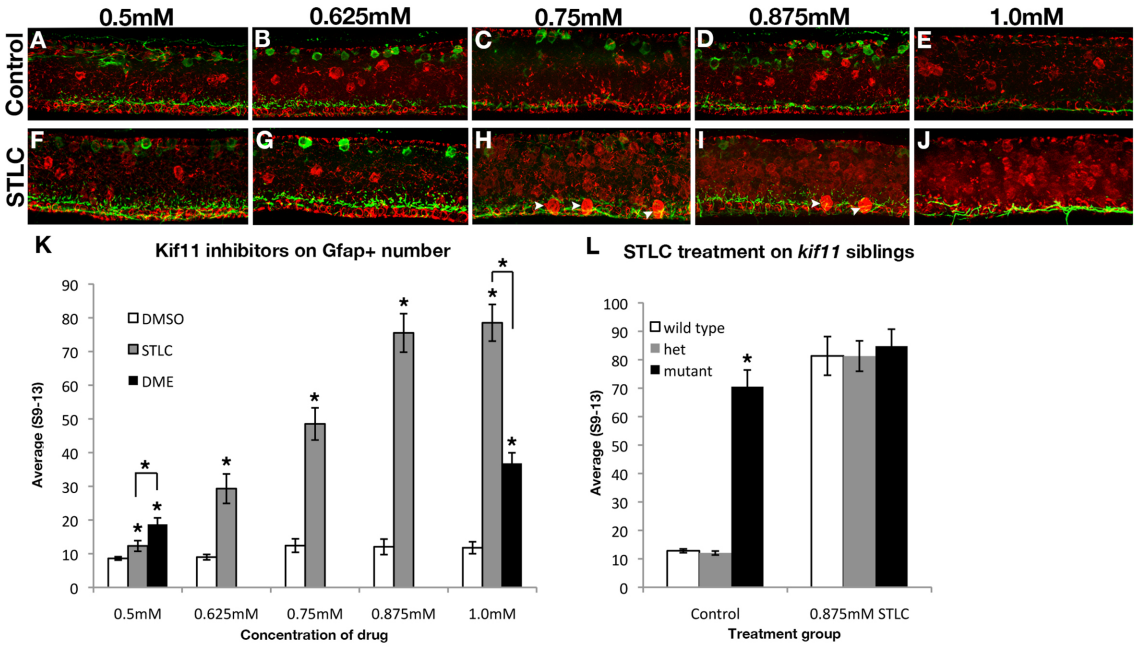

Supplemental Figure 2.1: STLC treatment phenocopies *kif11*$^{-/-}$ mutants without causing additional morphological deformations. Lateral views of wild type neural tubes after treatment from 5hpf to 30hpf with various concentrations of either the vehicle control (dimethyl sulfoxide, A-E) or S-trityl-L-cysteine (STLC, F-J). Astroglial and axon changes were visualized by labeling for Gfap and acetylated Tubulin (AT). No change in radial glial soma number was seen in DMSO control embryos at any concentration tested. Gfap+ floorplate somas (arrowheads) were only seen at higher concentrations of STLC (H-J). (K) Quantification of the average Gfap+ soma number following Kif11 inhibition. The lowest concentration of DME (0.5mM) caused an increase in GFAP+ cell bodies, however extreme gross morphological defects were also noted therefore this drug was not further processed. Gfap+ cell body number was increased in STLC concentrations higher than 0.625mM (grey bars, asterisks). (L) A maximum concentration of 0.875mM phenocopied the *kif11* mutant. No additive effects were seen or quantified when *kif11*$^{-/-}$ mutants were treated with 0.875mM STLC (L, black bars, data not shown). There was no statistically significant difference seen between STLC-treated wild type, heterozygous *kif1*$^{+/-}$, and homozygous *kif11*$^{-/-}$ (L). Error bars delineate the standard error of the mean. Asterisks indicate a statistical significance (t-test, two tailed, assuming equal variances, $p<0.05$).

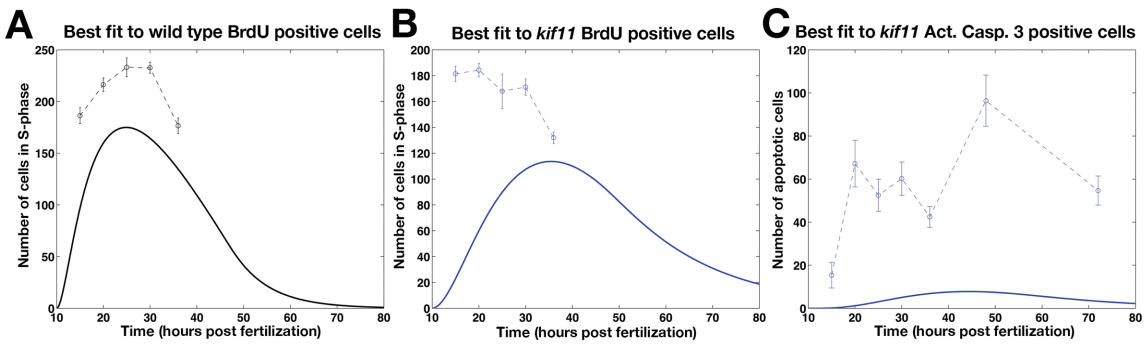

Supplemental Figure 2.2. Mathematical Model Variant 1 does not fit the raw BrdU or Cell death data counts. (A,B) Application of the radial glial cell division mathematical Model Variant 1 for data fitting of total cell counts for BrdU incorporation in wild type (A) and *kif11*$^{-/-}$ (B). (C) Application of the radial glial cell division mathematical Model Variant 1 for data fitting of total cell counts for anti-activated Caspase-3+ positive cells in *kif11*$^{-/-}$ mutants. Raw data is displayed as dashed lines while data fitting curves are represented as solid lines.

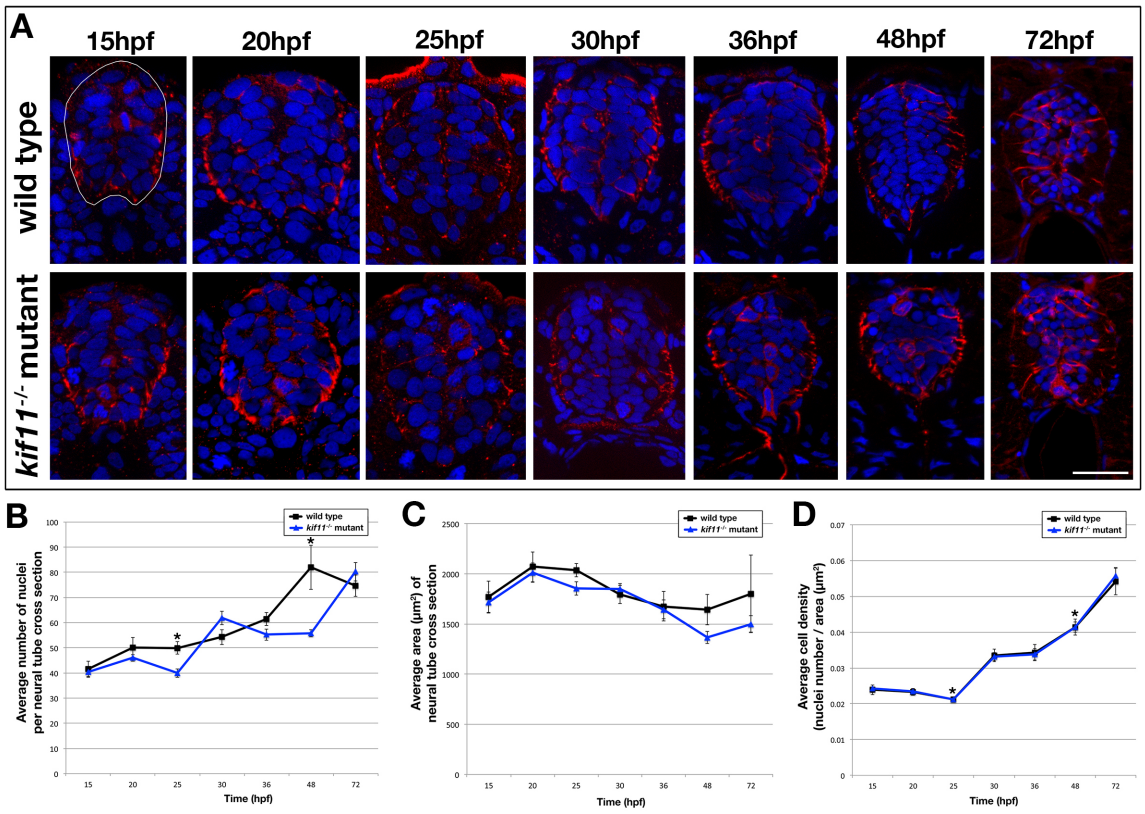

Supplemental Figure 2.3. Cell density in the *kif11*$^{-/-}$ neural tube is unchanged. (A) Cross sectional analysis of Gfap-positive astroglia (red) and Hoechst-positive nuclei (blue) in the developing spinal cord over time from 15hpf to 72hpf in wild type (top row) and *kif11*$^{-/-}$ mutants (bottom row). The cross sectional area of the neural tube was calculated for each section following manual outlining of the neural tube, which was based on Gfap labeling that delineates the outer edges of the neural tube (white line shown in 15hpf wild type image). (B-D) Quantification and data analysis of cell densities in the neural tube. Three sections corresponding to the axial locations of approximately somite 4-6, 10-12, and 16-18 were collected per embryo. 4 embryos were counted per time point. A resulting total of 12 sections were counted for 15-30hpf and 48hpf time points, and 11 sections were counted for 36hpf and 10 sections for 72hpf. Nuclei and area counts were averaged for each time point, and are shown on each example image (A). Only the 25hpf and 48hpf time points showed a statistically significant decrease in the number of nuclei in the *kif11*$^{-/-}$ mutant (blue line) neural tube as compared with wild type controls (black line) (B, asterisks). No statistically significant difference was seen in the cross sectional area of the neural tube between *kif11* siblings (C). (D) Calculated cell density in the neural tube showed no visible difference between *kif11* siblings (C, overlapping blue and black lines); however both 25hpf and 48hpf continued to be statistically significantly different (asterisks; 25hpf, $p=0.004$; 48hpf, $p=0.004$). Error bars delineate the standard error of the mean. Asterisks indicate a statistical significance (t-test, two tailed, assuming equal variances, $p<0.05$). Scale bar = 50μm.

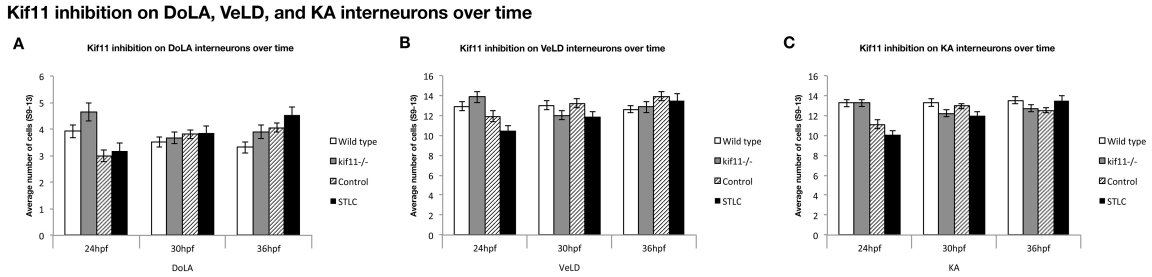

Supplemental Figure 2.4. No change was seen in DoLA, VeLD, or KA interneurons over time in Kif11 deficient embryos. (A-C) Quantification of DoLA (A), VeLD (B), or KA (C) interneurons in wild type (white bars), *kif11*$^{-/-}$ (grey bars), DMSO control (hashed bars) or STLC treated embryos (black bars) at 24hpf, 30hpf, and 36hpf. The numbers of DoLA, VeLD, and KA interneurons were consistent across time points and showed no statistically significant difference between *kif11*$^{-/-}$ mutant or STLC treated embryos and their respective controls.

2.6 Supplemental Information

We conducted a screen of several known Kif11 (Eg5) inhibitors on wild type embryos and compared the resultant radial glial phenotype to that of the mutant (Supplemental Figure 1, A-L). Preliminary drug treatments using Monastrol, Dimethylenastron (DME), S-trityl-L-cysteine (STLC), or the vehicle control (DMSO) were administered at initial concentrations of 0.5mM and 1.0mM in wild type embryos beginning at 5hpf (prior to MBT) until 30hpf to recapitulate the zygotic-derived phenotype in *kif11* mutants. We found that Monastrol is not a potent Kif11 inhibitor in zebrafish and caused no change in Gfap+ cell number (data not shown), even though it has been tested successfully on algae, *Xenopus* oocytes, and glioblastoma cell lines (Kapoor et al., 2000; Muller et al., 2007; Peters and Kropf, 2006). DME treated embryos exhibited an increase in M-phase radial glia within the spinal cord at both 0.5mM and 1.0mM compared to the control (Supplemental Figure 1M, $p<0.001$), but also caused severe defects within the spinal cord along with overall gross morphological defects not seen in the mutant (Supplemental Figure 1, K-L). No significant difference was seen in M-phase radial glia at 0.5mM STLC as compared to the control ($p=0.77$), however, a significant increase was seen in the 1.0mM treatment ($p<0.001$). An additional trial using intermediate concentrations (0.625, 0.75, 0.875mM) of STLC was next attempted, and we found that both 0.875mM and 1.0mM phenocopied the mutant with a significant increase in the number of Gfap+ cell bodies in comparison to the control ($p<0.001$), along with presence of enlarged Gfap+ floor plate cells (H-J, arrowheads). Although no significant difference was found in M-phase radial glial number in embryos treated with 0.875mM and 1.0mM STLC ($p=0.33$), an increase in mortality was noted in the higher concentrations. Therefore,

0.875mM was determined to be the best concentration that phenocopied the mutant and was used for subsequent trials.

CHAPTER 3

GFAP-POSITIVE RADIAL GLIA ARE THE PROGENITOR POPULATION FOR LATER BORN NEURONS AND GLIA

Sections contained within this chapter are adapted from the original research article *in submission*: Johnson K, Bashiruddin S, Barragan J, Smith CJ, Tyrrell C, Parsons MJ, Doris R, Kucenas S, Downes GB, Velez C, Sakai C, Pathak N, Anderson K, Stein R, Devoto SH, Mumm JS, Barresi MJF (2015) Gfap-positive radial glial cells are an essential progenitor population for later born neurons and glia in the zebrafish spinal cord. *Glia*.

3.1 Introduction

The central nervous system (CNS) is a complex organ that requires tight regulation of neural stem cell (NSC) division and differentiation in order to generate a properly patterned network of neuronal and glial cells. To understand how these mechanisms are regulated during neural development requires not only an understanding of the timing and location for the generation of specific cell populations, but also an understanding of the lineage contributions of neural progenitor populations.

During neural development, the coordinated actions of neuroepithelial cells, radial glia, and intermediate progenitor cells generate and pattern all of the neurons and glia necessary to construct the CNS, however little work discerning the individual contributions of any one population in the embryonic spinal cord have been conducted.

Recently, it was shown that radial glia act as the predominant neural stem cell during vertebrate embryonic and fetal brain development, a responsibility retained in the zebrafish adult brain (Malatesta et al., 2000; Noctor et al., 2001; Kim H et al., 2008b; reviewed in Kriegstein and Alvarez-Buylla, 2009). Radial glia conserve many characteristics of their neuroepithelial progenitors, such as retention of neural progenitor markers (Lam et al., 2009; Jao et al., 2012; Briona & Dorsky 2014), maintenance of

apical-basal polarity, and translocation of the nucleus to the lumen prior to division (Gotz & Huttner, 2005). Importantly, while neuroepithelial cells and radial glia express the neural progenitor markers nestin, vimentin, and Sox1/2/3 (Barry & McDermott 2005; Schmidt et al., 2013), radial glia can be elucidated as a molecularly distinct population through upregulation of the glial specific genes *gfap* (glial fibrillary acidic protein), *slc1a3a* (GLAST, astrocyte-specific glutamate transporter), *s100b* (calcium binding protein), and *blbp* (brain lipid binding protein) (Gotz & Huttner 2005;). While it is widely accepted that the intermediate filament Gfap is the most common and comprehensive marker for radial glia and astrocytes (Bignami & Dahl, 1977; Zhang, 2001), the radial glial population can be further refined along the dorsoventral axis of the spinal cord by expression of region specific genes, such as *dbx1* in radial glia of the intermediate spinal cord (Briona & Dorsky, 2014) or *olig2* in radial glia of the ventral spinal cord (Kim H et al., 2008b; Kim S et al., 2008).

We previously reported that loss of the kinesin motor protein *kif11* caused significant mitotic delays and death within the Gfap+ radial glial population (Johnson et al., 2014). This disruption in radial glial division led to a loss of neural progenitor function, and resulted in specific reductions of later born CoSA interneurons, secondary motorneurons, and oligodendroglial populations while early-born neuronal numbers were not affected. Though these results suggest that proper radial glial division and survival is necessary for the generation of specific later-born lineages, this indirect approach leaves the possibility that other *kif11* dependent progenitor populations also contributed to the development of these cell types.

To broadly label the radial glial population and assay their roles as a progenitor population during neural development, we generated a novel *gfap:nls-mCherry* line that drives nuclear expression of mCherry within Gfap+ cells. We showed that the *gfap:nls-mCherry* line recapitulates Gfap expression throughout neural tissues through comparison with established transgenic lines. Further, we identified that the *gfap:nls-mCherry* line allows identification of distinct, individual *gfap*+ cells exhibiting radial glial morphology within the spinal cord coexpressing neural stem cell markers, supporting the hypothesis that Gfap+ radial glia act as a progenitor population during CNS development. Lastly, we demonstrate that subsets of interneurons, secondary motorneurons, and oligodendroglia originate from Gfap+ radial glia. Overall, this approach explores the progenitor properties of Gfap+ radial glia and conclusively defines the cell lineages these radial glial give rise to during embryogenesis in the zebrafish spinal cord.

3.2 Experimental Strategy

In this study, we generated a *gfap*-driven nuclear mCherry reporter line to discretely label the nuclei of radial glia and their derivatives. The *tg(gfap:nls-mCherry)* transgenic line uses the regulatory elements of the zebrafish *gfap* gene (7.4kb of sequences from the 5'UTR, Exon1, and Intron1; Bernardos & Raymond, 2006) to drive expression of a mCherry reporter fused with a nuclear localization signal (*nls*) within Gfap+ cells. Using this approach, we are able to distinguish individual Gfap+ nuclei throughout the densely populated neuroepithelium and characterize the cell types that showed inheritance of the mCherry reporter. We first examine cells co-expressing *gfap* driven nls-mCherry with the known neural stem cells markers *nestin* and *sox2*. In

addition, we take advantage of the stability of the mCherry reporter to determine co-expression with markers of differentiated cell types to identify the lineages derived from the radial glial stem cells.

3.3 Results

3.3.1 Nuclear expression of mCherry recapitulates onset of *gfap* expression and labels spinal cord radial glia.

Faint expression of mCherry was first evident in *gfap:nls-mCherry* embryos during formation of the neural plate at tail bud stage (10hpf) (Figure 3.1A-A'), similar to observations made in the established *gfap:eGFP*^{mi2001} line that shares the same regulatory elements (Bernardos & Raymond, 2006). By late neural keel stage (15hpf), increased mCherry expression could be detected in neural tissues, including the developing eye (Figure 3.1B-B'). Following formation of the neural tube by 24hpf, mCherry was predominantly restricted to neural tissues, and was brightest throughout the forebrain, eye, hindbrain, and spinal cord (Figure 3.1C-C'). To confirm that the expression pattern of nuclear mCherry was being driven in the same cells as the original *gfap* reporter line, *gfap:nls-mCherry* was crossed with *gfap:eGFP*^{mi2001} and coexpression of the two fluorescent labels were detected throughout all neural tissues at 24hpf (Figure 3.1D). Closer examination of the spinal cord in cross section revealed complete coexpression of mCherry+ nuclei within GFP+ cells at 24hpf (Figure 3.1E) maintained throughout embryonic neurogenesis by 72hpf (Figure 3.1F), many of which exhibited a radial morphology indicative of radial glial cells as delineated by cytoplasmic GFP.

To determine whether our novel transgene targeted mCherry specifically to the nuclei of radial glial cells, we labeled cross sections of *gfap:nls-mCherry* embryos with anti-Gfap and assayed for radial glial morphology. At 24hpf, many of the nuclei present in the neural tube were mCherry+ (Figure 3.2A), which were positioned throughout the neural tube with Gfap+ radial fibers extending towards the nuclei in close association with the lumen (Figure 3.2B,C). Closer analysis through single optical sections revealed that most mCherry+ nuclei were found within anti-Gfap-labeled cell bodies positioned at the lumen and extending radial fibers towards the pial surface (Figure 3.2A'), which represent the classic hallmarks of radial glial morphology (Kim H et al., 2008b; Tawk et al., 2007). By 48hpf, nls-mCherry readily labeled a large portion of nuclei present around the lumen (Figure 3.2D), along with a small portion of dimly expressed mCherry nuclei devoid of anti-Gfap labeling. These dim mCherry+ cells are likely differentiated cells that retained fluorescence from the originating *gfap*+ progenitors, similar to observations made in the related *gfap:eGFP*^{mi2001} line (Bernardos & Raymond, 2006; Kim et al., 2008). Extensive networks of nls-mCherry and Gfap double-positive radial glia were seen along the dorsoventral axis of the spinal cord (Figure 3.2D',E,F) were also present by 48hpf By 72hpf, bright mCherry+ nuclei were predominantly found along the central canal (Figure 3.2G) that retained long Gfap+ processes towards the pial surface (Figure 3.2G',H,I). Dim mCherry+ cells absent for anti-Gfap were also found in the dorsal spinal cord, again likely differentiated neurons similarly observed in previous experiments at 72hpf (Bernardos & Raymond 2006). Therefore, we conclude that the *gfap:nls-mCherry* line accurately labels radial glial cells throughout embryonic development, and propose

that it may also act as a temporary lineage tracer for cells derived from *gfap*+ progenitor cells.

3.3.2 The neural progenitor marker Nestin is expressed in *gfap*+ populations.

To further characterize whether the radial glial populations labeled by the *gfap:nls-mCherry* transgene represent neural stem cells, we examined colocalization of mCherry with Nestin, a neural progenitor marker (Hockfield & McKay, 1985; Lam et al., 2009). To identify whether *gfap*+ radial glial cells coexpress Nestin, we crossed the *gfap:nls-mCherry* line with *tg(-3.9nestin:GFP)*, which uses 3.9kb of the *nestin* regulatory region and promoter sequence to drive cytoplasmic GFP throughout *nestin*+ cells (Lam et al., 2009). To facilitate the simultaneous identification of *nestin*+ and radial glia cells, cryosections from double-expressing embryos were labeled with anti-GFP (to boost signal of the *nestin*-driven transgene that we observed to be weak at earlier time points) as well as anti-Gfap. At 24hpf, cytoplasmic *nestin:*GFP+ labeling was visualized throughout the neural tube, and this expression colabeled with a majority of the cellular populations expressing mCherry+ nuclei (Figure 3.3A). By later time points, nearly all *nestin:*GFP+ cells emanating from the ventricular surface possessed mCherry+ nuclei and anti-Gfap+ radial morphology (Figure 3.3B,C). By 72hpf, *nestin:*GFP+, mCherry+ radial glial cells continued to colabel with anti-Gfap and were primarily localized in the ventral spinal cord around the central canal (Figure 3.3C). These results suggest that *gfap* and *nestin* are coexpressed in the same progenitor populations over the course of spinal cord development in the embryo. Importantly, we also observed *nestin*-driven GFP and *gfap*-driven mCherry double positive cells that lacked expression of Gfap protein and radial morphology. These *nestin:*GFP+/mCherry+, non-radial glial cells were located in regions

either away from the lumen or along the floorplate (Figure 3.3C, arrowheads), and quantification showed this population increased in number between 48hpf and 72hpf (48hpf ventral cell avg. = 0.73±0.21 per embryo; 72hpf ventral avg. = 2±0.35 per embryo; $p<0.004$). Taken together, these data demonstrate that the *tg(-3.9nestin:GFP)* and *tg(gfap:nls-mCherry)* lines label the same neural progenitor populations during embryonic neural development in zebrafish.

3.3.3 A pool of *gfap*+ radial glia are retained as a neural stem cell population throughout neurogenesis.

Sox2 is a known essential factor for neural progenitor maintenance and development in embryonic and adult neural tissues, and its expression is actively down regulated upon differentiation (Okuda et al., 2010; Graham et al., 2003; reviewed in Schmidt et al., 2013). We hypothesized that if *gfap*+ radial glial cells represent a majority of the neural stem and progenitor populations, then they should also express Sox2. Previous attempts to identify Sox2+ radial glia using *gfap:GFP*^{mi2001} lines have proved problematic, as the anti-Sox2 is a nuclear label and therefore does not cleanly colocalize with cytoplasmic GFP (Lam et al., 2009; Jao et al., 2012). However, using our nuclear localized *gfap:nls-mCherry* line coupled with anti-Gfap labeling, we can overcome these challenges and determine whether radial glia co-express Sox2 over time. To do this, cryosectioned *tg(gfap:nls-mCherry)* embryos were labeled for anti-Sox2 and anti-Gfap to delineate radial glial morphology at time points spanning embryonic neurogenesis.

Initial examination of Sox2 expression alone over a time course ranging between 24- to 72hpf showed Sox2+ nuclei present along the luminal surface at all time points

(Figure 3.3D,E,F). These Sox2+ nuclei became progressively restricted to the ventricular zone over time in accordance with the natural regression of the lumen into the central canal as previously described (Figure 3.3D,E,F) (Hudish et al., 2013). Between 24 and 48hpf there was no difference in the total number of Sox2+ nuclei (24hpf avg. = 51.57±2.4; 48hpf avg. = 55.67±1.02; p=0.121), however the total number of Sox2+ cells significantly decreased by 72hpf (avg. = 36.07±1.13; p<0.0001) (Figure 3.3G). When coupled for expression with the *gfap:nls-mCherry* transgene, quantitative analysis revealed that approximately 90% of Sox2+ nuclei were also nls-mCherry+ at 24hpf (avg. = 46.47±2.16; n=1394/1547 nuclei), which remained constant at 48hpf (avg. = 51.07±1.01; n=1532/1670 nuclei; p=0.06) (Figure 3.3H). By 72hpf the amount of Sox2+ nuclei colabeled with nls-mCherry slightly declined to 85% of the total Sox2 population (avg. = 30.63±1.12; n=919/1082 nuclei; p<0.0001) (Figure 3.3H). The resultant 10-15% fraction of Sox2+ nuclei absent for nls-mCherry labeling lacked radial glial morphology, and were predominantly found clustered together in the ventral portion of the spinal cord (dorsally opposed to the lateral floorplate cells) or sparsely distributed more dorsally in the neural tube (Figure 3.3D'-F",H grey portion of graph). To assess whether these Sox2+ cells are actively proliferating, we conducted a BrdU chase experiment from 24hpf to 48hpf and 48hpf to 72hpf. We discovered that both *gfap* positive and negative populations of Sox2 expressing cells were actively cycling during both time periods, albeit at different rates (Figure 3.3I,J). Quantitative analysis revealed that 64% of the Sox2/nls-mCherry double positive population incorporated BrdU between 24 and 48hpf, while only 33% of the Sox2+/nls-mCherry negative population was BrdU+ during that time (Figure 3.3J). Between 48 to 72hpf, however, this rate of BrdU incorporation had

dramatically decreased in both populations (Sox2+/nls-mCherry+ = 4%; Sox2+/mCherry neg. = 2%; $p<0.0001$), coincident with the cessation of embryonic neurogenesis. These results suggest that nearly all cells that constitute the embryonic neural stem cell population are represented by the co-expression of *gfap, nestin* and Sox2, with the exception of a subset population of cycling Sox2+*, gfap* negative progenitor cells in the ventral spinal cord.

3.3.4 Radial glial-derived lineages are confirmed through fate mapping.

We next sought to determine which cell populations were derived from radial glia through retention of nuclear mCherry fluorescence. Due to the known long-term stability of the mCherry protein in zebrafish (more than 24h (Boniface et al., 2009, Moro et al., 2012), we reasoned that any cell type derived from a radial glial division should show perdurance of mCherry fluorescence in *gfap:nls-mCherry* embryos. Labeling with anti-ISL, which marks both sensory and motorneuron populations (Appel et al, 1995; Song et al., 2004; Hutchinson and Eisen, 2006), revealed that 64% of motorneurons were mCherry+ (MN n=62/97 cells), while sensory neurons (RB) were completely absent for mCherry labeling at 30hpf (RB n=0/26 cells) (Figure 3.4A,C). To distinguish whether mCherry inheritance was retained in distinct motorneuron populations, we crossed the *gfap:nls-mCherry* line with either *mnx1:eGFP* to label primary motorneurons (Flanagan-Steet et al., 2005; Seredick et al., 2012) or *gata2:eGFP* for secondary motorneurons (Meng et al., 1997). Unfortunately since the *mnx1* transgene is also retained in secondary MNs and VeLD interneurons at time points proceeding primary MN generation (Seredick et al., 2012), primary MNs were identified by cellular morphology and position in the ventral spinal cord during early neural tube formation. While most *mnx1*+ primary MNs

were absent for retention of mCherry, we observed approximately 9% of *mnx1*+ neurons that were mCherry+ at 18hpf (n=5/53 cells), and this number declined 3.8% by 24hpf (n=44/1191 cells) (Figure 3.4C); however these cells did not appear to be primary MNs. By using the *gata*+ transgene, which reliably identifies secondary MNs and a small population of interneurons during late neurogenesis (Meng et al., 1997), we identified that 63% of *gata2*+ neurons coexpressed mCherry by 36hpf (n=283/450 cells) which increased to 73% by 48hpf (n=790/1080 cells; $p<0.0001$) (Figure 3.4B,C). Together, these experiments illustrate that secondary MNs, but not primary MNs, are generated by Gfap+ radial glia.

Previously, we identified an indirect link between Gfap+ radial glial progenitors and GABA+ CoSA interneurons, and suggested that other GABA+ interneuron populations were generated by non-radial glial progenitors (Johnson et al., 2014). Therefore, we hypothesized that only CoSA interneurons would retain nuclear mCherry in our fate-mapping assay. While labeling for anti-GABA revealed that 67% of CoSA interneurons retained mCherry labeling in their nuclei (C, n=76/114 cells), we also identified 23% of VeLD interneurons were mCherry+ as well (V, n=8/35 cells) (Figure 3.4D,E). Neither DoLA (D) nor KA (K) interneurons exhibited mCherry labeling at 30hpf (D n=0/12 cells; K n=0/38 cells) (Figure 3.4D,E). These data largely support our previous observations that later born neurons (CoSA interneurons and SMNs) are derived from Gfap+ radial glia, whereas earlier-born neurons (sensory neurons, PMNs, DoLA, and KA interneurons) are likely derived from neuroepithelial cells or other Gfap- progenitor populations. Unexpectedly, we also identified a small yet significant subset of VeLD interneurons (23%) with Gfap+ radial glial origins, suggesting this lineage

approach is a more direct and thorough analysis to understand the contributions of Gfap+ progenitors than our previous assay (Chapter 2).

Lastly, we crossed *gfap:nls-mCherry* with *olig2:eGFP* to discern whether radial glia were required during oligodendrocyte development. At the onset of *olig2* expression within the ventral spinal cord at 24hpf, 66% of ventral *olig2*+ cells retained mCherry expression in their nucleus (n=459/696 cells) (Figure 3.4F,H), which significantly increased to 93% by 48hpf (n=161/173 cells; $p<0.0001$) and 95% by 72hpf (n=154/161 cells; $p<0.0001$) (Figure 3.4G,H). Since progenitors residing in the ventral Olig2+ domain are largely responsible for generating oligodendrocyte progenitor cells (OPCs) and oligodendrocytes in the dorsal neural tube, we next assayed whether these cellular populations were positive for Gfap-derived mCherry. In the dorsal neural tube, 47% of migrating OPCs were positive for mCherry labeling at 48hpf (n=7/15 cells), which increased dramatically to 93% by 72hpf (n=14/15 cells) (Figure 3.4G asterisks,H). While these results largely support previous studies demonstrating a Gfap+ radial glial origin for oligodendroglia, it also illustrates the dynamic changes of Gfap expression within this population. Taken together, these data support that the *gfap:nls-mCherry* represents a robust label retention tool to identify individual Gfap+ progenitor cells and their derivatives throughout the duration of embryonic neurogenesis.

3.4 Discussion

In this study we have generated and characterized a novel reporter line to help define the direct involvement of Gfap+ radial glia in spinal cord development. By using nuclear localized mCherry under the regulation of *gfap*, we showed that individual

mCherry labeled radial glial cells are present at the lumen throughout neurogenesis while non-radial glial cells are closer to the pial surface of the neural tube. We defined that nearly all NSCs expressing *nestin* or Sox2 were also *gfap*+ radial glial cells, which provides strong support that radial glia act as the main NSC population during vertebrate development. Furthermore, we illustrated that the *gfap:nls-mCherry* line can be used as a short-term reporter for cells derived from *gfap*+ radial glial cell divisions, and through this type of fate mapping we conclude that *gfap*+ radial glia are the necessary parent population for later-born CoSA interneurons, secondary motorneurons, oligodendroglia, and a subpopulation of VeLD interneurons.

3.4.1 Dynamic changes in *gfap*+ radial glial location can be observed over time

Previously, changes in the dorsoventral expansion of the lumen to a small central canal was found to coincide with the loss of proliferative neural stem populations that, correlated with the cessation of embryonic neurogenesis (Hudish et al., 2013). While radial glia have been shown to retain neural stem/progenitor and proliferation markers in the zebrafish embryo (Jao et al., 2012; Kim H et al., 2008b), no study has correlated whether this regional change in spinal progenitors during spinal cord maturation affects radial glial cells present at the lumen. By labeling the *gfap:nls-mCherry* line for Gfap, we were able to identify individual *gfap*+ cells with radial morphology throughout neurogenesis, and always in close association with the lumen from initial ventricle formation in the early neural tube to its regression into the central canal (Figure 3.2).

In developing mouse embryos, radial glial identity has been confirmed molecularly through expression of other glial-specific markers (Hartfuss et al., 2001). A

similar line of investigation could be insightful for the study of radial glial in the zebrafish spinal cord; however, while mRNA expression for *vimentin* (Cerda et al., 1998; Thisse & Thisse, 2008), *blbp* (Kim H et al., 2008a), *slc1a3a/glast* (Thisse & Thisse, 2008), and *s100b* (Rauch et al., 2003) are expressed throughout the zebrafish embryo and adult brain (Goldschmidt et al., 2012; Schmidt et al., 2013), their expression within radial glial populations of the zebrafish embryo are unexplored. Fortunately, the *gfap:nls-mCherry* line faithfully recapitulates *gfap* expression (Figure 3.1D-F) and has enabled us to comprehensive characterize radial glial development throughout the zebrafish spinal cord.

3.4.2 *gfap*+ radial glia constitute the major NSC population in the zebrafish spinal cord

Neural stem cell populations in the vertebrate embryo are largely defined by the molecular markers Sox2, Nestin, and the retention of proliferation labels such as PCNA or BrdU (Noctor et al., 2002; Anthony et al., 2004; Pevny & Nicolis, 2010). *Nestin* mRNA was observed prior to neural tube closure in the mouse embryo and largely confined to columnar neuroepithelial cells, which became concentrated in pial-associated endfeet and fibers of neuroepithelial and radial glial cells (Dahlstrand et al., 1995; Hockfield & McKay 1985). While *nestin* mRNA is widely expressed throughout the developing zebrafish and required for the generation of neural tissues (Mahler & Driever, 2007; Chen et al., 2010), no work had previously illustrated *nestin*+ cell morphology or coexpression with Gfap in the developing zebrafish CNS. In this study, we offer the first view of *nestin* expression in a cellular context throughout the embryonic zebrafish spinal

cord, and correlate our findings with our reporter for *gfap*+ cells (Figure 3.3). Throughout all of the time points a majority of *nestin*+ cells coexpressed with *gfap*+ radial glial cells, supporting our observations with Sox2 labeling that a majority of these Gfap+ radial glia act as neural progenitors during neurogenesis (Figure 3.3). Importantly, a portion of *gfap+, nestin*+ cells absent for radial morphology were also observed in the dorsolateral spinal cord at a distance from the lumen (Figure 3.3C, arrowheads). As these locations are well characterized as regions containing postmitotic neurons when compared to radial glial localization (Briona & Dorsky, 2014; Bernardos & Raymond, 2006), it is likely that Nestin and Gfap label the same neural progenitor populations throughout neurogenesis, and generate cells that retain residual transgene expression from the two lines.

In the zebrafish early spinal cord, Sox2+ NSCs line the primitive lumen in the first two days of neural development, which is reduced over time as the lumen is restricted to the central canal (Hudish et al., 2013). By colabeling this population with *gfap:nls-mCherry*, we were able to define two distinct cycling populations of Sox2+ neural stem cells within the zebrafish spinal cord during embryonic neurogenesis: a *gfap*+ radial glial NSC population, and a small, distinctly *gfap*- NSC population in the ventral spinal cord Figure 3.3D'-F"). Between 24-48hpf nearly 90% of all Sox2+ NSC populations are also *gfap*+, and by 72hpf this percentage drops by 5% coinciding with the culmination of neurogenesis (Figure 3.3H). Importantly, while this modest decline is additionally reflected in the total Sox2 population (Figure 3.3G, asterisk), the number of Sox2+*, gfap*- NSCs remains constant throughout the time course. These results suggest that the overwhelming majority of NSC in the zebrafish spinal cord are *gfap*+ radial glia,

and as the need for embryonic cell type derivation reduces so does the proportion of radial glia to drive neurogenesis. Interestingly, the presence of a non-radial glial Sox2+ NSC in the ventral spinal cord as early as 24hpf (Figure 3.3D'-F") suggests maintenance of a unique stem cell population previously unstudied.

Previous studies defining Sox2+ neural progenitors in the zebrafish neural tube identified a similar population situated in a domain molecularly separate from the pMN domain, suggesting that this Sox2+ population is not required to generate oligodendrocyte progenitor cells (Jao et al., 2012). Additionally, this population did not colabel with Gfap+ fibers, further confirming that it was not a NSC population that had once expressed *gfap.* We hypothesize that this population may represent a unique population of Sox2 progenitors with limited proliferative capacity during spinal cord development, and may contribute to cellular populations present in the ventral nerve cord.

3.4.3 *gfap*+ divisions result in the generation of later-born interneurons, motorneurons and oligodendroglial populations

In zebrafish, little work has been conducted to understand what contributions radial glia may be making towards spinal cord neurogenesis. Previously, we and others illustrated that failure to maintain Gfap+ progenitor cells reduced both secondary motorneuron and oligodendrocyte populations from the pMN domain of the ventral spinal cord (Kim & Dorsky, 2011; Kim S et al., 2008) and a subpopulation of more dorsally localized CoSA interneurons (Johnson et al., 2014), however these studies cannot rule out the contributions made from other proliferative populations present in the spinal cord. Our fate mapping results using the *tg(gfap:nls-mCherry)* reporter line

corroborated, with greater confidence, the lineages we previously suggested to require radial glial cells for their derivation: CoSA interneurons, secondary motorneurons, oligodendrocyte progenitor cells and oligodendrocytes. The most notable difference was the unique identification of a small population of VeLD interneurons by fate mapping, which we previously reported to be unperturbed following radial glial mitotic arrest (Johnson et al., 2014). We reported only a 23% contribution to the total VeLD population (Figure 3.4D,E), which may have been too small of a difference for us to detect a statistically significant absence following radial glial loss. We hypothesize that this astroglial-dependent subset of VeLD interneurons is related to other radial glial derived pMN cells (motorneurons and oligodendroglia), as subsets of VeLD interneurons are known to express shared genes (*lim3, mnx*) with primary and secondary motorneurons located in the pMN domain (Appel et al., 1995, Park et al., 2004, Seredick et al., 2012).

3.5 Materials and Methods

3.5.1 Zebrafish

Adult zebrafish were maintained as described in Chapter 2 and Johnson et al., 2014. Additional fish lines used in this study were wild type (AB* and TU) (ZIRC and provided by Christian Lawrence, MGH), *tg(gfap:GFP^{mi2001})* (ZIRC), *tg(-3.9nestin:GFP)* (provided by Uwe Strahle), *tg(mnx1:eGFP)* (provided by Richard Dorsky), *tg(gata2:eGFP)* (provided by Shou Lin), and *tg(olig2:eGFP)* (provided by Bruce Appel). The routine care of zebrafish embryos involved incubation at 28°C and a 12h light-dark cycle ((Westerfield, 2007); Zebrafish International Resource Center, ZIRC).

3.5.2 Generation of *tg(gfap:nls-mCherry)*

Rosemarie Doris and Stephen Devoto, Department of Biology, Wesleyan University, Middletown, CT generated the-gfap:nls-mCherry construct. To take advantage of the efficiency of the Tol2 transposon and Gateway cloning technology (Kawakami, 2004), restriction/ligation and PCR was used to delete a short fragment of the original *gfap* promoter (Bernardos & Raymond, 2006) that included the ATG at bp8123. This edited version of the *gfap* promoter now comprises intron1-promoter-exon1, but lacks the endogenous ATG. This resulting *gfap* fragment was subcloned into the 5' p5E clone (*p5E-gfap)* of the gateway system. *p5E-gfap* was recombined with *pME-nlsmCherry* in order to build a construct for nuclear localized cherry expression driven by *gfap.* This construct was microinjected in wild type embryos at the one cell stage at a concentration of 50ng/µl in combination with *Tol2* transposase mRNA (Kawakami, 2004). One allele was retained, *tg(gfap:nlmCherry^{sc032}).* F4 progeny from incrossed F3 fish of this line was used in these studies.

3.5.3 BrdU treatments

For proliferation assays using the *gfap:nls-mCherry* line, embryos were incubated in 10mM 5'-bromo-2-deoxyuridine (BrdU, Sigma, catalog no: B9285) diluted in embryo medium on ice for 15 minutes, then incubated for the next 24h in embryo medium at 28.5C before fixing. All embryos were fixed for 2H in 4% formaldehyde and processed for immunofluorescence.

3.5.4 Immunofluorescence

Embryos were fixed in 4% formaldehyde in phosphate buffer for 2H at room temperature or overnight at 4°C. For interneuron and sensory neuron staining, embryos were fixed in a solution of 4% formaldehyde, 0.05% glutaraldehyde, 5mM EGTA, 5mM MgSO4, and 0.1% Triton-X in phosphate buffer (PB) for 1H room temperature (Dekens et al., 2003). Tissue sections were collected at a thickness of 0.14µm with a Leica cryostat. Whole mount or section immunofluorescence was conducted as previously described (Johnson et al., 2014). Primary antibodies used include rabbit anti-Gfap (1:500, Dako), mouse anti-Zrf1 (Gfap; 1:100, ZIRC), rabbit anti-Sox2 (1:500, Abcam), rabbit anti-GFP (1:300, Invitrogen), rat anti-BrdU (1:100, AbD Serotec), rabbit anti-GABA (1:1000, Sigma), and mouse anti-Islet-1 (39.4D5, 1:200, DSHB). Nuclei were visualized in sectioned tissue with Hoechst stain (1:30,000, Invitrogen).

3.5.5 Imaging

Images obtained to measure mCherry expression over time were conducted on live embryos using a Zeiss Lumar V12 stereomicroscope. Images on fixed tissue samples were obtained using an AxioImager Z1 equipped with Apotome (Zeiss), and Z-stacks were collected with an optical sectioning thickness of 0.53µm at 40X (for whole mount tissue) or 0.31µm at 63X (for sections), and processed using Zen software (Zeiss). For fate mapping, neuronal and glial populations were manually quantified for the retention of nuclear mCherry fluorescence, which was analyzed in single optical slices. Importantly, the exposure time and gain levels for the acquisition of mCherry fluorescence were maintained for all samples collected, and manipulation of intensity

levels was only used to eliminate background signal. Lateral acquisitions of neuronal and glial populations were identified and quantified as previously described (Johnson et al., 2014).

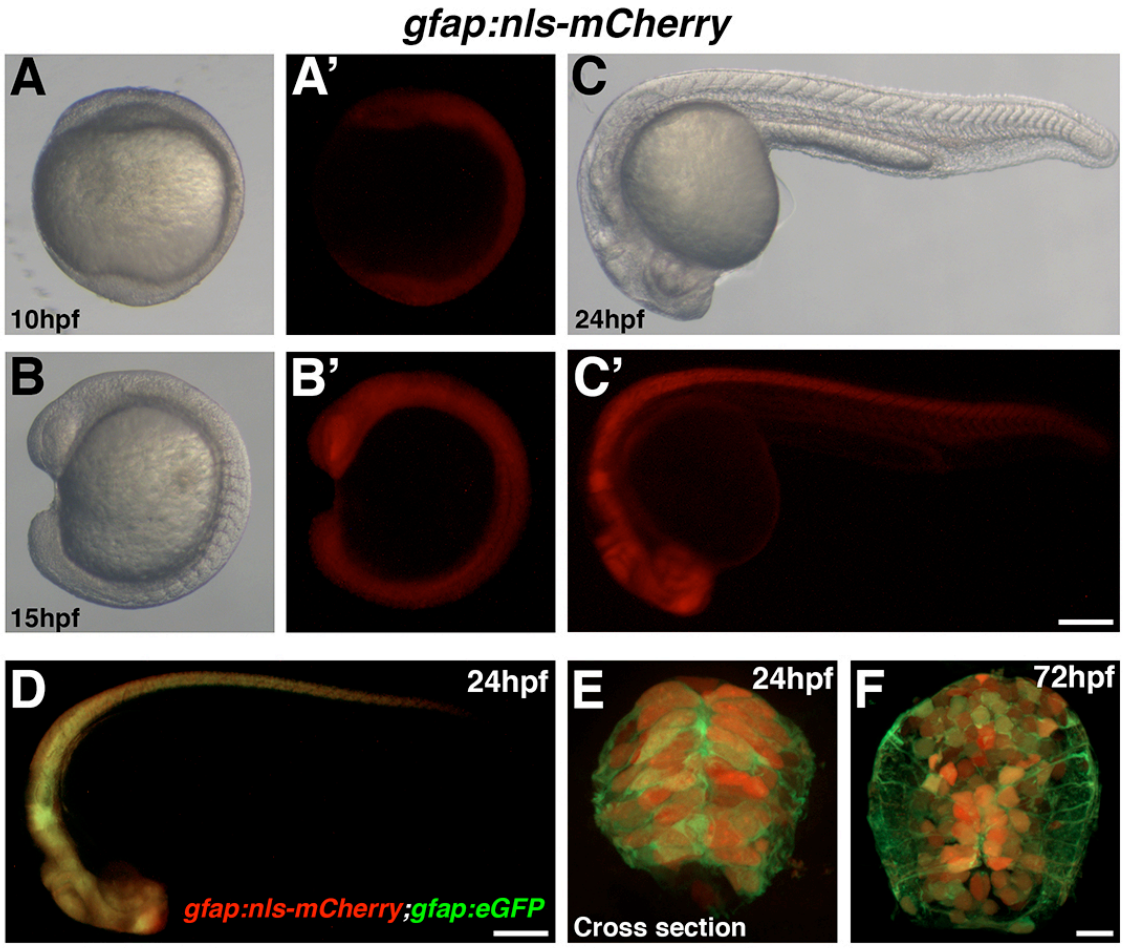

Figure 3.1. Transgene expression of the *gfap:nls-mCherry* line. Bright field and fluorescent images of *gfap:nls-mCherry* embryos at (A, A') 10h showing initial dim expression of nls-mCherry within neural tissues. (B' B') At 15hpf brighter nls-mCherry expression is seen in the forebrain, eye, and spinal cord, and (C, C') at 24hpf, nls-mCherry expression is restricted to neural tissues. Scale bar = 100μm. (D-F) Coexpression of *gfap:nls-mCherry* and *gfap:eGFP*^{mi2001} lines illustrate restriction of both transgenes to neural tissues throughout the embryo (D) and within radial glial cells at (E) 24hpf and (F) throughout embryonic neurogenesis. Scale bar = 10μm.

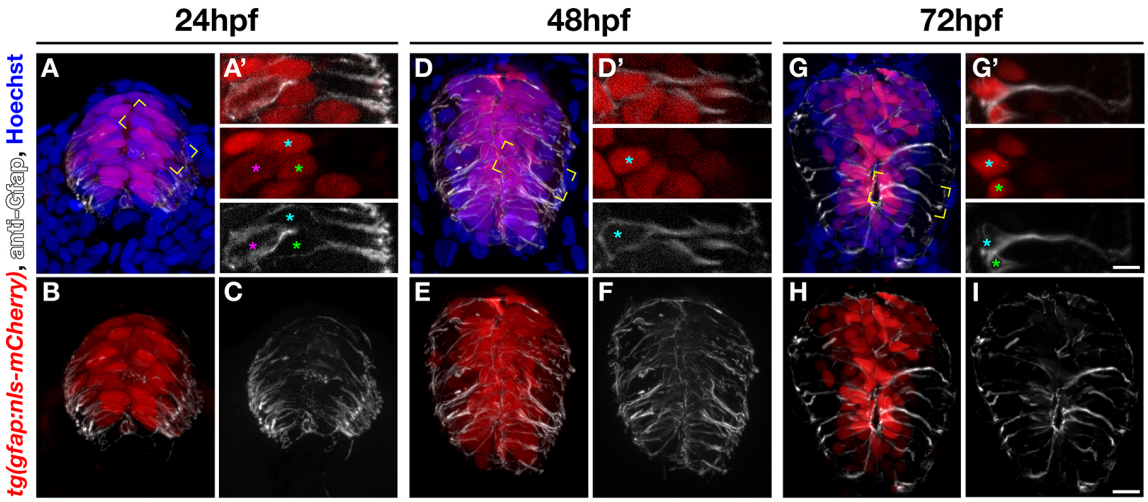

Figure 3.2. The *gfap:nls-mCherry* transgene labels individual nuclei in cells with radial glial morphology. (A-I) Maximum intensity projections showing cross sections of 24hpf, 48hpf, and 72hpf *gfap:nls-mCherry* embryos, immunolabeled with anti-Gfap (white) and Hoechst nuclear dye (blue) to visualize radial glial populations. (A', D', G') Single optical slices showing magnified views of individual cells from subregions of MIPs in A,D,G marked by yellow box. (A-C) Cross section of 24hpf embryo showing dispersed presence of nls-mCherry and Gfap coexpressing cells throughout the neural tube, many of which retain Gfap+ radial fibers clearly seen in B, C. (A') Magnified view of select cells in A showing individual nls-mCherry+ nuclei surrounded by anti-Gfap, indicating radial glial morphology (colored asterisks match nucleus with radial body). (D-F) Cross section of 48hpf embryo showing nls-mCherry and Gfap coexpressing cells, accumulated medially along the lumen. (D') Magnified view of select cells in D, showing typical radial glia morphology including bright pial fibers. (G-I) Cross section of 72hpf embryo showing restricted occurrence of nls-mCherry and Gfap coexpressing cells adjacent to the central canal. Note that many cells in the dorsal neural tube express nls-mCherry but are absent for radial fibers. (G') Magnified view of select nls-mCherry and Gfap coexpressing cells in G, adjacent to the central canal showing typical morphology of radial glia. Scale bar in G = 5μm; scale bar in I = 10μm.

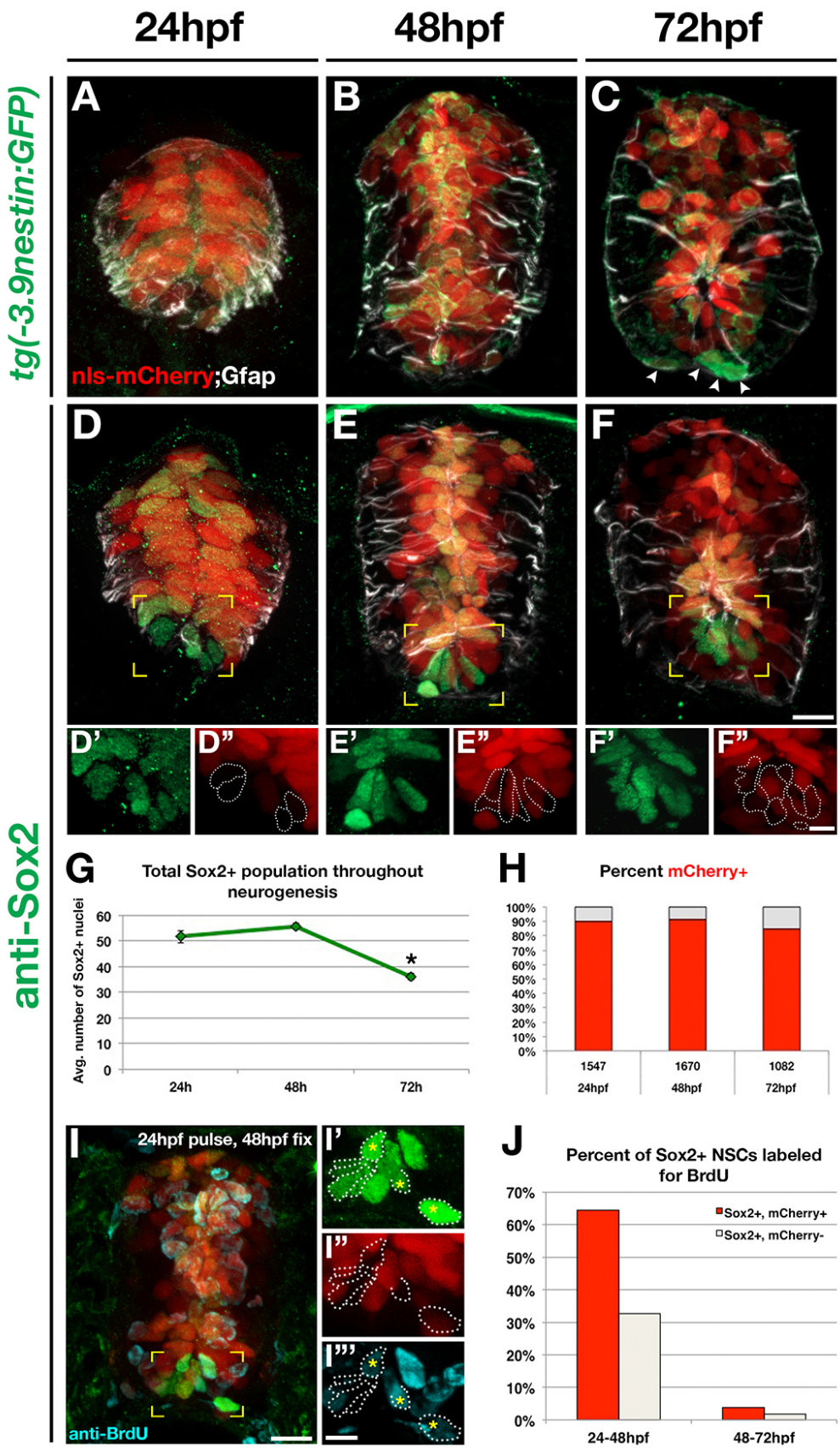
24hpf
48hpf
72hpf
tg(-3.9nestin:GFP)
anti-Sox2
A
B
C
nls-mCherry;Gfap
D
E
F
D'
D"
E'
E"
F'
F"
G
Total Sox2+ population throughout neurogenesis
Avg. number of Sox2+ nuclei
60
50
40
30
20
10
0
24h
48h
72h
*
H
Percent mCherry+
100%
90%
80%
70%
60%
50%
40%
30%
20%
10%
0%
1547
24hpf
1670
48hpf
1082
72hpf
I
24hpf pulse, 48hpf fix
anti-BrdU
I'
I"
I'"
J
Percent of Sox2+ NSCs labeled for BrdU
70%
60%
50%
40%
30%
20%
10%
0%
Sox2+, mCherry+
Sox2+, mCherry-
24-48hpf
48-72hpf

Figure 3.3. *gfap*+ radial glia coexpress neural progenitor markers. (A-C) Cross sections of 24hpf, 48hpf, and 72hpf double transgenic *gfap:nls-mCherry;-3.9nestin:GFP* embryos labeled with anti-Gfap to visualize *nestin+, gfap+* radial glial populations. All sections were immunolabeled with anti-GFP to enhance the signal of the *-3.9nestin:gfp* transgene. (A) Cross section of a 24h embryo showing cells coexpressing nls-mCherry and GFP, many of which retain Gfap+ radial fibers. (B) Cross section of a 48h embryo showing luminal accumulation of cells coexpressing nls-mCherry and GFP displaying typical radial glia morphology. Both transgenes also label cells closer to the lumen along the dorsolateral region of the neural tube that are not associated with glial fibers. (C) Cross section of a 72h embryo showing cells coexpressing nls-mCherry GFP with radial glial morphology restricted around the central canal. Double positive non-glial cells are located ventral to the central canal and show bright expression of *-3.9nestin:GFP* and dim expression of *gfap:nls-mCherry* transgenes (arrowheads). (D-F) Cross sections of 24hpf, 48hpf, and 72hpf *gfap:nls-mCherry* embryos immunolabeled with anti-Sox2 (green) and anti-Gfap (white) to visualize contributions of radial glia to the pan-NSC population. (D) Cross section of 24hpf embryo showing nearly all Sox2+ nuclei were present along the lumen and coexpressed nls-mCherry and Gfap in radial fibers. (E) Cross section of a 48hpf embryo showing that Sox2+/nls-mCherry+ nuclei concentrated at the lumen are present in cells with radial glial morphology. (F) Cross section of 72hpf embryos showing that Sox2+/nls-mCherry+ nuclei are mostly concentrated around the central canal and display radial glial morphology. At all time points, a population of Sox2+/nls-mCherry negative cells can be seen in the ventral neural tube in the yellow boxed area of panels D- F. Scale bar = 10μm. (D'-E") Enlarged views of yellow-boxed areas comparing ventral Sox2+ nuclei in panels D', E', F' with ventral nls-mCherry+ nuclei in panels D", E", F". Sox2+, mCherry negative nuclei were outlined for clarity. Scale bar = 5μm (G) Quantification of the total number of Sox2+ cells present at all time points. No change in the total number of Sox2+ is observed between 24hpf and 48hpf, however there is a modest yet significant decline at 72hpf ($p<0.0001$). (H) Quantification of the percentage of total Sox2+ nuclei that are nls-mCherry+ (red) throughout neural development. Nls-mCherry negative cells are depicted in grey, and the numbers above each population represent the total number of cells assayed per time point. (I) Cross section of a *gfap:nls-mCherry* embryo treated with BrdU at 24hpf, fixed at 48hpf, and labeled for anti-Sox2 (green) and anti-BrdU (cyan). Scale bar = 10μm. (I'-I''') Enlarged view of yellow-boxed area in panel I, with ventral Sox2+, nls-mCherry negative cells outlined for clarity. Asterisks denote ventral Sox2+/ nls-mCherry- cells that are BrdU+. Scale bar = 5μm. (J) Quantification of the percentage of Sox2+ populations positive for BrdU at all time points. Sox2+/nls-mCherry+ cells are shown in red, and Sox2+/nls-mCherry negative cells are depicted in grey.

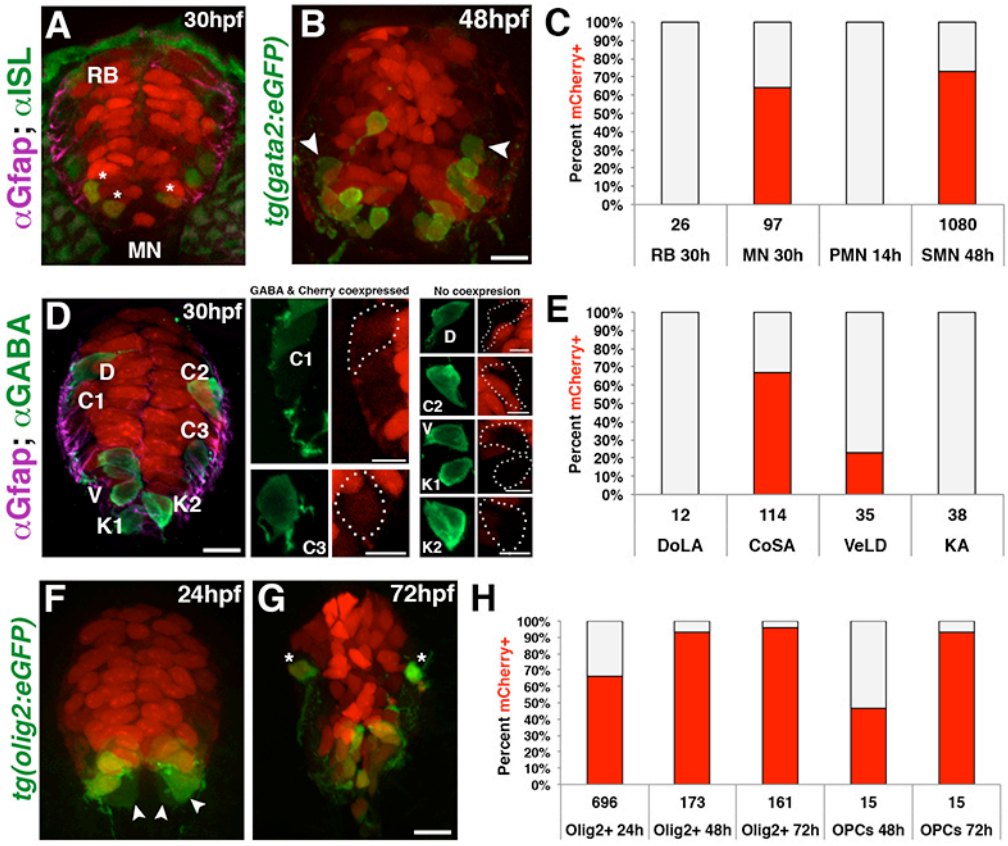

Figure 3.4. Fate mapping reveals radial glia are the parent population for distinct populations in the spinal cord. (A) Cross section of a 30hpf *gfap:nls-mCherry* embryo immunolabeled with anti-Islet-1 (ISL), showing nls-mCherry is absent in RB sensory neurons but present in a subpopulation of MNs (asterisks). (B) Cross section of a 48hpf *gfap:nls-mCherry;gata2:eGFP* embryo showing secondary motorneurons (SMN) expressing GFP. Nearly all Gata2+ SMN were nls-mCherry+, with few cells absent for nls-mCherry (arrowheads). Scale bar = 10μm. (C) Quantification for the percentage of sensory (RB), total ISL+ MNs, primary motorneurons (PMN) and secondary motorneurons (SMN) retaining nls-mCherry+ nuclei (red). (D) Cross section of a 30hpf *gfap:nls-mCherry* embryo immunolabeled with anti-GABA to identify DoLA (D), CoSA (C), VeLD (V) and KA (K) interneurons. Subset Z-stacks and maximum intensity projections were generated for each neuronal population for clarity. Scale bar = 10μm. (E) Quantification of the percentage of each interneuron population expressing nls-mCherry+ nuclei (red) at 30hpf. (F, G) Cross sections of 24hpf and 72hpf double transgenic *gfap:nls-mcherry;olig2:eGFP* embryos showing Olig2+ populations. (F) Cross section of a 24hpf embryo showing that a majority of Olig2+ cells express nls-mCherry with the exception of the ventral most Olig2+ population that do not express nls-mCherry (arrowheads). (G) Cross section of a 72h embryo showing nls-mCherry transgene expression is found throughout the ventral Olig2+ population as well as dorsal OPCs (asterisks). Scale bar = 10μm. (H) Quantification of the percentage of ventral Olig2+ cells along with dorsal migrating OPCs that retain nls-mCherry+ nuclei (red)

throughout oligodendroglial development. In all graphs, nls-mCherry negative cells are depicted in grey, and the numbers below each population represent the total number of cells assayed.

CHAPTER 4

GFAP-POSITIVE RADIAL GLIA ARE ESSENTIAL FOR LATE NEUROGENESIS, AXON PATTERNING, AND PROPER LOCOMOTION

Sections contained within this chapter are adapted from the original research article *in submission*: Johnson K, Bashiruddin S, Barragan J, Smith CJ, Tyrrell C, Parsons MJ, Doris R, Kucenas S, Downes GB, Velez C, Sakai C, Pathak N, Anderson K, Stein R, Devoto SH, Mumm JS, Barresi MJF (2015) Gfap-positive radial glial cells are an essential progenitor population for later born neurons and glia in the zebrafish spinal cord. *Glia*.

4.1 Introduction

In development, formation of the nervous system relies on the coordinated actions between proliferation, patterning and maintenance of neural tissues. During vertebrate neurulation, neuroepithelial cells are specified from neural ectoderm tissue and initiate neurogenesis. Later in development, neuroepithelial cells directly transform into radial glia, which then act as a major neural stem cell population before switching to a predominantly gliogenic role in later development of the vertebrate CNS (Malatesta et al., 2000; Noctor et al., 2001; Kim et al., 2008; reviewed in Kriegstein & Alvarez-Buylla, 2009). Following neurogenesis, radial glia act as a scaffold for supporting migrating neurons to generate the cortical layers, acting as a permissive substrate to promoting early forebrain commissure formation, or by spatially segregating axon tracts in the embryonic spinal cord (Marcus & Easter 1995; Barresi et al 2005; Barry et al., 2013). These programs can be upregulated in the larval and adult zebrafish following injury, where radial glia have been shown to proliferate and form scaffolds to promote axonal regeneration and neurogenesis in the brain and spinal cord (Briona & Dorsky 2014, Goldshmit et al 2012, Kroehne et al., 2011). Lastly, radial glia maintain neuronal health and homeostasis by regulating formation and function of the blood brain barrier (BBB).

Embryonic radial glia directly contact and provide tracts to guide angiogenic sprouts to help form the BBB (Gerhardt et al., 2004; Noctor et al., 2001) and regulate vascular proliferation, angiogenesis, and functional integrity throughout development into adulthood (McCarty et al., 2004; reviewed in Alvarez, 2013). Disruptions in these radial glial-vascular connections during neurogenesis were shown to lead to hemorrhagic lesions throughout the embryonic brain and spinal cord, motor defects, axonal deterioration in the brain and spinal cord, ataxia and death (McCarty et al., 2004), illustrating the importance of functional boundary formation by radial glia.

Surprisingly while these roles are generally supported, little work has been conducted to directly test the requirement of radial glia for these processes during embryonic development. Several studies have attempted to eliminate astroglial cells to elucidate their roles in forebrain neurogenesis or corticospinal tract formation (Pippenger et al., 1990, Delaney et al., 1996, Khurgel et al., 1996, Cui et al., 2001, Morshead et al., 2003), however, these approaches were limited in dosage, spatial restrictions, and/or only targeted small subsets of astrocytes. Recently, a new study in zebrafish utilizing a *gfap:*Gal4/UAS:Nitroreductase system was able to induce radial glial cell death in the adult zebrafish brain (Shimizu et.al., 2015). While this system was restricted to the telencephalon and the focus of the study on adult neurogenesis, it nonetheless described a novel avenue to ablate the radial glial population in a zebrafish model system.

To directly assay the contributions and functions of radial glia during embryonic neural development, we have utilized the inducible nitroreductase/Metronidazole (Mtz) system to generate two genetic ablation lines that drive expression of the bacterial nitroreductase *nfsB* gene under regulation of the zebrafish Gfap promoter. Here, we show

that following application of Mtz, robust ablation of radial glial cells is apparent throughout CNS tissues during late embryonic neurogenesis, with the highest defects observed in spinal cord. We show that microglial populations are actively recruited to the spinal cord by 3dpf, and propose an involvement in debris clearance independent of the macrophage population. In addition, ablation of spinal cord radial glia also lead to disruptions in lateral axon tract organization, and loss of motor coordination following touch-mediate escape response assays. We also observed reductions in CoSA interneurons, secondary motorneurons, and oligodendroglial lineages following astroglial ablation, supporting our previous findings. Together, this study largely corroborates our previous findings and more precisely delineates a role for radial glia in neuronal and glial development, axon organization, and locomotor output during zebrafish spinal cord development.

4.2 Experimental Strategy

In order to test the requirement of radial glia for proper neurogenesis, we generated an inducible and astroglial specific ablation system. The *tg(gfap:nfsb-mCherry)* transgenic line uses the regulatory elements of the zebrafish *gfap* gene (Chapter 3) to drive expression of the *E.coli* nitroreductase gene *nfsb* fused with mCherry within Gfap+ radial glia (Figure 4.1A). Upon application of the prodrug Metronidazole (Mtz), the nitroreductase enzyme (NTR) encoded by the *nfsb* gene will convert Mtz into cytotoxic metabolites to eventually induce cell death specifically in Gfap+ radial glia without perturbing surrounding populations. Using this approach, we are able to specifically

ablate Gfap+ radial glia both spatially and temporally throughout the nervous system to discern how this population is required throughout CNS development.

4.3 Results

4.3.1 Transgene recapitulates radial glial development and morphology in the developing spinal cord

To directly test the requirement of astroglia for CNS development, we took a similar approach as Shimizu et al and utilized the nitroreductase (NTR) system to chemically ablate radial glial cells by inducing cell death in a temporally controlled manner during embryogenesis (Shimizu et al., 2015, Curado et al., 2007, Pisharath et al., 2007, Curado et al., 2008). In contrast to the previously used Gal4/UAS driver, we engineered the 7.4kb zebrafish *gfap* promoter (5'UTR, Exon1 and Intron1 (Bernardos and Raymond, 2006)) to directly drive expression of the *E.coli nfsB* gene fused with mCherry (Figure 4.1A). By employing this system, the *nfsB* gene will encode for the NTR enzyme, which will convert the prodrug Metronidazole (Mtz) into a cytotoxin specifically within Gfap+ radial glial cells. We generated two stable lines *tg(gfap:nfsb-mCherry)*^{sc059} and *tg(gfap:nfsb-mCherry)*^{sc0129} (Figure 4.1B-I') that were used throughout the study. NTR-mCherry expression within the *nfsb*^{059} allele was first detected at 10 hours post fertilization (hpf) (Figure 4.1B-E; similar to the *gfap:eGFP*^{mi2001} line) while NTR-mCherry detection in the *nfsb*^{129} allele was first observed two hours earlier (Figure 4.1F-I). Expression in both lines was restricted to the developing CNS, where the intensity of NTR-mCherry expression increased over time (Figure 4.1B-I). To confirm

faithful reproduction of *gfap* expression, we crossed respective alleles with *tg(gfap:eGFP^{mi2001})* and full colocalization of NTR-mCherry and GFP protein was observed within the spinal cord at 24hpf that persisted in adult tissues (Figure 4.1J-L; adult expression for *nfsb^{129}* not shown).

4.3.2 Metronidazole induces apoptosis in NTR expressing radial glia by late embryogenesis that is cleared by microglia

To determine whether Mtz treatment of these *tg(gfap:nfsb-mCherry)* lines could induce radial glial cell ablation, we treated *tg(gfap:nfsb-mCherry)* embryos at 8hpf (corresponding with onset of their expression) with 10mM Mtz or 0.2% DMSO as the vehicle control until 24, 48 and 72 hpf. No change in overall gross morphology was seen at 24hpf (Figure 4.2A,D); however, dorsal curving of the trunk was observed in embryos treated with Mtz from 8-48hpf and 8-72hpf (Figure 4.2B-F). Significant brain hemorrhaging was observed particularly around the ventricles in 29% of 8-48hpf Mtz treated embryos and 48% of embryos treated with Mtz from 8-72hpf (Figure 4.2B,E,C,F). The timing of these morphological changes correlated with visible changes in NTR-mCherry expression. Uniform NTR-mCherry labeling was observed in both 24hpf groups, with expression being more prominent in the anterior spinal cord (somite 11) as compared to the more posterior regions (somite 26) (Supplemental Figure 4.1A,D; insets). At 48 and 72hpf, NTR-mCherry expression remained robust throughout the CNS of control treated embryos. In contrast, NTR-mCherry+ expression in Mtz-treated embryos was reduced and appeared fragmented at 48hpf as compared to controls (Supplemental Figure 4.1B,E, insets). This pattern in NTR-mCherry expression was more

severe at 72hpf (Supplemental Figure 4.1C,F). Interestingly, at 72h dense NTR-mCherry+ clusters were more prevalent in dorsal regions of the spinal cord and absent from more ventral regions (Supplemental Figure 4.1F, insets). Both alleles, *gfap:nfsb-mCherry*^{sc059} and *gfap:nfsb-mCherry*^{sc129} demonstrated similar gross morphology and NTR-mCherry expression (*nfsb*^{sc059} shown in Figure 2, *nfsb*^{129} not shown).

The fragmented appearance of NTR-mCherry expression in Mtz treated *tg(gfap:nfsb-mCherry)* embryos resembled the membrane blebbing behaviors characteristic of cells undergoing apoptosis (Kerr et al., 1972, Brill et al., 1999, Huppertz et al., 1999, Charras, 2008, Charras et al., 2008). To determine whether apoptotic cell death was being induced in NTR-mCherry+ cells, we immunolabeled with the apoptotic marker anti-activated Caspase-3 following treatment with Mtz or vehicle control in both *gfap:nfsb-mCherry*^{sc059} and *gfap:nfsb-mCherry*^{sc129} embryos. In addition, we attempted to identify when changes in NTR-mCherry and Caspase-3 labeling began by visualizing treated embryos in 6h intervals from 24hpf to 60hpf (Figure 4.2G). To ensure our 10mM Mtz treatment was not causing any neurotoxic effects, we similarly treated *tg(gfap:eGFP*^{mi2001}*)* embryos and assayed for changes in the amount of programmed cell death over time (Figure 4.2H). Little to no cell death was evident in our vehicle control or *tg(gfap:eGFP)* control lines throughout the time course (Figure 4.2G upper row, H, data not shown). In contrast, significant anti-activated Caspase-3 labeling was seen in *tg(gfap:nfsb-mCherry*^{sc129}*)* embryos as early as 36hpf, which colocalized with fragmented NTR-mCherry expression (Figure 4.2G, lower row). The NTR-mCherry+ clusters consistently observed in the more dorsal region of the spinal cord also co-expressed anti-activated Caspase-3 labeling (Figure 4.2G, t54, t60, arrowheads). Distinctively, Mtz-

treatment of embryos with the *gfap:nfsb-mCherry*^{sc059} allele did not show signs of anti-activated Caspase-3 labeling until 42hpf (data not shown), which may be reflective of the 2 hour difference in the timing of initial NTR-mCherry expression between the two lines (Figure 4.1). Importantly, the dynamic changes in NTR-mCherry fragmentation and accumulation in the dorsal spinal cord were observed in both alleles (*nfsb*^{059} not shown), suggesting that although the onset of cell death is slightly different, both induce a similar pattern of robust radial glial ablation over the course of neurogenesis.

To further characterize the process of cell death upon Mtz treatment in live embryos, we utilized an Annexin-V reporter construct to mark apoptotic cells in the live embryo (van Ham et al., 2010). To visualize Annexin-V, *TBP-GVP;UAS-SecA5-YFP* constructs were microinjected at the one cell stage into *gfap:nfsb-mcherry*^{sc129} embryos, which established a mosaic pattern of Annexin-V-YFP expression. The *UAS/Gal4* system drives expression of secreted Annexin-V-YFP, which decorates the membrane of dying cells with YFP (van Ham et al., 2010). Injected embryos were treated with either the vehicle control or Mtz from 8hpf to 38hpf. No change in YFP-labeling was observed between treatment groups at 28hpf (Figure 4.2I,K). However, in the following 10 hours, YFP-labeling significantly increased throughout the neural tube in Mtz-treated embryos as compared to control embryos (Figure 4.2J,L). In addition, we identified several examples of NTR-mCherry+ cells with radial glial morphology that showed progressive co-localization of Annexin-V-YFP. In these examples, fragmentation of NTR-mCherry preceded YFP labeling, and co-expressing cells were further broken into smaller pieces that disappeared in approximately 72 minutes (Figure 4.2M). Our results taken together suggest that *gfap* driven expression of NTR is effective at inducing apoptotic cell death in

radial glia of Mtz treated embryos as early as 36hpf. *gfap* expression is known to progressively increase over the course of primary neurogenesis, which is similar to the gradual increase in mCherry fluorescence seen in our transgenic lines (Figure 4.1; (Bernardos and Raymond, 2006)). Therefore, the delay in visible radial glial cell death until 36hpf might be due to the time lag associated with elevated *gfap* expression necessary to build up enough functional NTR activity to cause programmed cell death.

Due to the absence in mCherry+ fragments throughout the spinal cord over time, we hypothesized that a clearance mechanism must be activated in the embryo as a response to ablation. In injury models within the adult zebrafish CNS, immune cells were observed infiltrating into the nervous system to the site of the lesion, and actively cleared debris products (van Hamm et al., 2014). In collaboration with Dr. Cody Smith and Dr. Sarah Kucenas, University of Virginia, we assayed whether a similar response was occurring in our treated embryos to cause a reduction in mCherry expression. To observe if a similar process was occurring following ablation, *gfap:nfsb-mCherry*^{sc059} embryos were crossed with *pu1:GFP* to label for microglial and macrophage populations. Following treatment of *gfap:nfsb-mcherry;pu1:GFP* embryos, macrophages were consistently found on the periphery of control and ablated spinal cords by 72hpf (Figure 4.3A-B', arrows). In contrast, GFP+ microglial cells were first present within the spinal cords of Mtz-treated embryos at 72hpf and several coexpressed mCherry fragments (Figure 4.3B-B", arrowheads,G), suggesting an involvement with debris clearance. To confirm macrophages were not involved in spinal cord infiltration and clearance, *gfap:nfsb-mCherry*^{sc059} was also crossed with *mpeg:GFP,* which specifically labels for macrophages. Following ablation, no macrophages were seen within the spinal cord by

72hpf, indicating they have no involvement in the immunological response following astroglial ablation (Figure 4.3C-D",G). We next tested whether microglia are the main source of ablation-associated debris clearance by using a *spi1b* morpholino to specifically knock out microglial precursors. In uninjected Mtz-treated animals, mCherry fragments were still present throughout the spinal cord by 72hpf (Figure 4.3E-E"). In contrast, *spi1b* injected embryos had higher levels of fragmented mCherry expression, indicating that microglia are required for ablation-associated clearance (Figure 4.3F-F",H). However, we did observe several regions of cleared mCherry expression, indicating that some other unknown mechanism is eliminating debris from injured spinal cords independently of the immune system.

4.3.3 Two novel proliferative responses revealed in response to radial glial ablation

If radial glial cells serve as a major neural stem cell population during development as we and others have proposed, then their targeted ablation should cause a reduction in the presence of neural stem markers and proliferation throughout the spinal cord. To answer this, we again assayed the expression of the neural stem cell markers *nestin* and Sox2 following radial glial ablation. Changes in *nestin* expression were observed by crossing *tg(gfap:nfsb-mCherry)*^{sc059} with *tg(-3.9nestin:GFP),* and double-expressing embryos were treated with either vehicle control or Mtz. Consistent with our previous observations (Chapter 3), coexpression of the *nestin:GFP* and *gfap:nfsB-mCherry* transgenes were observed in the same cellular populations at all time points (Figure 4.4A-F). At 24hpf, preceding our expected onset of ablation, no visible changes in GFP or NTR-mCherry could be discerned between vehicle control and Mtz treated

embryos (Figure 4.4A,D). Between 48-72hpf, GFP continued to colocalize with NTR-mCherry within the spinal cords of vehicle control embryos, suggesting the two transgenes were consistently labeling the same spinal populations Figure 4.4B,C). Following induction of apoptosis at 48hpf, however, GFP+ fragments could be seen consistently coexpressed with blebbing NTR-mCherry+ debris (Figure 4.4E). By 72hpf, nearly all GFP+ cells observed in the spinal cord co-labeled with NTR-mCherry+ debris in Mtz-treated embryos, suggesting near complete loss of the *nestin*+ population (Figure 4.4F). Interestingly, we did observe consistent labeling of the *nestin:GFP* transgene in a small portion of ventral-localized cells in both control and Mtz-treated samples (Figure 4.4C,F arrowheads). This was a *nestin:GFP*+ cell population that we previously noted to be derived from *gfap*+ radial glia, albeit based on relatively dim level of *gfap:nls-mCherry* expression (Figure 3.3). We speculate that the survival of this *nestin:GFP*+ population may be due to the combined circumstances of particularly low NTR expression with the timeline of cell death induction(~40h) in our system as opposed to a novel subtype of *gfap* negative*/nestin* positive progenitors.

To further confirm that radial glial ablation reduces the spinal cord stem cell pool, control and Mtz-treated *gfap:nfsb-mCherry*^{sc059} embryos were labeled for the neural stem cell marker Sox2 and assayed throughout embryonic neurogenesis. Based on our previous observations that a majority of Sox2+ neural stem cells were *gfap*+ radial glial cells (Figure 3.3), we predicted that most Sox2+ cells would be lost following ablation with the exception of the small ventral subset of Sox2+, *gfap*-negative cells. Prior to any observable radial glial ablation at 24hpf, there was no significant difference in the number of Sox2+ cells present in the neural tube between control and Mtz-treated

embryos (p=0.908) (Figure 4.4G,J). In control embryos, the number of Sox2+ cells remained constant between 24hpf and 48hpf (p=0.435) until declining at 72hpf (p<0.0001) (Figure 4.4G-I) correlating with cessation of neurogenesis. After inducing ablation of *gfap*+ cells, there was a 17% reduction in the Sox2+ population at 48hpf as compared to control (Control avg. = 37.36±1.16, n=13; Mtz avg. = 31.2±1.58, n=13; p<0.0006) (Figure 4.4H,K), which continued to decline to 51% by 72hpf (Control avg. = 25.27±1.43, n=15; Mtz avg. = 12.27±0.93, n=15; p<0.0001) (Figure 4.4I,L). Importantly, we continued to observe the presence of Sox2+/NTR-mCherry negative cells dorsally opposed to the lateral floorplate cells following ablation (Figure 4.4K,L arrowheads), which is consistent with our previous description of this population (Figure 3.3D'-F").

Since ablation of *gfap*+ radial glia resulted in the loss of neural stem/progenitor markers, we next reasoned that there would be a deficit in cell proliferation in the developing spinal cord. To characterize cell proliferation over the course of radial glial ablation, control and ablated embryos were treated briefly with 10mM BrdU to label all cells in S-phase of the cell cycle at 24, 48, 72, and 96hpf. Prior to ablation, we saw no significant difference in the number of BrdU+ nuclei in the neural tube between vehicle control and Mtz-treated embryos at 24hpf (p<0.794) (Figure 4.5A,E,I). In vehicle control embryos, the number of BrdU+ nuclei within the neural tube decreased over time through 96hpf, again coinciding with the known culmination of embryonic neurogenesis by 72hpf (Figure 4.5A-D,I; (Mueller and Wullimann, 2003)). Following ablation, we quantified a statistically significant decrease in BrdU+ nuclei in Mtz-treated embryos at 48hpf as compared to vehicle controls (Control avg. = 5.07±0.35, n=19; Mtz avg. = 1.35±0.29, n=16; p<0.0001) (Figure 4.5B,F,I). Interestingly, at later time points, a small but

consistent number of BrdU+ nuclei persisted in the spinal cord of Mtz treated embryos at a level equivalent to vehicle controls (72hpf: Control avg. = 1.23±0.24, n=13, Mtz avg. = 1.4±0.21, n=14, p=0.590; 96hpf: Control avg. = 0.98±0.2, n=14, Mtz avg. = 1.5±0.23, n=14, p=0.093)) (Figure 4.5C,D,G,H,I). These results demonstrate that loss of Gfap+ radial glia leads to an immediate collapse in cell proliferation within the spinal cord, and while some proliferative cells persisted their dynamics were not altered relative to controls to compensate for the loss of Gfap+ radial glia.

We next considered whether the Sox2+/NTR-mCherry negative progenitor population we characterized was contributing to the remaining BrdU+ population present within the spinal cord (Figure 4.5K-N). When colabeled for anti-Sox2, we found no change in the total number of cycling Sox2+/NTR-mCherry nuclei between control and Mtz-treated embryos at 24hpf (Control avg. = 23.27±1.14; Mtz avg. = 26.2±1.85; p=0.189) (Figure 4.5M). Consistent with previous observations, the total proliferative Sox2+/NTR-mCherry population present in control treated embryos declined between 48 and 96hpf. At 48hpf, Mtz-treated embryos displayed a significant decline in the number of Sox2+/NTR-mCherry cells coexpressing BrdU (Control avg. = 2.6±0.41; Mtz avg. = 0.47±0.29; $p<0.001$) (Figure 4.5M), which was not recovered by 72hpf (Control avg. = 0.8±0.31; Mtz avg. = 0.4±0.24; p=0.314) and absent by 96hpf (Control avg. = 0.8±0.3; Mtz avg. = 0; $p<0.01$) (Figure 4.5K,L,M). This supports our previous observations where we found that *gfap*+ radial glia comprise the majority of the proliferative NSC population, and suggests that no other stem or progenitor population can compensate for loss of this population during embryonic neurogenesis. Interestingly, while no change in BrdU incorporation between control and Mtz-treated embryos was observed within the

Sox2+/NTR-mCherry negative fraction between 24 to 72hpf ($p>0.3$), we observed a modest yet significant increase in proliferative response in Sox2+/NTR-mCherry negative cells following ablation at 96hpf (Control avg. = 0.2±0.14; Mtz avg. = 0.93±0.32; $p<0.05$) (Figure 4.5K'-L",N), considerably after embryonic neurogenesis has completed. This late proliferative response is surprising, as no change in total BrdU incorporation is detected between control and Mtz-treated embryos at 96hpf ($p=0.093$), and suggests that this change may reveal a shift in stem cell potential in reaction to loss of the radial glial NSC population.

Following ablation, we consistently noticed an increase in the number of BrdU+ cells outside of the Gfap+ pial surface which is a barrier suggested to be established by radial glia (Figure 4.5A'-H' white asterisks) (McDermott et al., 2005, Lee and Song, 2013). These BrdU+ nuclei were characterized by an elongated morphology whose volume measured an average of 2 times larger than nuclei found within the spinal cord in control or Mtz-treated embryos (Supplemental Figure 4.2A-C). In control embryos, the number of BrdU+ elongated nuclei alongside the Gfap+ border of the spinal cord decreased over time by 96hpf. However at the onset of ablation there was a modest but significant increase in the number of elongated BrdU+ nuclei contacting the outer border of the spinal cord in Mtz-treated embryos at 48hpf as compared to vehicle control (Control avg. = 2.86±0.31, n=14; Mtz avg. = 4.36±0.14, n=11; $p<0.0001$), and this increase remained constant in Mtz-treated embryos throughout the duration of the experiment ($p>0.594$). Of particular importance, several of the elongated nuclei were seen straddling the border of the spinal cord (Figure 4.5F-H arrowheads, J; Supplemental Figure 4.2B,C), suggesting that these cells may have the ability to freely enter or exit the

spinal cord following loss of radial glia. When correlated with expression of Gfap, we found that while Gfap protein expression in control and Mtz treated embryos appeared normal at 24hpf (Figure 4.5A',E'), a complete loss of radial processes and decreased Gfap labeling along the pial surface was observed after 48hpf as compared to controls (Figure 4.5B'-D, F'-H'). Importantly the larger, elongated BrdU+ nuclei observed spanning the spinal cord boundary were typically found in locations correlating with reductions in anti-Gfap labeled radial glial fibers and end-feet (Figure 4.5F'-H' arrowheads, F' outlined example in Supplemental Figure 4.2C), suggesting that loss of Gfap+ radial glial cells and their structural end-feet eliminates a restrictive boundary that may permit the passage of proliferative, non-neural cells into the spinal cord.

4.3.4 *gfap*+ progenitors are required for late-born neuronal and glial populations

Previously, we showed that arresting trunk radial glial divisions had profound impact on the development of CoSA interneurons, secondary motorneurons, and oligodendroglia. This allowed us to build a model for spinal cord neurogenesis in zebrafish, however it was largely based on indirect observations. Using our two transgenic ablation lines, we next sought to directly test whether loss of radial glia prior to the birth of later-born neurons and glia had a profound impact on their development. To test whether radial glia are required for CoSA interneurons, *gfap:nfsb-mCherry*^{sc129} embryos were treated with vehicle control and Mtz, and labeled for interneurons with anti-GABA. Prior to ablation, we observed no change in the overall patterning of DoLA, CoSA, VeLD, or KA interneurons between vehicle control and treatment groups by 24hpf ($p>0.05$) (Figure 4.6C). During ablation, we observed a noticeable 21% reduction

in CoSA interneurons in Mtz-treated embryos at 36hpf (DMSO avg. = 31.9±0.95, n=10; Mtz avg. = 27.4±1.23, n=16; $p<0.02$), reducing further by 41% at 48hpf as compared to control (DMSO avg. = 36.36±1.65, n=14; Mtz avg. = 20.5±1.63, n=14; $p<0.0001$) (Figure 4.6A-C). This data largely supports our previous findings, where we reported a similar 42% reduction in CoSA interneurons following mitotic arrest of radial glia. Importantly, no significant changes in DoLA, VeLD, or KA interneuron populations between treatment groups at any age assayed ($p>0.05$). It should be noted that little to no change in the CoSA population was detected following ablation using the *nfsb*^{sc059} allele (data not shown), suggesting that either the CoSA lineage depends on radial glial derivation prior to 40hpf, or illustrates the requirement of CoSA interneurons for radial glia for their continued maintenance throughout development.

To determine if secondary motorneurons were impacted following radial glial ablation, we crossed *gfap:nfsb-mCherry*^{sc059} with *gata2:eGFP* line and visualized secondary motorneuron development over time (Meng et al., 1997). No change in the number of *gata2* expressing cells was detected between treatment groups at 36hpf ($p=0.878$) (Figure 4.6F), however, a 41% reduction in the number of *gata2*+ motorneurons was seen at 48hpf following radial glial ablation (DMSO avg. = 189.8±3.39, n=42; Mtz avg. = 112.3±6.9, n=31; $p<0.0001$) (Figure 4.6D-F). Despite extending the time course to account for any potential developmental delay, we did not observe a statistically significant difference in the number of *gata2*+ motorneurons present between 8-48hpf and 8-60hpf treatment groups ($p>0.83$) (Figure 4.6F).

Lastly, we induced radial glial ablation to test a direct requirement of radial glia for oligodendrocyte production. To do this, *gfap:nfsb-mcherry*^{sc059} was crossed with

tg(olig2:eGFP) to identify dorsal migrating oligodendrocyte progenitor cells (OPCs) and oligodendrocyte populations. A growing body of evidence widely supports a radial glial origin for a portion of the oligodendroglial lineage (Kim et al., 2008; reviewed in Kriegstein & Alvarez-Buylla 2009), therefore we predicted that induction of radial glial ablation would result in significant defects in OPCs and oligodendrocyte development. Prior to radial glial ablation, no significant change in the number of dorsal migrating OPCs was observed at 36hpf ($p>0.34$) (Figure 4.6I). By 48hpf, migratory OPCs were reduced by nearly 80% in Mtz-treated embryos as compared to control (DMSO avg. = 28.71±1.28, n=28; Mtz avg. = 6.33±1.1, n=33; $p<0.0001$) (Figure 4.6G-I), coinciding with astroglial ablation. By 72hpf, there was no change in the number of OPCs present in ablated embryos as compared to the 48hpf Mtz-treated group ($p>0.4$) (Figure 4.6I). Additionally, mature oligodendrocytes were not found within ablated spinal cords by the end of the time course, despite their presence in vehicle control embryos (not shown). Furthermore, GFP+ fragments were found throughout the spinal cord following radial glial ablation that colabed with mCherry+ debris, suggesting that a portion of *olig2* cells were generated by *gfap*+ radial glia and retained NTR-mCherry prior to induction of cell death. Here, the sum of these ablation studies provide direct evidence supporting our hypothesis that radial glia serve as a progenitor population for later-born neuronal and glial populations during spinal cord neurogenesis.

4.3.5 Loss of radial glia disrupts spinal cord axon organization and impairs locomotive behavior.

Our ablation system leads to the loss of radial glia, thereby providing the opportunity to assess the requirement of these cells in a variety of developmental events. If radial glia serve as critical support and guidance structures for pathfinding axons as pervious studies have suggested (Jacobs and Goodman, 1989, Marcus and Easter, 1995, Barresi et al., 2005), then radial glial ablation should lead to a disorganization of axonal patterning. To determine whether structural changes to axonal circuits occur following astroglial ablation, *gfap:nfsb-mCherry*^{sc059} embryos were treated and labeled for anti-Gfap and anti-acetylated tubulin (AT) to visualize axon morphology in the spinal cord. Prior to induction of radial glial ablation, no change in axon morphology was observed between control and treatment groups at 36hpf (Figure 4.7A,D), however, progressive disorganization of normal axonal patterns were clearly evident over time as compared to controls (Figure 4.7B-F). In Mtz treated embryos, longitudinally growing axonal tracts along the rostrocaudal axis of the spinal cord displayed small areas devoid of axons at 48hpf (Figure 4.9E, arrowheads), and by 72hpf these tracts had a severely defasciculated and disorganized morphology (Figure 4.7F). Computational rotation of the optical sections along the Y-axis provided a view of mCherry+ cells associated with axon fibers, and suggested a correlation between early axonal defects with neighboring dying mCherry+ cells or with the absence of mCherry labeling at both 48hpf and 72hpf (Figure 4.7E,F, insets). Because high concentrations of Mtz has been attributed to neurotoxic defects (Curado et al., 2007, Curado et al., 2008, Mathias et al., 2014), we additionally treated *gfap:eGFP*^{mi2001} embryos with Mtz and also assayed for changes in Gfap and AT patterning in the spinal cord. No radial glial or axonal defects were observed in treated

gfap:eGFP^{mi2001} embryos at any ages assayed throughout this study (data not shown), demonstrating that any observed phenotypes correspond to the direct loss of radial glia.

We next predicted that a breakdown in the pattern of neural circuits would cause functional defects in behavioral responses. Astroglia are known to play important roles regulating synapse function, and astroglial malfunction has been shown to generate abnormal swimming behavior (McKeown et al., 2012). The touch-response assay is a robust means to examine motor behavior in developing zebrafish, given that the associated motor outputs are well characterized and easily defined during embryogenesis (Granato et al., 1996; Saint-Amant and Drapeau, 1998). In collaboration with the Downes lab at University of Massachusetts, we defined the earliest point when behavioral defects could be observed following radial glial ablation by treating *gfap:nfsb-mCherry*^{sc059} embryos with either embryo medium, vehicle control, or Mtz and applying a touch stimulus to the head at 24hpf and 48hpf. Embryos treated with embryo medium were used to serve as a baseline control for any added effects from vehicle control treatment. At 24hpf, no differences in motor response (Figure 4.8A; mean tail coils: E3=1, DMSO=1.55, Mtz=1.64, $t_{E3xDMSO}$=1.35, p=0.21; t_{E3xMtz}=1.98, p=0.08; $t_{DMSxMtz}$=0.20, p=0.85) or touch sensitivity (Figure 4.8B; mean % response: E3=52%, DMSO=62%, Mtz=70%, $t_{E3xDMSO}$= 0.37, p=.73; t_{E3xMtz}=1.38, p=.24; $t_{DMSOxMtz}$=0.57, p=.60) was observed between the three treatment groups.

By 48hpf, the touch response in wild-type embryos has developed into a stereotyped escape response, beginning with a single high-amplitude 'C-like' body bend (defined here as a body angle that is greater than 110° or less than -110°) that reorients the larvae, followed by lower-amplitude body undulations that propel the embryo away

from the stimulus (Eaton et al, 1977; Saint-Amant and Drapeau, 1998). At this stage, Mtz treated embryos demonstrated a significantly decreased responsiveness to touch (Figure 4.8B, mean % response: E3=86%, DMSO=74%, Mtz=28%, $t_{E3xDMSO}$=1.72, p=.12; t_{E3xMtz}=6.55, p<.001; $t_{DMSOxMtz}$=4.91, p<.001). In addition to reduced touch responsiveness, behavior of Mtz-treated embryos differed significantly from DMSO or E3 embryos following ablation. At 48hpf, Mtz-treated embryos displayed supernumerary C-Like bends (Figure 4.8E) (E3=1.19, DMSO=1.69, Mtz=10.88), diminished linear velocity (Figure 4.8G) (E3=23.89mm/s, DMSO=21.31mm/s, Mtz=10.78mm/s), and prolonged overall response (Figure 4.8F) (E3=584ms, DMSO= 633ms, Mtz=1619ms). These findings were significantly different from both E3 (t=2.69, p=.02; t=6.54, p<.001; t=2.44, p=.03, respectively) and DMSO (t=2.55, p=.02; t=6.54, p<.001; t=2.29, p=.04, respectively), with no differences found between E3 and DMSO treated embryos for any measured characteristic (t=1.00, p=.33; t=1.00, p=.33; t=0.28, p=.79, respectively). Taken together, these data support a continuous role for radial glia in maintaining axon organization and synapse function throughout spinal cord development, which is necessary for proper swimming behavior.

4.4 Discussion

In this study we have generated and characterized two novel ablation lines that illustrate the direct involvement of radial glia on spinal cord development. These tools allowed us to confirm a stem-like role for *gfap*+ radial glia, as well as define a small population of *gfap*-negative, Sox2+ progenitors. In addition, we showed that loss of radial glia leads to reduced progenitor cell proliferation and loss of specific neuronal and

glial cell fates. We additionally demonstrated that loss of radial glia caused brain hemorrhaging and disruptions in axon patterning, confirming the important roles radial glia play in the structural organization of the CNS. Moreover, we provide evidence for a novel role in neural circuitry, as radial glial loss resulted in irregular locomotor behaviors. This study supports a model in which embryonic radial glial cells function to maintain spinal cord integrity and serve as the major stem cell population required for the generation of later born neurons and glial cells during late- and post-embryonic stages. These two genetic ablation tools will prove useful in testing the roles of astroglia in later CNS development, neuron-glial interactions and regeneration.

4.4.1 Astroglial ablation as a tool to study nervous system development

The most direct way to test the requirement of a cell type in the development of a given tissue is to remove that cell type and assess its impact to the system. To evaluate the role radial glial cells play in neural development, we chose the NTR ablation method for its promoter driven cell type specificity and clean apoptotic mechanism (Curado et al., 2008). We initially predicted that the *gfap:nfsb-mCherry* line would induce radial glial ablation early in development, coinciding with the onset of *gfap* expression previously observed in zebrafish. Previous reports using the same *gfap* regulatory elements driving fluorescent proteins noted that *gfap* driven expression was weakly present in the zebrafish spinal cord by 15hpf and intense labeling was present by 20hpf (Bernardos & Raymond, 2006), suggesting that the delay in radial glial cell death may be due to the natural progression of *gfap* expression over time. Following Mtz exposure, we noted a linear decrease in the expression of the mCherry reporter along with decreases in Gfap protein

expression predominantly in the ventral spinal cord, whereas as the dorsal region retained clustered mCherry+ fragments as late as 96hpf (Supplemental Figure 4.1, Figure 4.5). Interestingly, we noted continued bright expression of the mCherry reporter in the anterior CNS throughout our assays, indicating that this population of radial glia may regionally respond differently to Mtz treatment. Previous attempts to ablate radial glia using NTR driven by GFAP in mouse have also observed a regional restriction of ablation to the cerebellum (Cui et al., 2003), however this may be a restriction of the location of Gfap+ progenitor populations between species. Following Mtz-treatment, we did observe brain hemorrhaging that progressively worsened over time, likely due to the reduction in astroglial contributions wrapping the developing blood vessels that contribute to the overall blood brain vasculature (Figure 4.2). A similar observation has been made following ablation of astroglial specific integrins in the zebrafish that promote astroglial-vascular interactions, which ultimately resulted in brain hemorrhaging, motor defects, and reductions in neurons throughout the developing mouse CNS (McCarty et al., 2004). Due to the level of ablation we are able to achieve in the spinal cord, we report that our two *gfap:nfsb-mCherry* lines are the first transgenic tools to specifically and thoroughly eliminate radial glia to allow study of the different processes related to radial glial involvement during late embryonic CNS development.

4.4.2 Loss of NSCs and proliferative responses following *gfap*+ radial glial ablation

Often, a proliferative response follows injury in the CNS and other tissues as part of the repair mechanism (Curado et al., 2008, Goldshmit et al., 2012, Briona and Dorsky, 2014). This is likely due to the presence of resident progenitor cells such as astroglia,

ependymal cells or oligodendrocyte progenitors that upregulate Sox transcription factors and undergo proliferation to regenerate the injured tissue (Briona et al., 2015; Lee et al., 2012). Unfortunately radial glial ablation not only resulted in accumulating deficits in Sox2+ cells (Figure 4.4), but also severely reduced *nestin*+ (Figure 4.4) and *olig2*+ progenitor cell (Figure 4.6G-I) populations that could have responded to ablation by upregulating stem cell markers. Importantly, loss of Sox2 has been correlated with reductions in neuronal progenitor cells, proliferation deficits, inhibition of neuronal differentiation, and reductions in neurogenesis (Pevny & Nicolis 2010; Graham et al., 2003). In this study we report many of the same observations following radial glial ablation, supporting a requirement for Sox2+, *gfap*+ progenitors during spinal cord development. Following ablation, we observed a dramatic reduction in overall proliferation throughout the spinal cord between 48 and 72hpf (Figure 4.5), supporting a comprehensive role for Gfap+ radial glia as the primary dividing cell population in the spinal cord. Surprisingly while no change in proliferation was reported at 96hpf between control and Mtz-treated embryos (Figure 4.5I), we did observe a small portion of Sox2+/NTR-mCherry negative cells that were actively cycling at 96hpf (Figure 4.5K'-L", N). This suggests that the Sox2+/*gfap* negative population possesses the capacity to respond to injury even when a majority of the proliferative radial glial cells are gone.

Outside of the CNS, we did discover a response by proliferative populations to radial glial ablation in the spinal cord. Following ablation we observed increases in uniquely larger BrdU+ cells interacting with and spanning the border between the spinal cord and peripheral tissues at areas with decreased Gfap protein expression (Figure 4.5, Supplemental Figure 4.2). Previous astroglial ablation via irradiation in rats similarly

permitted Schwann cell invasion of the ventral spinal cord due to increased permeability of the CNS-vasculature interface (Sims et al., 1998). Therefore, we suspect that the presence of the "elongated/large" BrdU+ nuclei found at higher proportions at the border of the spinal cord of astroglial ablated embryos are represented by some portion of proliferative microglia, PNS glia (Schwann and perineurial glia), and/or other neural crest derivatives, although further confirmation is required. Our results strongly support a role for radial glia in establishing a peripheral spinal cord barrier that function in part to restrict PNS cells from entering the spinal cord.

4.4.3 Radial glial contributions to neurogenesis and gliogenesis

Previously, we have demonstrated that *gfap*+ radial glia likely act as the progenitor population for specific, later-born neurons and glial populations both directly through fate mapping (Chapter 3) and indirectly through mitotic inhibition of proliferative radial glia. In the present study, we have tested the requirement of Gfap+ radial glia for these secondary neuronal and glial populations and show conclusively that Gfap+ radial glia give rise to a majority of these populations in the zebrafish spinal cord. Importantly, the persistent decline in CoSA interneurons (Figure 4.6A-C), secondary motorneurons (Figure 4.6D-E), and oligodendroglia (Figure 4.6G-H) suggested that the reduced phenotypes were not the result of developmental delay, but rather suggested lack of generation or loss due to inheritance of the NTR-mCherry construct by radial glial progenitors. Interestingly, while we reported similar reductions in CoSA interneurons and *gata2*+ secondary motorneurons in ablated spinal cords as compared to our Kif11 study, we found that significantly more *olig2*+ lineage cells were lost following ablation (80%)

as opposed to mitotic inhibition (43%) at 72hpf. These results suggests two outcomes; either a significant portion of *olig2* progenitors do not rely on Kif11-mediated division to generate OPCs, or that radial glia transition into Olig2 lineages as opposed to generating them through division. Past support for radial glial transitions into oligodendroglial lineages has been reported in studies of rodent neural tissues (Fogarty et al., 2005; Choi & Kim 1985), however a closer analysis for potential transitional states in zebrafish is warranted.

4.4.4 Radial glia are required for the maintenance of axonal pattern and locomotor behavior

Following loss of radial glia, we observed a progressive loss of axon tract formation and organization over time. Upon closer examination, we noted that severe axon dysmorphisms were accompanied with mCherry+ fragments and reductions in Gfap+ glial endfeet (Figure 4.7), and propose the observed disorganization of spinal cord axons as result of losing a radial glial contact substrate. Radial glia are proposed to be necessary for axon pathfinding during embryonic development, demonstrated in the zebrafish forebrain where a Gfap+ radial glial "bridge" is established prior to axon crossing during commissure formation (Barresi et al, 2005), and acting as boundary cells for lateral axon tracts in the developing mouse spinal cord (reviewed in Barry, 2014). These interactions are reiterated in the adult zebrafish in spinal cord regeneration and repair, where a glial bridge spans the injury site to and acts as axon substrate in larval and adult zebrafish spinal cord (Briona & Dorsky 2014; Goldschmit et al., 2012).

In addition, axon phenotypes observed following ablation might reflect a reduction in neuronal populations that typically project axons laterally in the embryonic spinal cord. We noted that radial glial ablation resulted in the loss in the CoSA interneuron population (Figure 4.6A-C), a commissural neuron population known to project axons into the dorsal longitudinal fasciculus (DLF) in the spinal cord (reviewed in Martin & Ribera, 2013). The reductions in the CoSA population may also explain the alterations in swimming behavior observed in Mtz-treated embryos following a touch stimulus (Figure 4.8). CoSA interneurons represent a class of commissural locomotor neurons that are active during swimming behaviors and coordinate left-right alternation (reviewed in Lewis & Eisen 2003; Goulding 2009; Martin & Ribera 2013). Taken together, we hypothesize that the loss of this rhythmicity following radial glial ablation is likely due to a reduction in the CoSA interneuron component of the spinal commissural pathway.

4.5 Materials and Methods

4.5.1 Zebrafish

Adult zebrafish were maintained as described in Chapter 2 and Johnson et al., 2014. Fish lines used in this study were wild type (AB* and TU) (ZIRC and provided by Christian Lawrence, MGH), *tg(gfap:GFP^{mi2001})* (ZIRC), *tg(-3.9nestin:GFP)* (provided by Uwe Strahle), *tg(mnx1:eGFP)* (provided by Richard Dorsky), *tg(gata2:eGFP)* (provided by Shou Lin), *tg(olig2:eGFP)* (provided by Bruce Appel), *tg(mpeg:eGFP)* (Ellett et al., 2011), and *tg(pU1:eGFP)* (Peri and Nusslein-Volhard, 2008). The routine care of zebrafish embryos involved incubation at 28°C and a 12h light-dark cycle ((Westerfield,

2007); Zebrafish International Resource Center, ZIRC); however, Mtz treated embryos and their controls were maintained in total darkness due to the photosensitive nature of the drug.

4.5.2 Generation of *tg(gfap:nfsb-mCherry)*

Michael Parsons, Department of Surgery, Johns Hopkins University generated the *gfap:nfsb-mCherry* construct. The E. coli gene *nfsB* was previously amplified and cloned into T2KXIGDIN and subsequently subcloned in frame with mCherry on the C terminus of NTR as previously described (Pisharath et al., 2007). The 7.4 kb *gfap* promoter was PCR amplified with the inclusion of BAMH1 and Nco1 restriction sites, which were used to replace *Ins* in the *Ins:nfsB-mCherry* construct (Bernardos and Raymond, 2006, Pisharath et al., 2007). The resulting construct was microinjected at a concentration of 50ng/µl in combination with *Tol2* transposase mRNA to make transgenic fish (Kawakami, 2004). Two alleles were retained, *gfap:nfsB-mCherry*^{sc059} and *gfap:nfsB-mCherry*^{sc129}. F5 and F6 progeny from incrossed adults of the respective lines were used in the drug ablation studies.

4.5.3 Metronidazole treatments

Metronidazole treatments were largely conducted as previously described (Pisharath and Parsons, 2009). Working solutions of 10mM Metronidazole (Mtz, Sigma M3761) were prepared in E3 media containing 0.2% dimethyl sulfoxide (DMSO) and mixed for a minimum of 15 minutes prior to embryo application. Embryos were hand dechorionated and placed in treatment plates containing a layer of 1.5% agarose.

Treatments began at 8hpf when embryos were incubated at 28.5°C in either 10mM Mtz or vehicle control consisting of E3 media supplemented with 0.2% DMSO. All embryos were protected from light throughout the treatment periods until the endpoint stage was reached.

4.5.4 Live Imaging of Annexin-V expression

To record the process of apoptosis *in vivo* following induction of astroglial cell death, *gfap:nfsb-mCherry*^{sc129} embryos were injected at the one-cell stage with *UAS-SecA5-YFP* and *pCH-TBP-G4m* constructs each at 20ng/mL (modified from (van Ham et al., 2010)). Injected *gfap:nfsb-mCherry*^{sc129} embryos were then treated with control or Mtz solutions at 8hpf as described above. At 28hpf, Mtz and control treated embryos were anaesthetized with 1200ppm clove oil dissolved in fresh Mtz solution, and immobilized in 0.75% agarose for a dorsal view of the spinal cord on a 3.5cm glass-bottom culture dish (MatTek, Ashland, MA, USA). Time-lapse recordings were conducted on the Leica SP5 laser scanning confocal microscope. Z-stacks were obtained every 8' for 10h at an optical sectioning thickness of 0.55µm using a 63X water immersion objective. Time-lapse movies were processed using Volocity software. To verify that the progressive increase of Annexin-V labeling was consistent across all injected embryos, we imaged ten embryos per Mtz and control treated groups using a Zeiss Lumar V12 stereomicroscope every hour for the duration of the time-lapse.

4.5.5 BrdU treatments

For proliferation assays during ablation, *gfap:nfsB-mCherry*^{sc059} embryos were incubated in either vehicle control or 10mM Mtz until 24, 48, 72, or 96 hpf. Embryos were then treated with 10mM 5'-bromo-2-deoxyuridine (BrdU, Sigma, catalog no: B9285) diluted in either vehicle control or Mtz solution on ice for 15 minutes, then incubated at 28.5C for 5 minutes just prior to fixing. All embryos were fixed for 2H in 4% formaldehyde and processed for immunofluorescence.

4.5.6 Immunofluorescence

Embryonic tissue was collected and labeled as described in Chapter 3. Primary antibodies used in this study include rabbit anti-Gfap (1:500, Dako), mouse anti-Zrf1 (Gfap; 1:100, ZIRC), rabbit anti-Sox2 (1:500, Abcam), rabbit anti-GFP (1:300, Invitrogen), rabbit anti-activated Caspase-3 (1:500, BD Pharmingen), mouse anti-Acetylated Tubulin (AT; 1:800, Sigma), rat anti-BrdU (1:100, AbD Serotec), rabbit anti-GABA (1:1000, Sigma), and mouse anti-Islet-1 (39.4D5, 1:200, DSHB). Nuclei were visualized in sectioned tissue with Hoechst stain (1:30,000, Invitrogen).

4.5.7 Locomotor Analysis

All locomotor assays were conducted in collaboration with Chelsea Tyrrell and Dr. Gerald Downes, Department of Biology, University of Massachusetts Amherst. To characterize swimming behavior following ablation, *gfap:nfsB-mCherry*^{sc059} embryos were incubated in E3, vehicle control (DMSO), or Mtz. Touch-induced motor responses were recorded at 24hpf and 48hpf. A light touch stimulus was applied to the head region using a 3.22/0.16 g of force von Frey filament. Touch responsiveness was analyzed by

measuring the percentage of times each embryo or larvae generated a motor response over 5 trials. Locomotor responses were captured using a Fastec Imaging high-speed camera recording at 500 frames per second. Body angle, angular velocity, linear velocity, and response duration were calculated using FishTail, a semi-automated program created in the Downes lab (Friedrich et al., 2012, McKeown et al., 2012). Selected videos of 48hpf responses from each condition were edited for clarity in Image J. To generate rainbow overlays, individual frames from each selected video were imported into Adobe Illustrator and the body positions of the larvae were traced. Time points chosen for silhouetting were as follows: E3 Frame before response initiation (0ms), 20ms, 40ms, 120ms, 200ms, response end (500ms); DMSO response start (0ms), 20ms, 40ms, 120ms, 200ms, 280ms, response end (402ms); Mtz response start (0ms), 20ms, 40ms, 120ms, 200ms, 360ms, 520ms, 680ms, 840ms, 1000ms, 1160ms, 1320ms, 1480ms, response end (1602ms). The zero time point for each video is defined as the frame preceding that in which movement is first detected.

4.5.8 Imaging and Quantification

Images on fixed tissue samples were obtained using an AxioImager Z1 equipped with Apotome (Zeiss), and Z-stacks were collected with an optical sectioning thickness of 0.53μm at 40X (for whole mount tissue) or 0.31μm at 63X (for sections), and processed using Zen software (Zeiss). Lateral acquisitions of neuronal and glial populations were identified and quantified as previously described (Johnson et al., 2014). BrdU+ nuclei were averaged from images of three nonconsecutive sections per embryo, and the mean number of BrdU+ nuclei was determined per time point and condition. We

differentiated BrdU+ nuclei morphologies as either elongated or non-elongated nuclei by measuring nuclear volume using Volocity quantification. All quantitative results are displayed as the mean ± standard error of the mean, with *p* values generated from unpaired *t*-tests assuming equal variance at a significance level of 0.05.

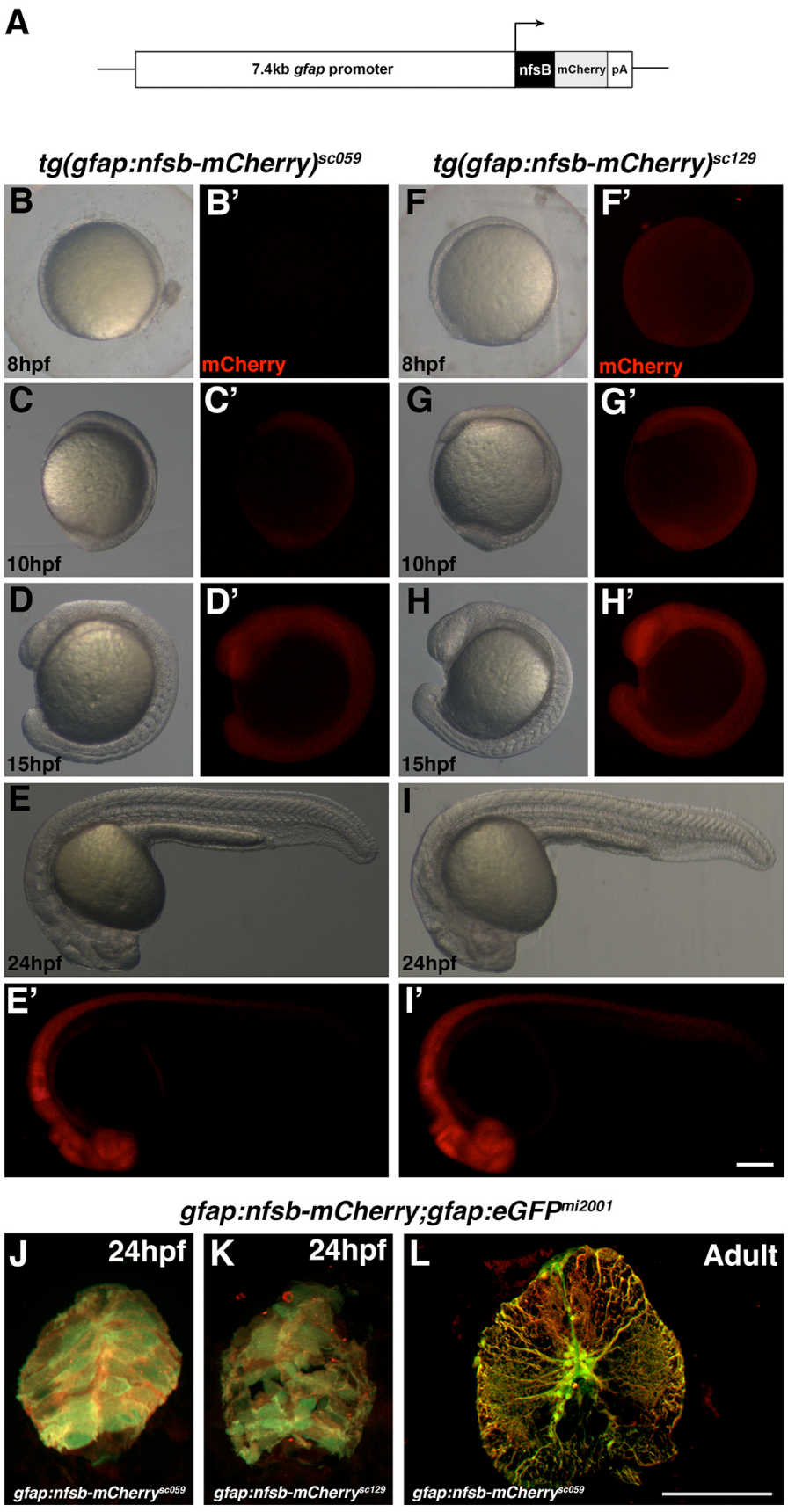
A
7.4kb gfap promoter
nfsB
mCherry
pA
tg(gfap:nfsb-mCherry)sc059
tg(gfap:nfsb-mCherry)sc129
B
B'
8hpf
mCherry
F
F'
8hpf
mCherry
C
C'
10hpf
G
G'
10hpf
D
D'
15hpf
H
H'
15hpf
E
24hpf
I
24hpf
E'
I'
gfap:nfsb-mCherry;gfap:eGFPmi2001
J
24hpf
gfap:nfsb-mCherrysc059
K
24hpf
gfap:nfsb-mCherrysc129
L
Adult
gfap:nfsb-mCherrysc059

Figure 4.1. Transgene expression of *gfap:nfsb-mCherry* alleles during embryonic development. (A) Diagram of the construct design using 7.4kb of the zebrafish *gfap* regulatory elements driving expression of the *E. coli nfsB* gene fused to the mCherry reporter. (B-I) Stable transgene expression in the *gfap:nfsb-mCherry*^{sc059} (B-E) and *gfap:nfsb-mCherry*^{sc129} (F-I) alleles over time. NTR-mCherry expression in the *gfap:nfsb-mCherry*^{sc059} allele (B-E) is absent at 8hpf (B,B'), dimly present within early neural tissues by 10hpf (C,C'), and more robust expression is present by 15hpf (D,D'). By 24hpf, strong NTR-mCherry expression restricted to the forebrain, hindbrain, spinal cord and eye can be observed. Expression patterns were similar in the *gfap:nfsb-mCherry*^{sc129} allele (F-I), with the onset of NTR-mCherry visible in ectodermal tissues as early as 8hpf (F,F'), becoming brighter and restricted to neural tissues by (G-I') 24hpf. Scale bar = 100μm. (J-L) Transgene expression of the two *gfap:nfsb-mCherry* alleles within the spinal cord as compared to *gfap:gfp*^{mi2001} line, which shares the same regulatory elements. Both the *nfsb*^{sc059} (J) and *nfsb*^{sc129} (K) alleles completely colocalize with GFP+ cells within the spinal cord at (L) 24hpf. This colocalization is maintained throughout adulthood. *nfsb*^{sc129} allele not shown. Scale bar = 100μm.

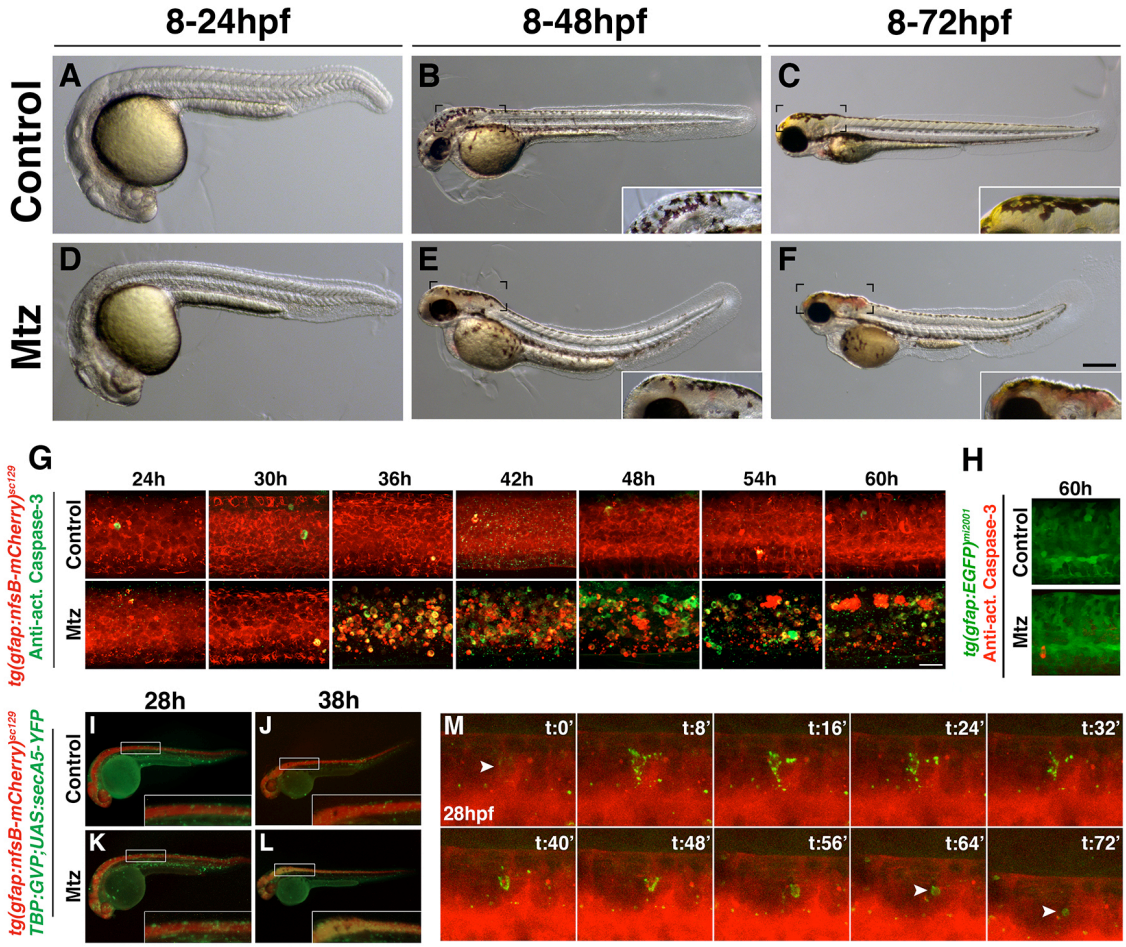

Figure 4.2. Metronidazole (Mtz) treatment induces neural defects and dynamic changes in mCherry expression during development. (A-C) Gross morphology of transgenic *gfap:nfsb-mCherry*^{sc059} embryos treated with vehicle control, showing no adverse effects associated with transgene expression. (D- F) Gross morphology of transgenic *gfap:nfsb-mCherry*^{sc059} embryos treated with Mtz from 8-24hpf showing onset of spinal curvature and brain hemorrhage (E, inset) that becomes more severe over time (F, inset). Scale bar = 100μm. (G, H) Lateral views of cell death within the spinal cord visualized by immunolabeling with Anti-activated Caspase-3. Robust death is detected by 36hpf in Mtz treated *gfap:nfsb-mCherry*^{sc129} embryos, whereas little to no cell death is observed in vehicle control or following treatment with Mtz in (H) *gfap:eGFP*^{mi2001}. Scale bar = 20μm. (I-M) Images of live *gfap:nfsb-mCherry*^{sc129} embryos at 28hpf and 38hpf expressing secreted Annexin-V YFP labeling. (I-J) Vehicle treated embryos showing dim Annexin-V labeling within the nervous system. (K, L) Mtz treated embryos showing accumulation of Annexin-V YFP with NTR-mCherry in neural tissues following Mtz treatment that appears to colocalize with NTR-mCherry in the insets. (M) Example of NTR-mCherry+ cell with radial glial morphology expressing Annexin-V (YFP) labeling undergoing apoptosis over the course of 72'.

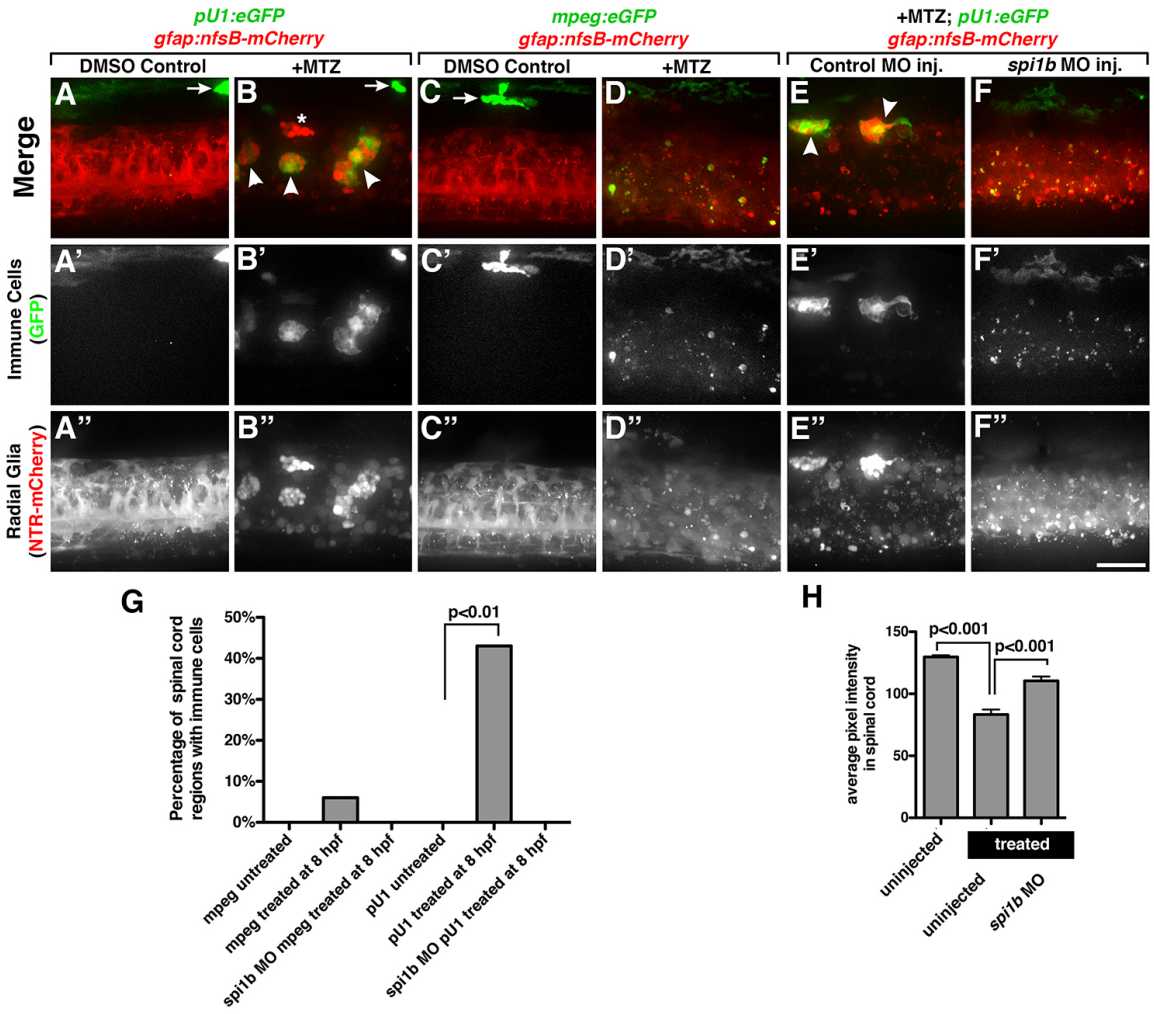

Figure 4.3. Spinal cord radial glial debris is cleared by microglia but not peripheral macrophages at 72hpf. (A-B") Lateral views of 72hpf double transgenic *gfap:nfsb-mCherry*^{sc059}*;pU1:egfp* embryo following treatment with vehicle control (A-A") or Mtz (B-B"). In both cases peripheral macrophages can be seen outside the neural tube (arrows), whereas microglial cells (arrowheads) are only present in Mtz treated embryos and coexpress mCherry+ debris in panel, B". (C-D") Lateral views of 72hpf double transgenic *gfap:nfsb-mCherry*^{sc059}*;mpeg:eGFP* embryo showing presence of macrophages following (C, C") control or (D-D") Mtz treatment. Macrophages were absent in both conditions, however, in panel D', GFP+ debris is evident following Mtz exposure and overlaps with NTR-mCherry+ debris, visible in panel D". (E-F") Lateral views of a 72hpf *gfap:nfsb-mCherry*^{sc059}*;pU1:eGFP* embryo injected with control or *spi1b* morpholino (*spi1b* MO) to inhibit myeloid progenitors and treated with Mtz. (E) Mtz treated embryos injected with control MO show GFP+ microglial cells (arrowheads) coexpressing NTR-mCherry+ and low overall levels of NTR-mCherry+ debris seen in panel E", in contrast to (F, F') *spi1b* MO injected embryos that lack immune cells and (F") exhibit accumulation of NTR-mCherry+ debris. (G) Quantification depicting percent of the total spinal cord with immune cells present in control (untreated) and Mtz (treated) embryos expressing either the *mpeg* or *pU1* promoter and injected with *spi1b* MO. Only

embryos treated with Mtz without *spi1b* knockdown contained immune cells within the spinal cord. (H) Quantification of the levels of NTR-mCherry+ expression through average pixel intensity in control embryos and embryos treated in Mtz that were either uninjected or injected with *spi1b* MO. Significantly less NTR-mCherry signal is detected in embryos treated with Mtz, however significantly more NTR-mCherry is detected following *spi1b* MO injection in Mtz treated embryos. Scale bar = 20μm.

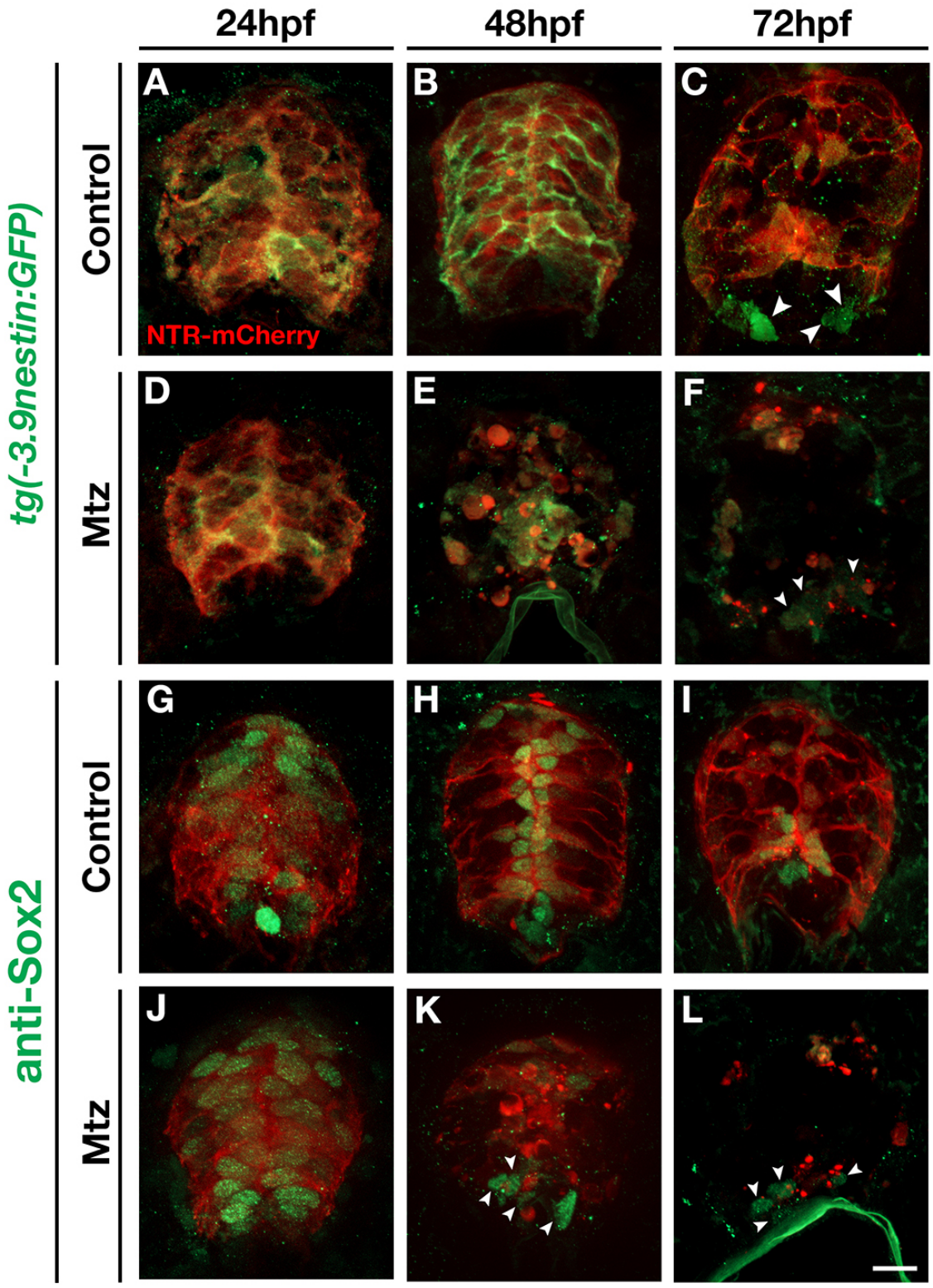

Figure 4.4. Radial glial ablation reduces the neural progenitor population. (A-F) Cross sections of 24hpf, 48hpf, and 72hpf double transgenic *gfap:nfsb-mCherry*^{sc059}*;-3.9nestin:GFP* embryos treated with (A-C) vehicle control or (D-F) Mtz. All sections

were immunolabeled with anti-GFP to enhance the signal of the *-3.9nestin:gfp* transgene. At all time points, GFP colocalized with NTR-mCherry+ cells in panels A, D or debris in panels E,F. (C, F) GFP+ cells lacking NTR-MCherry expression (arrowheads) in 72hpf embryo were not lost following ablation. (G-L) Cross section views of 24hpf, 48hpf and 72hpf *gfap:nfsb-mCherry*^{sc059} embryos immunolabeled with anti-Sox2 (green) to visualize neural stem cell populations following treatment with (G-I) vehicle control or (J-L)Mtz. In vehicle control treated embryos, Sox2+ nuclei localize along the lumen at all time points and are contained within NTR-mCherry+ cells. (J) 24hpf Mtz treated embryo showing similar luminal localization of Sox2+ populations as seen in panel G or vehicle control. However by (K, L) 48h and 72h, Mtz treated embryos show progressive and significant loss in Sox2+ cells, except the small population of Sox2+ cells ventral cord, that do not express NTR-mCherry (arrowheads). Scale bar = 10μm.

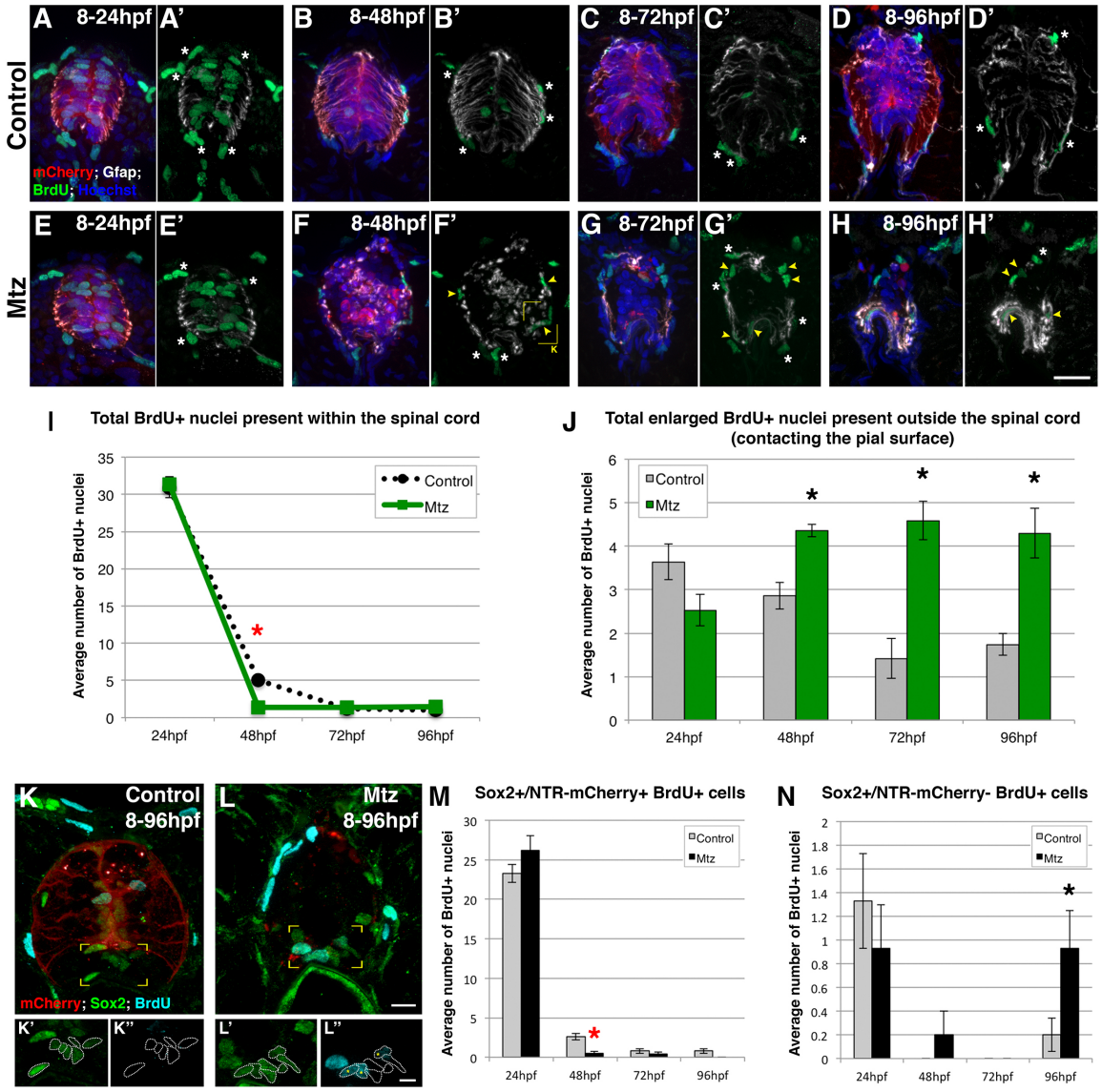

Figure 4.5. Radial glial ablation leads to reductions in proliferation and architectural integrity. (A-H') Cross section views of proliferative cells within spinal cords of (A-D') vehicle control and (E-H') Mtz treated embryos throughout neurogenesis visualized by immunolabeling with anti-BrdU (green), anti-Gfap (white) and Hoechst nuclear dye (blue). (A'-H') represent the same images in (A-H) but only showing anti-Gfap and anti-BrdU labeling. At all time points, elongated BrdU+ nuclei (white asterisks) can be seen in contact with Gfap+ spinal cord boundaries. In Mtz treated embryos, outer elongated nuclei are seen infiltrating the spinal cord at regions with decreased or absent Gfap staining (yellow arrowheads). Scale bar = 10µm. (I) Quantification of all BrdU+ populations visualized within the spinal cords between control (black line) and Mtz (green line) treatment groups. Significantly less BrdU nuclei were present in Mtz treated animals at 48hpf ($p<0.001$, red asterisk) until 72hpf when control nuclei populations were depleted. (J) Quantification of all elongated BrdU+ populations found outside of the spinal cord between vehicle control (grey) and Mtz (green) treatment groups.

Significantly more BrdU+ nuclei are present and contacting the Gfap+ spinal cord surface in Mtz treated embryos at 48hpf ($p<0.001$, black asterisks), and this trend remains constant through 96hpf. (K,L) Cross section views of (K) control and (L) Mtz treated embryos immunolabeled for BrdU (cyan) and Sox2 (green) at 96hpf. Scale bar = 10μm. (K'-L") Enlarged view of ventral Sox2+/NTR-mCherry negative cells (outlined) to denote cycling cells within this population (yellow asterisk). (M,N) Quantification of the two cycling Sox2+ populations present in the spinal cord following ablation. Scale bar = 5μm. (M) Significantly less cycling Sox2+ cells were observed at 48hpf following ablation as compared to control (red asterisk). (N) Significantly more cycling Sox2+/NTR-mCherry negative cells were observed at 96hpf as compared to controls (black asterisk). In all graphs, control averages are depicted in grey and Mtz averages are in black.

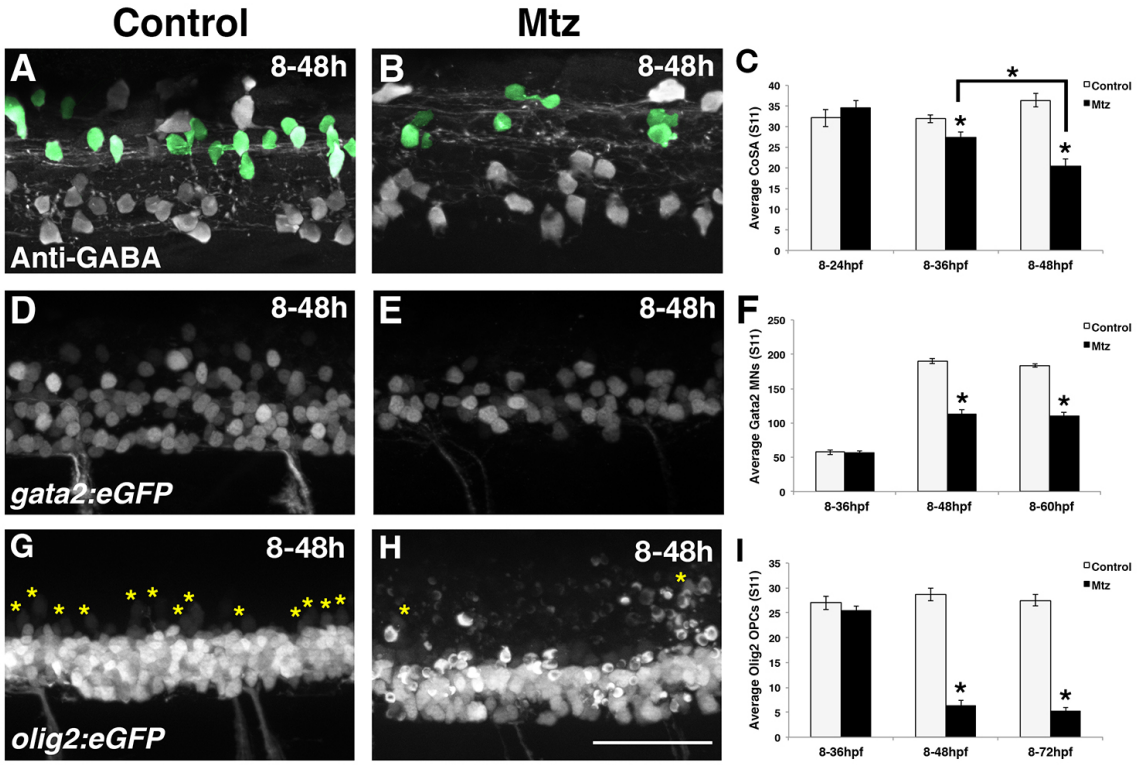

Figure 4.6. Reductions in later born neurons and glia are observed following radial glial ablation. (A,B) Lateral views of spinal cords showing interneurons immunolabeled with anti-GABA within control and Mtz-treated *gfap:nfsb-mCherry*^{sc129} embryos. The later-born CoSA population is highlighted in green to distinguish them from DoLA, VeLD, and KA populations. (C) Quantification of the CoSA population present at somite 11 over time following control (grey bars) and Mtz (black bars) treatment. By 36hpf, significantly less CoSA interneurons are present in the spinal cord in Mtz treated embryos, which continues to decline by 48hpf. (D, E) Lateral views of secondary motorneurons within control and Mtz treated *gfap:nfsb-mCherry*^{sc059}*;gata2:eGFP* embryos. (F) Quantification of secondary motorneurons present at somite 11 over neurogenesis. By 48hpf, significantly less Gata2+ secondary motorneurons were present in the spinal cord, and this loss is not recovered by 60hpf (black asterisks). (G, H) Lateral views of oligodendrocyte progenitor cells (OPCs, yellow asterisks) in control and Mtz treated *gfap:nfsb-mCherry*^{sc059}*;olig2:eGFP* embryos. GFP+ debris is highly evident following treatment with Mtz (H). (I) Quantification of OPCs present at somite 11 over neurogenesis. By 48hpf, significantly less OPCs were present in the dorsal spinal cord, and this reduction remains constant by 72hpf (black asterisks). Scale bar = 50µm.

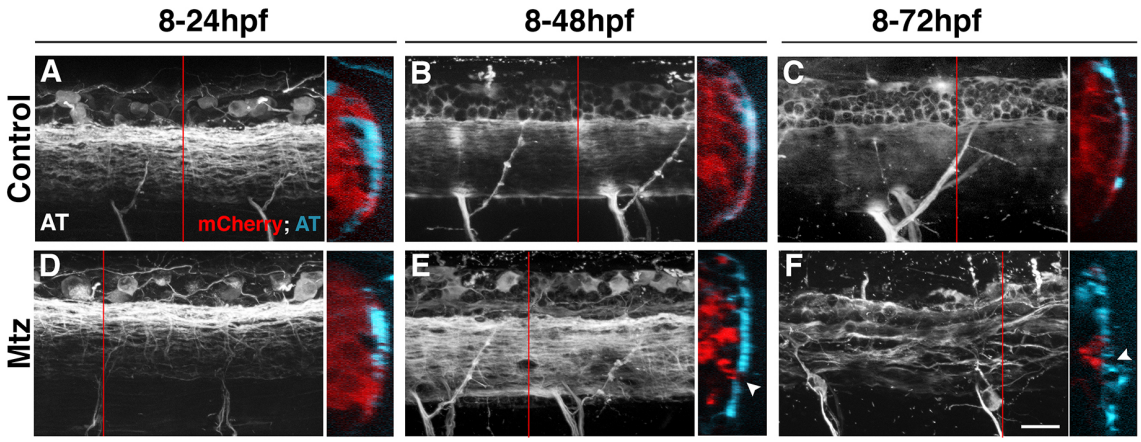

Figure 4.7. Reductions in later born neurons and glia are observed following radial glial ablation. (A-F) Lateral views of spinal cord axons within control and Mtz treated *gfap:nfsb-mcherry*^{sc059} embryos immunolabeled with anti-acetylated tubulin (AT, white). Alongside each image is an excerpt from the Z stack rotated along the X-axis to show correlations between NTR-mCherry (red) and AT labeling (blue). Red line depicts the location along the Z-axis where the rotated optical section is found. (A-C) Uniform, uninterrupted axon tracts are found throughout the spinal cords of control treated embryos at all time points assayed. (D) At 24hpf, no observable difference is seen in Mtz treated embryos prior to ablation as compared to its control (A). (E) At the onset of ablation, defects in axon organization can be observed in the spinal cord. When rotated, these defects (arrowheads) align with regions with reduced NTR-mCherry labeling or NTR-mCherry+ debris, which becomes more severe over time (F). Scale bar = 20µm.

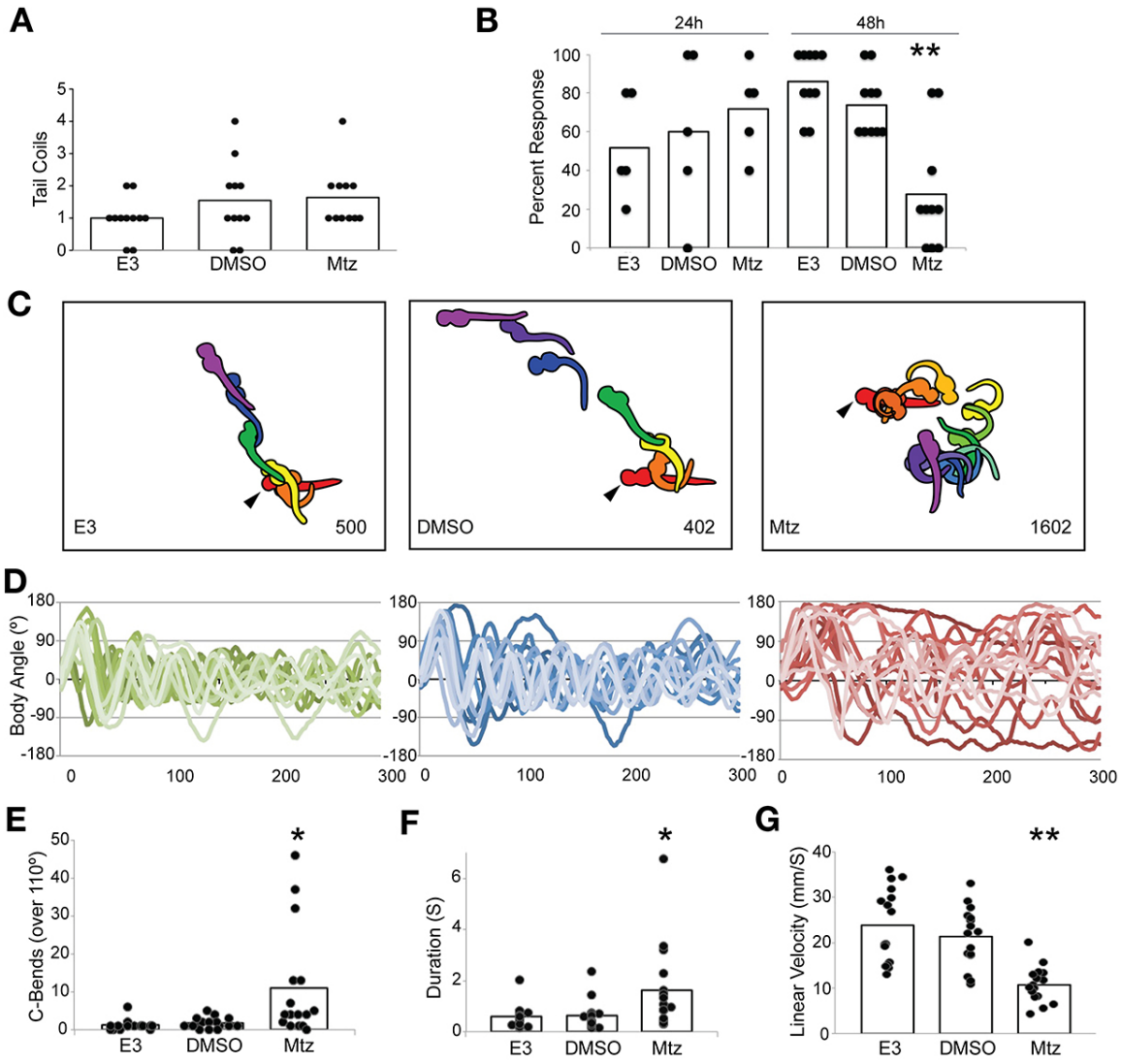

Figure 4.8. Radial glia ablation results in motor and sensory abnormalities at 48, but not 24, hours post fertilization. (A) Tail coils in response to touch stimulation at 24hpf. No significant difference was found between any of the conditions. (B) Touch sensitivity, as measured by percent of time a tactile stimulus elicited a motor response. No differences were found between conditions at 24hpf, but at 48hpf, Mtz-treated embryos were significantly less responsive to touch than their E3- or DMSO- treated siblings. (C) Rainbow overlays depicting escape response of the selected individual in the sample video provided for each condition. Response duration (ms) is listed in lower right-hand corner. The red silhouette represents embryo body position at the beginning of the response (arrow indicates head). The purple silhouette represents the embryo body position at the end of the response. Other color silhouettes represent intermediate time points. (D) Kinematics of escape response at 48hpf. Left to right: E3, DMSO, and Mtz. Body angle of 0° represents a straight embryo, while 180° and -180° represent head-to-tail touches. The sign of the body angle was assigned such that the first C-Bend occurs in the positive direction. (E) Mean number of C-Bends per condition at 48hpf. Mtz-treated embryos display a greater number of C-Bends than either E3 or DMSO conditions. (F)

Mean duration (s) of escape response at 48hpf. Mtz condition demonstrated a significantly prolonged response compared to either control condition. (G) Mean linear velocity (mm/s) at 48hpf. Mtz-treated embryo responses were characterized by significantly decreased linear velocity.

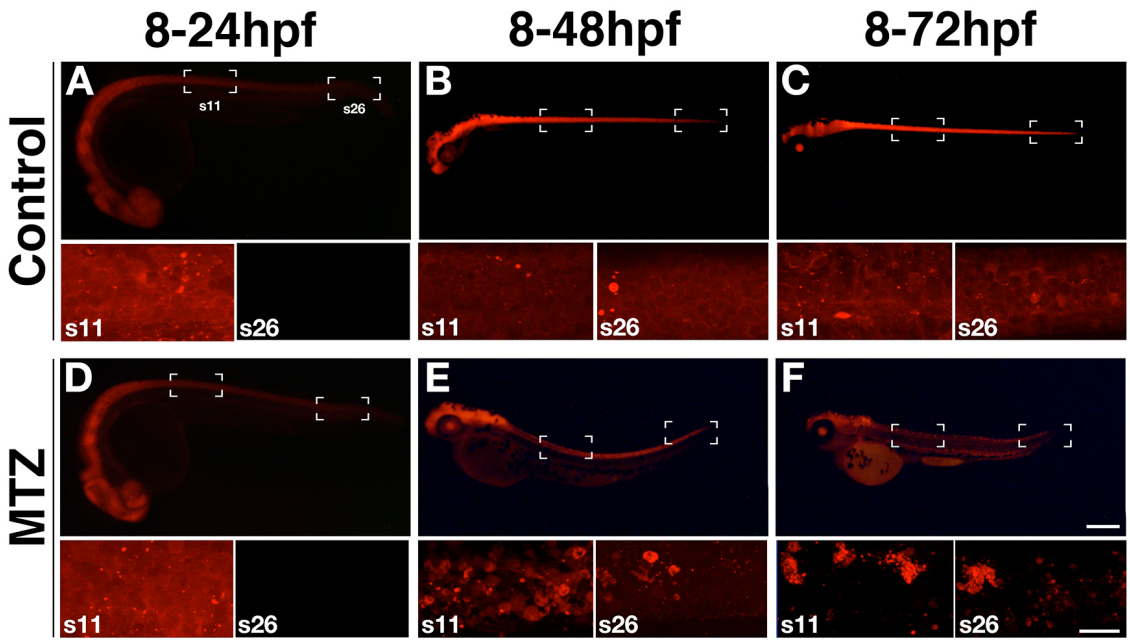

Supplemental Figure 4.1. Metronidazole (Mtz) treatment induces dynamic changes in mCherry expression during development. (A-F) Changes in NTR-mCherry expression correlate with timing of morphological defects in treated *gfap:nfsb-mCherry*^{sc059} embryos. (A) At 24hpf, NTR-mCherry expression is highest in the forebrain and anterior spinal cord (somite 11 inset) and weaker in the posterior spinal cord (somite 26 inset). (B,C) By 48hpf and 72hpf, bright NTR-mCherry expression is visible throughout the entire length of the neural tube (higher magnifications in insets). (D) At 24hpf, no change is observed in NTR-mCherry expression following Mtz treatment as compared to control (A). (E) Significant NTR-mCherry degradation is observed in the anterior spinal cord by 48hpf (s11 inset) which is reduced in the posterior spinal cord (s26 inset). (F) NTR-mCherry debris was dim throughout Mtz treated embryos, with NTR-mCherry debris present in the dorsal spinal cord (s11 inset) and extending into the posterior spinal cord (s26 inset). Scale bar in F = 100μm, scale bar in insets = 20μm.

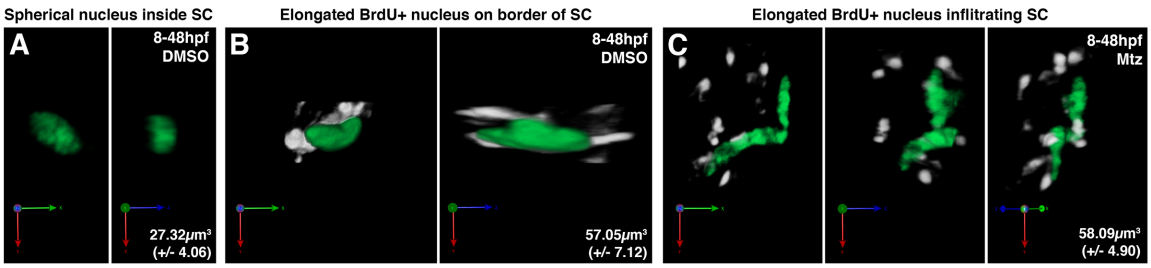

Supplemental Figure 4.2. Changes in BrdU+ nuclei present surrounding the neural tube following ablation. (A-C) Representative projections of nuclei found within (A) and outside (B-C) of the spinal cord. Outer nuclei are depicted with anti-Gfap labeling (white) to denote their relationship with the spinal cord border. Average volumes for each population are represented in each example.

CHAPTER 5

CONCLUSION AND FUTURE DIRECTIONS

5.1 Summary of Findings

The overall goal of this dissertation work is to provide insight on radial glial division and contribution to neurogenesis, gliogenesis, and overall patterning of the nervous system. In Chapter 2, I investigated how the mitotic kinesin Kif11 regulated radial glial division and ultimately neural development. By characterizing a mutation in the zebrafish *kif11* gene, I was able to identify a role for Kif11 mediating radial glial division throughout the neural tube. This led to the discovery that loss or inhibition of *kif11* results in mitotic arrest in radial glial cells. Moreover, pharmacological inhibition of Kif11 at distinct time points during embryonic development revealed when Kif11 is essential for radial glial division. In addition, collaborators and I generated a mathematical model of NSC dynamics during neurogenesis to predict how alterations in the radial glial population (inhibited division, altered cell cycle rates and cell death) affect CNS development that we confirmed experimentally. Lastly, I was able to indirectly discern that secondary neuronal and oligodendroglial lineages were generated Kif11-dependent radial glial divisions, and hypothesized that neuroepithelial cells generated primary neurons through Kif11-independent mechanisms.

In Chapter 3, collaborators and I generated a novel reporter line *tg(gfap:nls-mCherry)* that uses *glial fibrillary acidic protein (gfap)* regulatory regions to drive nuclear localized mCherry to visualize individual radial glial cells and act as a transient lineage reporter in downstream populations. I demonstrated that Gfap+ radial glial cells

are present in the spinal cord positioned at the lumen, widely recognized as a niche for stem cell populations. Further, I was able to identify two distinct cycling populations that express NSC markers in the spinal cord: *gfap*+ radial glial cells that coexpress *nestin* and Sox2 and a small population of *gfap*-, Sox2+ cells. Through fate mapping, I determined that subsets of interneurons, secondary motorneurons, and oligodendroglia originate from Gfap+ radial glia, supporting the hypothesis that Gfap+ radial glia act as a progenitor population during CNS development.

In Chapter 4, collaborators and I generated a tool to allow us to temporally remove radial glial from the spinal cord to assay how radial glia are required during vertebrate central nervous system (CNS) development and patterning. Robust ablation of *gfap*+ radial glia through use of the bacterial nitroreductase (NTR) system was induced throughout the CNS by late embryonic stages (36hpf) upon application of the prodrug Metronidazole (Mtz). Radial glial ablation resulted in significant loss of the *gfap*+, *nestin*+, Sox2+ NSC population as well as later-born neurons and glia, which could not be compensated for by other progenitor populations during embryonic neurogenesis. A late proliferative response by residual *gfap*-, Sox2+ NSCs was found following loss of radial glia, suggesting that they may be competent to respond to ablation in post-embryonic stages. Lastly, I showed that ablation of radial glia leads to brain hemorrhaging, disruptions in the organization of lateral axon tracts, and progressive abnormalities in touch responses and coordinated locomotion. Collectively, the results of this study aim to conclusively demonstrate the function of radial glia as the major embryonic neural stem cell, as well as display the diverse roles of radial glia throughout neural development.

5.1.1 Gfap+ radial glia are the major NSC in the zebrafish spinal cord

Radial glia are multipotent progenitor cells in the developing CNS across vertebrate species (Malatesta et al., 2000; Noctor et al., 2002; Anthony et al., 2004; and reviewed in Ihrie and Alvarez-Buylla, 2008; Pinto and Gotz, 2007). While significant work has been done on the role of radial glia and their progeny in the brain, much less is known about how radial glial proliferation help sculpt the spinal cord, and which specific neural lineages derive from spinal cord radial glia.

One of the main goals of this study was to confirm a neural stem/progenitor role for radial glia in the spinal cord through retention of stem cell markers, proliferative capacity, and the generation of multipotent lineages. We initially defined a portion of the radial glial population as mitotic through colabeling of anti-Gfap and the mitotic marker anti-phosphohistone H3 (Figure 2.2A,E insets). In doing so, we were the first to confirm that the "rounded up" radial glial morphology present at the luminal/ventricular surface of the zebrafish neural tube was indicative of a cell in mitosis as previously suspected (Tawk et al., 2007; Barresi et al., 2010). In later approaches, we labeled *gfap* expressing radial glia for *nestin* and Sox2 expression, two neural stem/progenitor markers essential for CNS development (Chen et al., 2010; Okuda et al., 2010; Graham et al., 2003) and identified that a majority of NSCs in the spinal cord are Gfap-expressing radial glial cells positioned along the lumen throughout embryonic neurogenesis (Figure 3.3A-F).

A major discrepancy in defining radial glia as a multipotent stem cell population was that between vertebrate species, not all radial glial cells give rise to both neurons and glial cells. In murine models, spinal cord radial glia were demonstrated to be exclusively gliogenic and solely produced oligodendrocytes and astrocytes (Choi et al., 1985; Leber

& Sanes, 1995; Hirano & Goldman 1988; Fogarty et al., 2005). Little evidence using Cre-based fate mapping techniques have illuminated that radial glial populations are present after the initiation of neurogenesis in mice (Anthony et al, 2004), however since neurogenesis had already begun, it was suggested that spinal cord radial glia do not participate in spinal cord neurogenesis. Recent research using the zebrafish model system, however, supported a role for radial glial populations producing some neuronal and oligodendroglial populations in the spinal cord (Briona & Dorsky, 2014; Kim et al., 2008; Bernardo & Raymond, 2006) suggesting that radial glia are present at the right time in development to be multipotent. In this study, we showed that radial glial proliferation can be observed as early as 15hpf in the zebrafish neural tube (Figure 2.2I,J) at a time when primary motorneurons are being generated and well before secondary motorneurons are found (Lewis et al., 2003). This contradicts views found in murine spinal cord models, and supports the model whereby radial glia are present in the spinal cord at times when they can contribute to neurogenesis. This discrepancy between model systems may be due to the abilities to view embryonic radial glial populations early in neural development in mice, as the method we used here (using Gfap as a radial glial label) can only visualize more mature radial glia in the mouse. It would be interesting to revisit this question in the mouse with tools refined to earlier developmental stages and determine more conclusively the role for radial glia in early spinal cord development.

Throughout the study we demonstrate that *gfap*+ radial glia are the major proliferative NSC population present in the spinal cord, and tested this directly by removing *gfap*+ radial glial cells and observing a near complete loss of proliferating in the spinal cord that was not rescued by another progenitor population (Figure 4.4, 4.5).

We also demonstrated that proliferation is temporally regulated throughout spinal cord development, and suggest that the radial glial stem/progenitor population is also subject to this regulation. When we inhibited Kif11 at different developmental stages, we discovered two critical time points when Kif11-mediated radial glial division was required during embryonic neurogenesis: between 5-10hpf, and between 15-20hpf (Figure 2.7). The first developmental time point was surprising, as *gfap* is not expressed in the neural tube until 10-12hpf (Kim et al., 2008; Bernardos & Raymond 2006). This suggested to us that Kif11 was likely required by the cells generating radial glia, thus impacting the generation of the radial glial population as a whole. Of interesting note was the lack of any difference in the requirement for Kif11-mediated division between 10hpf and 15hpf by radial glia. I hypothesize that this may reflect a stage in radial glial development between birth from neuroepithelial cells (onset of *gfap* at 10hpf) and the time in which it takes to go through the cell cycle (~5H; assumptions found in section 2.5.6: Mathematical Modeling; based of reference Leung et al., 2011) prior to entering into M-phase. The second time point, 15-20hpf, suggests a developmental stage where radial glial cells are probably competent to divide, and could perhaps serve as a time point in development when radial glia begin to act as progenitor cells and divide in a Kif11-dependent mechanism. This work thus better defines the period of time radial glial proliferation is required during neurogenesis, and helps clarify the role of radial glia as a stem/progenitor population during spinal cord development.

5.1.2. Gfap+ radial glia are the progenitor for secondary neurons and glia

We further supported a multipotent role for spinal cord radial glia by determining the specific lineages derived from Gfap+ radial glial divisions. Previous research in

zebrafish have supported this role, however knowledge of the specific types of neurons or glia that radial glia generate had not been well elucidated. Evidence for a multipotent role had been described using the first *gfap* transgenic line, where retention of the GFP transgene was found in neurons throughout the spinal cord (Bernardos & Raymond, 2006). Recently spinal cord radial glia have been shown to contribute to the generation of neurons and glia within the pMN domain of the ventral spinal cord in zebrafish (Kim H et al., 2008b, Kim & Dorsky 2011), as well as some undefined interneuron populations more dorsally (Briona & Dorsky, 2014). Further, failure to maintain Gfap+ progenitor cells reduced both secondary motorneuron and oligodendrocyte populations from the pMN domain of the ventral spinal cord (Kim et al., 2011), supporting a requirement of radial glia for these lineages. To build off of these studies, we have used a combination of mitotic inhibition, genetic ablation, and fate mapping approaches to show conclusively the specific lineages that Gfap+ radial glia give rise to during neural development in the spinal cord. The major findings of the three radial glial manipulation studies can be found below, in Table 1.

Table 5.1. Recorded changes between neural and glial populations present in the neural tube following radial glial manipulation, ablation, and fate mapping*

Cell Type	Kif11 inhibition	Radial glial Ablation	Gfap+ Fate Mapping
Sensory Neurons	No change	No change	No change
DoLA Interneurons	No change	No change	No change
CoSA Interneurons	42% reduction (30hpf)	41% reduction (48hpf)	67% (30hpf)
VeLD Interneurons	No change	No change	23% (30hpf)
KA Interneurons	No change	No change	No change
Primary Motorneurons	No change	No change	No change
Secondary Motorneurons	58% reduction (48hpf)	41% reduction (48hpf)	73% (48hpf)
Oligodendrocyte lineage cells	43% reduction (72hpf)	80% reduction (72hpf)	93% (72hpf)

*Ages reported reflect the latest time point this population was observed in the given study. Analyses of cell population changes over time are presented in Chapters 2 through 4.

Importantly when we compared the results from our three radial glial-manipulation studies, we found generally the same neuronal and glial cell types were affected throughout the study. Notably, use of the lineage reporter line identified a small portion of VeLD interneurons that retained residual expression of the *gfap*-transgene, suggesting a previously unrecognized role for radial glia in the generation of this population. The dependence of VeLD interneurons was likely overlooked following Kif11 inhibition and ablation due to the relatively small population shown to be derived from Gfap+ radial glial divisions (23%), and it is possible that reductions in too few VeLD interneurons following Kif11 inhibition or genetic ablation would not have been statistically significant. We hypothesize that this astroglial-dependent subset of VeLD interneurons is related to other radial glial derived pMN cells (motorneurons and oligodendroglia), as subsets of VeLD interneurons are known to express shared genes (*lim3, mnx*) with primary and secondary motorneurons located in the pMN domain (Appel et al., 1995, Park et al., 2004, Seredick et al., 2012).

Although we did report a similar reduction in CoSA interneurons and *gata2*+ secondary motorneurons following Kif11 inhibition (Johnson et al., 2014), assays conducted with our astroglial ablation model resulted in higher deficits in the same populations. For example, significantly more *olig2*+ lineage cells were lost following ablation at 72hpf (80% as opposed to 43% from mitotic inhibition). This result has two possible interpretations: either a significant portion of *olig2* progenitors do not rely on Kif11-mediated division to generate OPCs or that radial glia transition into Olig2 lineages as opposed to generating them through division. Past support for radial glial transitions into oligodendroglial lineages has been reported in studies of rodent neural

tissues (Choi and Kim, 1985, Fogarty et al., 2005); however, a closer analysis for potential transitional states in zebrafish is warranted. The results of this work conclusively delineates the specific neuronal and glial lineages that *gfap*+ radial glia contribute to during embryonic development, and proposes that earlier born neurons are likely generated by neuroepithelial cells. Identification of markers specific to neuroepithelial cells in zebrafish would be essential to confirm this hypothesis.

5.1.3 *gfap* negative progenitor populations exist in the spinal cord that do not compensate for loss of radial glia during embryonic development

Neuroepithelial cells and Gfap+ radial glia are not the only progenitor populations in the embryonic CNS (Figure 1.2). Neural stem/progenitor populations in the neural tube are heterogeneous and molecularly distinct along the dorsoventral axis of the neural tube, defined spatiotemporally by morphogen signaling gradients from tissues surrounding the neural tube. In fact, different populations of radial glial cells can be found throughout the spinal cord that do not express Gfap, which have been shown to directly give rise to neuronal populations in the zebrafish (Briona & Dorsky, 2014). When we were screening for Gfap+ radial glial division in the zebrafish spinal cord of wild type and *kif11* siblings, we identified a population of Ph3+ nuclei that were not found within Gfap+ radial glia (Figure 2.2J). We hypothesized that this population may be a combined pool of neural stem/progenitor cells, such as neuroepithelial cells, Gfap negative radial glia, or intermediate progenitor cells (nIPCs or OPCs; examples in Figure 1.2). Unfortunately no molecular marker specific to neuroepithelial cells currently exists in zebrafish, which would be essential to test this hypothesis. Through fate mapping and protein expression we also determined that proliferative OPCs not only use Kif11-mediated divisions, but

are also derived from Gfap+ radial glia (Figure 2.10; Figure 3.4). While we suspected that this population could also contribute to the lineages we described to be dependent on Gfap+ radial glia divisions (Figure 2.8, 2.9, 2.10; Table 5.1), we later confirmed through fate mapping that this was not the case (Figure 3.4; Table 5.1). How these progenitor cells are required for spinal cord development and their identity remains unknown.

When we investigated the portion of the NSC population, defined by expression of *nestin* and Sox2, that would be *gfap*+, we discovered that two discrete cell populations make up the Sox2+ neural stem/progenitor population in the zebrafish spinal cord: *gfap+, nestin*+, Sox2+ radial glial cells and Sox2+, *gfap* negative cells (Figure 3.3). This population of *gfap* negative, Sox2+ cells were predominantly positioned in the ventral spinal cord just dorsal to the lateral floorplate cells at all stages examined, although a few were observed in more dorsal locations. We show that both populations of Sox2+ cells have proliferative potential, but the highest rates of BrdU incorporation were found within the Sox2+/*gfap*+ fraction. Regardless, the limited proliferative capacity observed by Sox2+/*gfap* negative cells (33% between 24-48hpf, 2% between 48-72hpf; Figure 3.3I'-I"',J) supports their role as a unique population of stem/progenitor cells in the spinal cord. Further, these cells have been shown to be molecularly distinct from the *mnx1* motorneuron pool in the zebrafish spinal cord, suggesting that they are a stem/progenitor cells and not terminally differentiated (Jao et al., 2012). Unfortunately this study did not address this population of Sox2+/*gfap* negative cells further, so our study represents the first characterization of this population using proliferation assays to determine whether they act as progenitor cells.

Following acute injury models in zebrafish, an expansion of proliferating progenitor cells and increased Sox2 expression precedes reconnection of the severed tissue and regeneration of lost neurons and glia (Goldschmit et al., 2012; Lee et al., 2012; Briona & Dorsky 2014; Briona et al., 2015). Since a majority of the *gfap*+ cells lost following ablation were also Sox2+ (Figure 4.4), it was not surprising that an expansion of Sox2 expression was lacking in our system. However, we did observe that the Sox2+, *gfap* negative population was retained in the spinal cord following ablation of *gfap*+ radial glia, which both supports their role as a molecularly distinct subpopulation of the Sox2+ NSC pool and exemplifies the autonomy of our *gfap:nfsB-mCherry* ablation system to *gfap* expressing cells. Prior to 96hpf this population was relatively quiescent, with only a small fraction of this population actively cycling in both control and Mtz-treated embryos (Figure 4.5N). This population remained quiescent until 96hpf, when most of the Sox2+/NTR-mCherry+ cells were eliminated from the spinal cord (15% of the Sox2+/NTR-mCherry- cells were BrdU+ in Mtz as compared to 3.4% in controls) (Figure 4.5K'-L", N). This suggests that the Sox2+/*gfap* negative population possesses the capacity to respond to injury even when a majority of the proliferative radial glial cells are gone. This behavioral response by Sox2+/*gfap* negative cells in our study raises many new questions about their cellular identity and the level of potency these cells hold for the generation of new neurons and glial cells. Therefore, this work has provided a more comprehensive view of the progenitor populations constructing the spinal cord, and provides evidence towards the identification of new populations of non-radial glia that may be able to respond to injury models.

5.2 Future Studies

Prior to the initiation of this study, it was unclear the precise roles radial glia were required for during neural development. There were conflicting results on their role as a progenitor population largely due to differences in neural development, molecular markers, and the temporal distribution of radial glial populations between vertebrate systems. In this study we proposed three new tools to identify and manipulate radial glial cells, and through which have provided the first direct assays of radial glia as a progenitor and structural cell population during embryonic spinal cord development. We have shown that Gfap+ radial glia actively proliferate, retain NSC markers, and give rise to specific late born neurons and oligodendroglial populations in the zebrafish spinal cord. Use of these tools also helped identify a Sox2+, Gfap negative progenitor population that maintains the capacity to respond to loss of embryonic Gfap+ radial glia during larval development. Further, we provide initial evidence that radial glia are required structurally for axon maintenance in the spinal cord, neural tube integrity, and for blood brain barrier formation. The results of these studies provide a more comprehensive foundation for radial glial biology and their roles at different stages of embryonic CNS development.

With a more definitive view on radial glial roles as NSCs, understanding how radial glial proliferation is regulated throughout neural tube development can now be assayed. Morphogen gradients, such as Wnt or Sonic Hedgehog (Shh), have been shown to regulate NSC division and differentiation during neural development (reviewed in Schmidt et al., 2012), but how this pertains to radial glia is less understood. By using our nuclear *gfap* reporter line in combination with the proliferation assays outlined in this study, the effects of extrinsic signaling on radial glial division and differentiation during

neurogenesis can be investigated. Data acquired from these experiments can be applied into our mathematical model of neurogenesis to predict how signaling systems affect self-renewal, progeny generation, cell cycle rates, or influence cell death. Further, this program would facilitate prioritization of future experiments, as we showed previously (Chapter 2).

Astroglia are the main population that respond to CNS or injury models across vertebrates (Goldschmit et al., 2012; Lee et al., 2012; Briona & Dorsky 2014; Briona et al., 2015). In zebrafish, radial glia found in adult tissues are quiescent, but reactivate upon injury (Goldschmidt et al., 2012). In doing so, radial glia proliferate, extend processes to contact the disconnected halves of the neural tissue and act as a bridge to facilitate regrowth of the tissue (Goldschmidt et al., 2012). While radial glia have been shown to promote this process, it is unknown whether radial glia are truly required for this process, and which steps of the regenerative process are essential to facilitate tissue repair. The tools described in this study would enable researchers to determine which part of the regenerative process that radial glia are required for. Proliferation, expansion of progenitor pools and the regeneration of neurons can all be tested using the Kif11 system, with confirmation of radial glia performing these actions by using the nuclear *gfap* line as a lineage tracer. Roles in scaffolding could be assayed using our ablation model system, as well as an overall assay on radial glial involvement on CNS regeneration. A combination of these techniques would prove useful in furthering our understanding of neural development, with applications into understanding CNS disease and regeneration.

BIBLIOGRAPHY

Alexandre, P., Reugels, A.M., Barker, D., Blanc, E., Clarke, J.D., 2010. Neurons derive from the more apical daughter in asymmetric divisions in the zebrafish neural tube. Nat Neurosci 13, 673-679.

Amsterdam, A., Nissen, R.M., Sun, Z., Swindell, E.C., Farrington, S., Hopkins, N., 2004. Identification of 315 genes essential for early zebrafish development. Proc Natl Acad Sci U S A 101, 12792-12797.

Anthony, T.E., Klein, C., Fishell, G., and Heintz, N. (2004). Radial Glia Serve as Neuronal Progenitors in All Regions of the Central Nervous System. Neuron *41*, 881–890.

Appel, B., Chitnis, A., 2002. Neurogenesis and specification of neuronal identity. Results Probl Cell Differ 40, 237-251.

Appel, B., Eisen, J.S., 1998. Regulation of neuronal specification in the zebrafish spinal cord by Delta function. Development 125, 371-380.

Appel, B., Korzh, V., Glasgow, E., Thor, S., Edlund, T., Dawid, I.B., Eisen, J.S., 1995. Motoneuron fate specification revealed by patterned LIM homeobox gene expression in embryonic zebrafish. Development 121, 4117-4125.

Barresi, M.J., Burton, S., Dipietrantonio, K., Amsterdam, A., Hopkins, N., Karlstrom, R.O., 2010. Essential genes for astroglial development and axon pathfinding during zebrafish embryogenesis. Developmental dynamics : an official publication of the American Association of Anatomists 239, 2603-2618.

Barresi MJ, Hutson LD, Chien CB, Karlstrom RO (2005) Hedgehog regulated Slit expression determines commissure and glial cell position in the zebrafish forebrain. Development 132:3643-3656.

Barry D, McDermott K (2005) Differentiation of radial glia from radial precursor cells and transformation into astrocytes in the developing rat spinal cord. Glia 50:187-197.

Barry DS, Pakan JM, McDermott KW (2014) Radial glial cells: key organisers in CNS development. The international journal of biochemistry & cell biology 46:76-79.

Barry DS, Pakan JM, O'Keeffe GW, McDermott KW (2013) The spatial and temporal arrangement of the radial glial scaffold suggests a role in axon tract formation in the developing spinal cord. J Anat 222:203-213.

Beattie, C.E., Hatta, K., Halpern, M.E., Liu, H., Eisen, J.S., Kimmel, C.B., 1997. Temporal separation in the specification of primary and secondary motoneurons in zebrafish. Dev Biol (N Y 1985) 187, 171-182.

Bentivoglio M, Mazzarello P (1999) The history of radial glia. Brain Res Bull 49:305-315.

Bernardos RL, Raymond PA (2006) GFAP transgenic zebrafish. Gene Expr Patterns 6:1007-1013.

Bernhardt, R.R., Chitnis, A.B., Lindamer, L., Kuwada, J.Y., 1990. Identification of spinal neurons in the embryonic and larval zebrafish. J Comp Neurol 302, 603-616.

Bernhardt, R.R., Patel, C.K., Wilson, S.W., Kuwada, J.Y., 1992. Axonal trajectories and distribution of GABAergic spinal neurons in wildtype and mutant zebrafish lacking floor plate cells. J Comp Neurol 326, 263-272.

Bignami A, Dahl D (1977) Specificity of the glial fibrillary acidic protein for astroglia. J Histochem Cytochem 25:466-469.

Boniface EJ, Lu J, Victoroff T, Zhu M, Chen W (2009) FlEx-based transgenic reporter lines for visualization of Cre and Flp activity in live zebrafish. Genesis 47:484-491.

Brill A, Torchinsky A, Carp H, Toder V (1999) The role of apoptosis in normal and abnormal embryonic development. Journal of assisted reproduction and genetics 16:512-519.

Briona LK, Dorsky RI (2014) Radial glial progenitors repair the zebrafish spinal cord following transection. Exp Neurol 256:81-92.

Briona, L.K., Poulain, F.E., Mosimann, C., and Dorsky, R.I. (2015). Wnt/ß-catenin signaling is required for radial glial neurogenesis following spinal cord injury. Dev. Biol.

Brusco, A., Gomez, L.A., López, E.M., Tagliaferro, P., and Saavedra, J.P. (1995). Relationship between glial organization and the establishment of nerve tracts in rat spinal cord. Int. J. Neurosci. *82*, 25–31.

Castillo, A., Justice, M.J., 2007. The kinesin related motor protein, Eg5, is essential for maintenance of pre-implantation embryogenesis. Biochemical and biophysical research communications 357, 694-699.

Charras GT (2008) A short history of blebbing. Journal of microscopy 231:466-478.

Charras GT, Coughlin M, Mitchison TJ, Mahadevan L (2008) Life and times of a cellular bleb. Biophys J 94:1836-1853.

Chauviere, M., Kress, C., Kress, M., 2008. Disruption of the mitotic kinesin Eg5 gene (Knsl1) results in early embryonic lethality. Biochemical and biophysical research communications 372, 513-519.

Chen, H.-L., Yuh, C.-H., and Wu, K.K. (2010). Nestin is essential for zebrafish brain and eye development through control of progenitor cell apoptosis. PLoS ONE *5*, e9318.

Choi BH, Kim RC (1985) Expression of glial fibrillary acidic protein by immature oligodendroglia and its implications. Journal of neuroimmunology 8:215-235.

Chung, A.-Y., Kim, P.-S., Kim, S., Kim, E., Kim, D., Jeong, I., Kim, H.-K., Ryu, J.-H., Kim, C.-H., Choi, J., et al. (2013). Generation of demyelination models by targeted ablation of oligodendrocytes in the zebrafish CNS. Mol. Cells *36*, 82–87.

Ciruna, B., Jenny, A., Lee, D., Mlodzik, M., Schier, A.F., 2006. Planar cell polarity signalling couples cell division and morphogenesis during neurulation. Nature 439, 220-224.

Cochran, J.C., Gatial, J.E., 3rd, Kapoor, T.M., Gilbert, S.P., 2005. Monastrol inhibition of the mitotic kinesin Eg5. The Journal of biological chemistry 280, 12658-12667.

Copp, A.J., Greene, N.D., Murdoch, J.N., 2003. The genetic basis of mammalian neurulation. Nat Rev Genet 4, 784-793.

Cui W, Allen ND, Skynner M, Gusterson B, Clark AJ (2001) Inducible ablation of astrocytes shows that these cells are required for neuronal survival in the adult brain. Glia 34:272-282.

Curado S, Anderson RM, Jungblut B, Mumm J, Schroeter E, Stainier DY (2007) Conditional targeted cell ablation in zebrafish: a new tool for regeneration studies. Dev Dyn 236:1025-1035.

Curado S, Stainier DY, Anderson RM (2008) Nitroreductase-mediated cell/tissue ablation in zebrafish: a spatially and temporally controlled ablation method with applications in developmental and regeneration studies. Nat Protoc 3:948-954.

Dahlstrand, J., Lardelli, M., and Lendahl, U. (1995). Nestin mRNA expression correlates with the central nervous system progenitor cell state in many, but not all, regions of developing central nervous system. Brain Res. Dev. Brain Res. *84*, 109–129.

DeBonis, S., Skoufias, D.A., Lebeau, L., Lopez, R., Robin, G., Margolis, R.L., Wade, R.H., Kozielski, F., 2004. In vitro screening for inhibitors of the human mitotic kinesin Eg5 with antimitotic and antitumor activities. Mol Cancer Ther 3, 1079-1090.

Dekens, M.P., Pelegri, F.J., Maischein, H.M., Nusslein-Volhard, C., 2003. The maternal-effect gene futile cycle is essential for pronuclear congression and mitotic spindle assembly in the zebrafish zygote. Development 130, 3907-3916.

Delaney CL, Brenner M, Messing A (1996) Conditional ablation of cerebellar astrocytes in postnatal transgenic mice. J Neurosci 16:6908-6918.

Demerens, C., Stankoff, B., Logak, M., Anglade, P., Allinquant, B., Couraud, F., Zalc, B., and Lubetzki, C. (1996). Induction of myelination in the central nervous system by electrical activity. Proc Natl Acad Sci U S A *93*, 9887–9892.

Demir, O., Singh, S., Klimaschewski, L., Kurnaz, I.A., 2009. From birth till death: neurogenesis, cell cycle, and neurodegeneration. Anatomical record 292, 1953-1961.

Devoto, S.H., Melancon, E., Eisen, J.S., Westerfield, M., 1996. Identification of separate slow and fast muscle precursor cells in vivo, prior to somite formation. Development 122, 3371-3380.

Ellett F, Pase L, Hayman JW, Andrianopoulos A, Lieschke GJ (2011) mpeg1 promoter transgenes direct macrophage-lineage expression in zebrafish. Blood 117:e49-56.

Ellis, P., Fagan, B.M., Magness, S.T., Hutton, S., Taranova, O., Hayashi, S., McMahon, A., Rao, M., and Pevny, L. (2004). SOX2, a persistent marker for multipotential neural stem cells derived from embryonic stem cells, the embryo or the adult. Dev. Neurosci. *26*, 148–165.

Ferhat, L., Cook, C., Chauviere, M., Harper, M., Kress, M., Lyons, G.E., Baas, P.W., 1998. Expression of the mitotic motor protein Eg5 in postmitotic neurons: implications for neuronal development. J Neurosci 18, 7822-7835.

Flanagan-Steet H, Fox MA, Meyer D, Sanes JR (2005) Neuromuscular synapses can form in vivo by incorporation of initially aneural postsynaptic specializations. Development 132:4471-4481.

Fogarty M, Richardson WD, Kessaris N (2005) A subset of oligodendrocytes generated from radial glia in the dorsal spinal cord. Development 132:1951-1959.

Friedrich T, Lambert AM, Masino MA, Downes GB (2012) Mutation of zebrafish dihydrolipoamide branched-chain transacylase E2 results in motor dysfunction and models maple syrup urine disease. Disease models & mechanisms 5:248-258.

Gartner, M., Sunder-Plassmann, N., Seiler, J., Utz, M., Vernos, I., Surrey, T., Giannis, A., 2005. Development and biological evaluation of potent and specific inhibitors of mitotic Kinesin Eg5. Chembiochem 6, 1173-1177.

Gasser, U.E., and Hatten, M.E. (1990). Central nervous system neurons migrate on astroglial fibers from heterotypic brain regions in vitro. Proc Natl Acad Sci U S A *87*, 4543–4547.

Gerhardt H, Ruhrberg C, Abramsson A, Fujisawa H, Shima D, Betsholtz C (2004) Neuropilin-1 is required for endothelial tip cell guidance in the developing central nervous system. Dev Dyn 231:503-509.

Goldshmit Y, Sztal TE, Jusuf PR, Hall TE, Nguyen-Chi M, Currie PD (2012) Fgf-dependent glial cell bridges facilitate spinal cord regeneration in zebrafish. J Neurosci 32:7477-7492.

Gotz, M., Huttner, W.B., 2005. The cell biology of neurogenesis. Nat Rev Mol Cell Biol 6, 777-788.

Goulding M (2009) Circuits controlling vertebrate locomotion: moving in a new direction. Nat Rev Neurosci 10:507-518.

Graham, V., Khudyakov, J., Ellis, P., and Pevny, L. (2003). SOX2 functions to maintain neural progenitor identity. Neuron *39*, 749–765.

Grandel, H., Brand, M., 2013. Comparative aspects of adult neural stem cell activity in vertebrates. Development genes and evolution 223, 131-147.

Gruber, J., Manninga, H., Tuschl, T., Osborn, M., Weber, K., 2005. Specific RNAi mediated gene knockdown in zebrafish cell lines. RNA Biol 2, 101-105.

Hartfuss, E., Galli, R., Heins, N., and Götz, M. (2001). Characterization of CNS precursor subtypes and radial glia. Dev. Biol. *229*, 15–30.

Herbomel P, Thisse B, Thisse C (1999) Ontogeny and behaviour of early macrophages in the zebrafish embryo. Development 126:3735-3745.

Hidalgo A, Urban J, Brand AH (1995) Targeted ablation of glia disrupts axon tract formation in the Drosophila CNS. Development 121:3703-3712.

Hirano, M., and Goldman, J.E. (1988). Gliogenesis in rat spinal cord: evidence for origin of astrocytes and oligodendrocytes from radial precursors. J. Neurosci. Res. *21*, 155–167.

Hockfield, S., and McKay, R.D. (1985). Identification of major cell classes in the developing mammalian nervous system. J. Neurosci. *5*, 3310–3328.

Hollyday, M., 2001. Neurogenesis in the vertebrate neural tube. Int J Dev Neurosci 19, 161-173.

Huang, P., Xiong, F., Megason, S.G., Schier, A.F., 2012. Attenuation of Notch and Hedgehog signaling is required for fate specification in the spinal cord. PLoS genetics 8, e1002762.

Hudish, L.I., Blasky, A.J., and Appel, B. (2013). miR-219 regulates neural precursor differentiation by direct inhibition of apical par polarity proteins. Dev. Cell *27*, 387–398.

Huppertz B, Frank HG, Kaufmann P (1999) The apoptosis cascade--morphological and immunohistochemical methods for its visualization. Anat Embryol (Berl) 200:1-18.

Hutchinson SA, Eisen JS (2006) Islet1 and Islet2 have equivalent abilities to promote motoneuron formation and to specify motoneuron subtype identity. Development 133:2137-2147.

Ihrie, R.A., Alvarez-Buylla, A., 2008. Cells in the astroglial lineage are neural stem cells. Cell Tissue Res 331, 179-191.

Inagaki, M., Nakamura, Y., Takeda, M., Nishimura, T., Inagaki, N., 1994. Glial fibrillary acidic protein: dynamic property and regulation by phosphorylation. Brain Pathol 4, 239-243.

Jacobs JR, Goodman CS (1989) Embryonic development of axon pathways in the Drosophila CNS. I. A glial scaffold appears before the first growth cones. J Neurosci 9:2402-2411.

Jao, L.-E., Appel, B., and Wente, S.R. (2012). A zebrafish model of lethal congenital contracture syndrome 1 reveals Gle1 function in spinal neural precursor survival and motor axon arborization. Development *139*, 1316–1326.

Johnson K, Moriarty C, Tania N, Ortman A, DiPietrantonio K, Edens B, Eisenman J, Ok D, Krikorian S, Barragan J, Gole C, Barresi MJ (2014) Kif11 dependent cell cycle progression in radial glial cells is required for proper neurogenesis in the zebrafish neural tube. Dev Biol 387:73-92.

Joosten, E.A.J., and Gribnau, A.A.M. (1989). Astrocytes and guidance of outgrowing corticospinal tract axons in the rat. An immunocytochemical study using anti-vimentin and anti-glial fibrillary acidic protein. Neuroscience *31*, 439–452.

Jowett, T., 1997. Tissue in situ hybridization: methods in animal development. John Wiley & Sons, Inc, New York.

Kapitein, L.C., Peterman, E.J., Kwok, B.H., Kim, J.H., Kapoor, T.M., Schmidt, C.F., 2005. The bipolar mitotic kinesin Eg5 moves on both microtubules that it crosslinks. Nature 435, 114-118.

Kapoor, T.M., Mayer, T.U., Coughlin, M.L., Mitchison, T.J., 2000. Probing spindle assembly mechanisms with monastrol, a small molecule inhibitor of the mitotic kinesin, Eg5. The Journal of cell biology 150, 975-988.

Kawaguchi, A., Ikawa, T., Kasukawa, T., Ueda, H.R., Kurimoto, K., Saitou, M., Matsuzaki, F., 2008a. Single-cell gene profiling defines differential progenitor subclasses in mammalian neurogenesis. Development 135, 3113-3124.

Kawaguchi, D., Yoshimatsu, T., Hozumi, K., Gotoh, Y., 2008b. Selection of differentiating cells by different levels of delta-like 1 among neural precursor cells in the developing mouse telencephalon. Development 135, 3849-3858.

Kawai, H., Arata, N., and Nakayasu, H. (2001). Three-dimensional distribution of astrocytes in zebrafish spinal cord. Glia *36*, 406–413.

Kawakami K (2004) Transgenesis and gene trap methods in zebrafish by using the Tol2 transposable element. Methods Cell Biol 77:201-222.

Kerr JF, Wyllie AH, Currie AR (1972) Apoptosis: a basic biological phenomenon with wide-ranging implications in tissue kinetics. British journal of cancer 26:239-257.

Khurgel M, Koo AC, Ivy GO (1996) Selective ablation of astrocytes by intracerebral injections of alpha-aminoadipate. Glia 16:351-358.

Kim, H., Kim, S., Chung, A.-Y., Bae, Y.-K., Hibi, M., Lim, C.S., and Park, H.-C. (2008a). Notch-regulated perineurium development from zebrafish spinal cord. Neurosci. Lett. *448*, 240–244.

Kim H, Shin J, Kim S, Poling J, Park HC, Appel B (2008b) Notch-regulated oligodendrocyte specification from radial glia in the spinal cord of zebrafish embryos. Dev Dyn 237:2081-2089.

Kim, H.T., So, J.H., Jung, S.H., Ahn, D.G., Koh, W., Kim, N.S., Kim, S.H., Lee, S., Kim, C.H., 2011. Cug2 is essential for normal mitotic control and CNS development in zebrafish. BMC developmental biology 11, 49.

Kimmel, C.B., Warga, R.M., Kane, D.A., 1994. Cell cycles and clonal strings during formation of the zebrafish central nervous system. Development 120, 265-276.

Kirby BB, Takada N, Latimer AJ, Shin J, Carney TJ, Kelsh RN, Appel B (2006) In vivo time-lapse imaging shows dynamic oligodendrocyte progenitor behavior during zebrafish development. Nat Neurosci 9:1506-1511.

Kozielski, F., Skoufias, D.A., Indorato, R.L., Saoudi, Y., Jungblut, P.R., Hustoft, H.K., Strozynski, M., Thiede, B., 2008. Proteome analysis of apoptosis signaling by S-trityl-L-

cysteine, a potent reversible inhibitor of human mitotic kinesin Eg5. Proteomics 8, 289-300.

Kriegstein A, Alvarez-Buylla A (2009) The glial nature of embryonic and adult neural stem cells. Annu Rev Neurosci 32:149-184.

Kroehne V, Freudenreich D, Hans S, Kaslin J, Brand M (2011) Regeneration of the adult zebrafish brain from neurogenic radial glia-type progenitors. Development 138:4831-4841.

Krzysiak, T.C., Grabe, M., Gilbert, S.P., 2008. Getting in sync with dimeric Eg5. Initiation and regulation of the processive run. The Journal of biological chemistry 283, 2078-2087.

Kucenas, S., Takada, N., Park, H.C., Woodruff, E., Broadie, K., Appel, B., 2008. CNS-derived glia ensheath peripheral nerves and mediate motor root development. Nat Neurosci 11, 143-151.

Kuo, B.R., Erickson, C.A., 2010. Regional differences in neural crest morphogenesis. Cell Adh Migr 4, 567-585.

Lam, C.S., März, M., and Strähle, U. (2009). gfap and nestin reporter lines reveal characteristics of neural progenitors in the adult zebrafish brain. Dev. Dyn. *238*, 475–486.

Latasa, M.J., Cisneros, E., and Frade, J.M. (2009). Cell cycle control of Notch signaling and the functional regionalization of the neuroepithelium during vertebrate neurogenesis. Int. J. Dev. Biol. *53*, 895–908.

Le Belle, J.E., Sperry, J., Ngo, A., Ghochani, Y., Laks, D.R., López-Aranda, M., Silva, A.J., and Kornblum, H.I. (2014). Maternal Inflammation Contributes to Brain Overgrowth and Autism-Associated Behaviors through Altered Redox Signaling in Stem and Progenitor Cells. Stem Cell Reports *3*, 725–734.

Leber, S.M., and Sanes, J.R. (1995). Migratory paths of neurons and glia in the embryonic chick spinal cord. J. Neurosci. *15*, 1236–1248.

Lee H, Song MR (2013) The structural role of radial glial endfeet in confining spinal motor neuron somata is controlled by the Reelin and Notch pathways. Exp Neurol 249:83-94.

Lee HJ, Wu J, Chung J, Wrathall JR (2012) SOX2 expression is upregulated in adult spinal cord after contusion injury in both oligodendrocyte lineage and epndymal cells. J Neurosci 91(2):196-210.

Leung, L., Klopper, A.V., Grill, S.W., Harris, W.A., Norden, C., 2011. Apical migration of nuclei during G2 is a prerequisite for all nuclear motion in zebrafish neuroepithelia. Development 138, 5003-5013.

Lewis KE, Eisen JS (2003) From cells to circuits: development of the zebrafish spinal cord. Prog Neurobiol 69:419-449.

Lindwall C, Fothergill T, Richards LJ (2007) Commissure formation in the mammalian forebrain. Curr Opin Neurobiol 17:3-14.

Ma, S., Kwon, H.J., Johng, H., Zang, K., and Huang, Z. (2013). Radial Glial Neural Progenitors Regulate Nascent Brain Vascular Network Stabilization Via Inhibition of Wnt Signaling. PLoS Biol *11*, e1001469.

Mahler, J., and Driever, W. (2007). Expression of the zebrafish intermediate neurofilament Nestin in the developing nervous system and in neural proliferation zones at postembryonic stages. BMC Dev Biol *7*, 1–11.

Malatesta P, Hartfuss E, Gotz M (2000) Isolation of radial glial cells by fluorescent-activated cell sorting reveals a neuronal lineage. Development 127:5253-5263.

Marcus, A.I., Peters, U., Thomas, S.L., Garrett, S., Zelnak, A., Kapoor, T.M., Giannakakou, P., 2005. Mitotic kinesin inhibitors induce mitotic arrest and cell death in Taxol-resistant and -sensitive cancer cells. The Journal of biological chemistry 280, 11569-11577.

Marcus RC, Easter SS, Jr. (1995) Expression of glial fibrillary acidic protein and its relation to tract formation in embryonic zebrafish (Danio rerio). J Comp Neurol 359:365-381.

Martin TC, Ribera AB (2013) Lessons from zebrafish: Ion channels guide neuronal development. : Elsevier.

März, M., Chapouton, P., Diotel, N., Vaillant, C., Hesl, B., Takamiya, M., Lam, C.S., Kah, O., Bally-Cuif, L., and Strähle, U. (2010). Heterogeneity in progenitor cell subtypes in the ventricular zone of the zebrafish adult telencephalon. Glia *58*, 870–888.

Mathias JR, Zhang Z, Saxena MT, Mumm JS (2014) Enhanced Cell-Specific Ablation in Zebrafish Using a Triple Mutant of Escherichia Coli Nitroreductase. Zebrafish.

Mayer, T.U., Kapoor, T.M., Haggarty, S.J., King, R.W., Schreiber, S.L., Mitchison, T.J., 1999. Small molecule inhibitor of mitotic spindle bipolarity identified in a phenotype-based screen. Science 286, 971-974.

McCarty JH (2005) Cell biology of the neurovascular unit: implications for drug delivery across the blood-brain barrier. Assay and drug development technologies 3:89-95.

McCarty JH, Lacy-Hulbert A, Charest A, Bronson RT, Crowley D, Housman D, Savill J, Roes J, Hynes RO (2005) Selective ablation of alphav integrins in the central nervous system leads to cerebral hemorrhage, seizures, axonal degeneration and premature death. Development 132:165-176.

McDermott KW, Barry DS, McMahon SS (2005) Role of radial glia in cytogenesis, patterning and boundary formation in the developing spinal cord. J Anat 207:241-250.

McKeown KA, Moreno R, Hall VL, Ribera AB, Downes GB (2012) Disruption of Eaat2b, a glutamate transporter, results in abnormal motor behaviors in developing zebrafish. Dev Biol 362:162-171.

Meng A, Tang H, Ong BA, Farrell MJ, Lin S (1997) Promoter analysis in living zebrafish embryos identifies a cis-acting motif required for neuronal expression of GATA-2. Proc Natl Acad Sci U S A 94:6267-6272.

Middeldorp, J., Hol, E.M., 2011. GFAP in health and disease. Prog Neurobiol 93, 421-443.

Miyamoto, D.T., Perlman, Z.E., Burbank, K.S., Groen, A.C., Mitchison, T.J., 2004. The kinesin Eg5 drives poleward microtubule flux in Xenopus laevis egg extract spindles. J Cell Biol 167, 813-818.

Moro E, Ozhan-Kizil G, Mongera A, Beis D, Wierzbicki C, Young RM, Bournele D, Domenichini A, Valdivia LE, Lum L, Chen C, Amatruda JF, Tiso N, Weidinger G, Argenton F (2012) In vivo Wnt signaling tracing through a transgenic biosensor fish reveals novel activity domains. Dev Biol 366:327-340.

Morshead CM, Garcia AD, Sofroniew MV, van Der Kooy D (2003) The ablation of glial fibrillary acidic protein-positive cells from the adult central nervous system results in the loss of forebrain neural stem cells but not retinal stem cells. Eur J Neurosci 18:76-84.

Mueller T, Wullimann MF (2003) Anatomy of neurogenesis in the early zebrafish brain. Brain Res Dev Brain Res 140:137-155.

Muller, C., Gross, D., Sarli, V., Gartner, M., Giannis, A., Bernhardt, G., Buschauer, A., 2007. Inhibitors of kinesin Eg5: antiproliferative activity of monastrol analogues against human glioblastoma cells. Cancer Chemother Pharmacol 59, 157-164.

Myers, P.Z., Eisen, J.S., Westerfield, M., 1986. Development and axonal outgrowth of identified motoneurons in the zebrafish. J Neurosci 6, 2278-2289.

Noctor SC, Flint AC, Weissman TA, Dammerman RS, Kriegstein AR (2001) Neurons derived from radial glial cells establish radial units in neocortex. Nature 409:714-720.

Noctor, S.C., Flint, A.C., Weissman, T.A., Wong, W.S., Clinton, B.K., Kriegstein, A.R., 2002. Dividing precursor cells of the embryonic cortical ventricular zone have morphological and molecular characteristics of radial glia. J Neurosci 22, 3161-3173.

Nomura H, Kim H, Mothe A, Zahir T, Kulbatski I, Morshead CM, Shoichet MS, Tator CH (2010) Endogenous radial glial cells support regenerating axons after spinal cord transection. Neuroreport 21:871-876.

Ohnuma, S., and Harris, W.A. (2003). Neurogenesis and the cell cycle. Neuron *40*, 199–208.

Okuda Y, Ogura E, Kondoh H, Kamachi Y (2010) B1 SOX coordinate cell specification with patterning and morphogenesis in the early zebrafish embryo. PLoS Genet 6(5):e1000936.

Park, H.C., Mehta, A., Richardson, J.S., Appel, B., 2002. olig2 is required for zebrafish primary motor neuron and oligodendrocyte development. Dev Biol 248, 356-368.

Park HC, Shin J, Appel B (2004) Spatial and temporal regulation of ventral spinal cord precursor specification by Hedgehog signaling. Development 131:5959-5969.

Park, H.C., Shin, J., Roberts, R.K., Appel, B., 2007. An olig2 reporter gene marks oligodendrocyte precursors in the postembryonic spinal cord of zebrafish. Dev Dyn 236, 3402-3407.

Peri F, Nusslein-Volhard C (2008) Live imaging of neuronal degradation by microglia reveals a role for v0-ATPase a1 in phagosomal fusion in vivo. Cell 133:916-927.

Peters, N.T., Kropf, D.L., 2006. Kinesin-5 motors are required for organization of spindle microtubules in Silvetia compressa zygotes. BMC Plant Biol 6, 19.

Peterson, S.M., Freeman, J.L., 2009. RNA isolation from embryonic zebrafish and cDNA synthesis for gene expression analysis. Journal of visualized experiments : JoVE.

Pevny, L.H., and Nicolis, S.K. (2010). Sox2 roles in neural stem cells. The International Journal of Biochemistry & Cell Biology *42*, 421–424.

Pfaff, K.L., Straub, C.T., Chiang, K., Bear, D.M., Zhou, Y., Zon, L.I., 2007. The zebra fish cassiopeia mutant reveals that SIL is required for mitotic spindle organization. Molecular and cellular biology 27, 5887-5897.

Pinto, L., Gotz, M., 2007. Radial glial cell heterogeneity--the source of diverse progeny in the CNS. Prog Neurobiol 83, 2-23.

Pippenger MA, Sims TJ, Gilmore SA (1990) Development of the rat corticospinal tract through an altered glial environment. Brain Res Dev Brain Res 55:43-50.

Pisharath H, Parsons MJ (2009) Nitroreductase-mediated cell ablation in transgenic zebrafish embryos. Methods Mol Biol 546:133-143.

Pisharath H, Rhee JM, Swanson MA, Leach SD, Parsons MJ (2007) Targeted ablation of beta cells in the embryonic zebrafish pancreas using E. coli nitroreductase. Mech Dev 124:218-229.

Ramón y Cajal S (1911) Histologyof the Nervous System of Man and Vertebrates: Oxford University Press.

Raible, D.W., Wood, A., Hodsdon, W., Henion, P.D., Weston, J.A., Eisen, J.S., 1992. Segregation and early dispersal of neural crest cells in the embryonic zebrafish. Dev Dyn 195, 29-42.

Rauch, G.J., Lyons, D.A., Middendorf, I., Friedlander, B., Arana, N., Reyes, T., and Talbot, W.S. (2003) Submission and Curation of Gene Expression Data. ZFIN Direct Data Submission (http://zfin.org).

Reif, A., Fritzen, S., Finger, M., Strobel, A., Lauer, M., Schmitt, A., and Lesch, K.-P. (2006). Neural stem cell proliferation is decreased in schizophrenia, but not in depression. Mol. Psychiatry *11*, 514–522.

Rhodes J, Hagen A, Hsu K, Deng M, Liu TX, Look AT, Kanki JP (2005) Interplay of pu.1 and gata1 determines myelo-erythroid progenitor cell fate in zebrafish. Dev Cell 8:97-108.

Sanai, N., Alvarez-Buylla, A., and Berger, M.S. (2005). Neural Stem Cells and the Origin of Gliomas. New England Journal of Medicine *353*, 811–822.

Sarli, V., Giannis, A., 2006. Inhibitors of mitotic kinesins: next-generation antimitotics. ChemMedChem 1, 293-298.

Sawin, K., Mitchison, T., 1990. Cell biology. Motoring in the spindle. Nature 345, 22-23.

Sawin, K.E., LeGuellec, K., Philippe, M., Mitchison, T.J., 1992. Mitotic spindle organization by a plus-end-directed microtubule motor. Nature 359, 540-543.

Sawin, K.E., Mitchison, T.J., 1991. Poleward microtubule flux mitotic spindles assembled in vitro. J Cell Biol 112, 941-954.

Sawin, K.E., Mitchison, T.J., 1995. Mutations in the kinesin-like protein Eg5 disrupting localization to the mitotic spindle. Proc Natl Acad Sci U S A 92, 4289-4293.

Schmidt, R., Strähle, U., and Scholpp, S. (2013). Neurogenesis in zebrafish - from embryo to adult. Neural Dev *8*, 3.

Seredick SD, Van Ryswyk L, Hutchinson SA, Eisen JS (2012) Zebrafish Mnx proteins specify one motoneuron subtype and suppress acquisition of interneuron characteristics. Neural Dev 7:35.

Sharp, D.J., Yu, K.R., Sisson, J.C., Sullivan, W., Scholey, J.M., 1999. Antagonistic microtubule-sliding motors position mitotic centrosomes in Drosophila early embryos. Nat Cell Biol 1, 51-54.

Shepard, J.L., Amatruda, J.F., Stern, H.M., Subramanian, A., Finkelstein, D., Ziai, J., Finley, K.R., Pfaff, K.L., Hersey, C., Zhou, Y., Barut, B., Freedman, M., Lee, C., Spitsbergen, J., Neuberg, D., Weber, G., Golub, T.R., Glickman, J.N., Kutok, J.L., Aster, J.C., Zon, L.I., 2005. A zebrafish bmyb mutation causes genome instability and increased cancer susceptibility. Proceedings of the National Academy of Sciences of the United States of America 102, 13194-13199.

Shepard, J.L., Stern, H.M., Pfaff, K.L., Amatruda, J.F., 2004. Analysis of the cell cycle in zebrafish embryos. Methods in cell biology 76, 109-125.

Shimizu, Y., Ito, Y., Tanaka, H., and Ohshima, T. (2015). Radial glial cell-specific ablation in the adult Zebrafish brain. Genesis *53*, 431–439.

Shin J, Park HC, Topczewska JM, Mawdsley DJ, Appel B (2003) Neural cell fate analysis in zebrafish using olig2 BAC transgenics. Methods Cell Sci 25:7-14.

Shin, J., Poling, J., Park, H.C., Appel, B., 2007. Notch signaling regulates neural precursor allocation and binary neuronal fate decisions in zebrafish. Development 134, 1911-1920.

Shitamukai, A., Konno, D., Matsuzaki, F., 2011. Oblique radial glial divisions in the developing mouse neocortex induce self-renewing progenitors outside the germinal zone that resemble primate outer subventricular zone progenitors. The Journal of neuroscience : the official journal of the Society for Neuroscience 31, 3683-3695.

Shu T, Li Y, Keller A, Richards LJ (2003a) The glial sling is a migratory population of developing neurons. Development 130:2929-2937.

Shu T, Puche AC, Richards LJ (2003b) Development of midline glial populations at the corticoseptal boundary. J Neurobiol 57:81-94.

Shu T, Richards LJ (2001) Cortical axon guidance by the glial wedge during the development of the corpus callosum. J Neurosci 21:2749-2758.

Sims TJ, Durgun MB, Gilmore SA (1998) Schwann cell invasion of ventral spinal cord: the effect of irradiation on astrocyte barriers. J Neuropathol Exp Neurol 57:866-873.

Smith CJ, Johnson K, Welsh TG, Barresi MJF, Kucenas S (in review) Radial glia inhibit peripheral glial infiltration into the spinal cord at motor exit point transition zones. Journal of Neuroscience.

Sommer, L., Rao, M., 2002. Neural stem cells and regulation of cell number. Progress in neurobiology 66, 1-18.

Song MH, Brown NL, Kuwada JY (2004) The cfy mutation disrupts cell divisions in a stage-dependent manner in zebrafish embryos. Dev Biol (N Y 1985) 276:194-206.

Suter, D.M., Tirefort, D., Julien, S., Krause, K.H., 2009. A Sox1 to Pax6 switch drives neuroectoderm to radial glia progression during differentiation of mouse embryonic stem cells. Stem Cells 27, 49-58.

Takahashi, T., Nowakowski, R.S., Caviness, V.S., Jr., 1995. The cell cycle of the pseudostratified ventricular epithelium of the embryonic murine cerebral wall. The Journal of neuroscience : the official journal of the Society for Neuroscience 15, 6046-6057.

Tanenbaum, M.E., Macurek, L., Janssen, A., Geers, E.F., Alvarez-Fernandez, M., Medema, R.H., 2009. Kif15 cooperates with eg5 to promote bipolar spindle assembly. Current biology : CB 19, 1703-1711.

Tawk, M., Araya, C., Lyons, D.A., Reugels, A.M., Girdler, G.C., Bayley, P.R., Hyde, D.R., Tada, M., Clarke, J.D., 2007. A mirror-symmetric cell division that orchestrates neuroepithelial morphogenesis. Nature 446, 797-800.

Thisse, C., Thisse, B., 2008. High-resolution in situ hybridization to whole-mount zebrafish embryos. Nat Protoc 3, 59-69.

Ullian, E.M., Sapperstein, S.K., Christopherson, K.S., and Barres, B.A. (2001). Control of Synapse Number by Glia. Science *291*, 657–661.

Uzbekov, R., Prigent, C., Arlot-Bonnemains, Y., 1999. Cell cycle analysis and synchronization of the Xenopus laevis XL2 cell line: study of the kinesin related protein XlEg5. Microsc Res Tech 45, 31-42.

Valensin, S., Ghiron, C., Lamanna, C., Kremer, A., Rossi, M., Ferruzzi, P., Nievo, M., Bakker, A., 2009. KIF11 inhibition for glioblastoma treatment: reason to hope or a struggle with the brain? BMC Cancer 9, 196.

Valentine, M.T., Fordyce, P.M., Block, S.M., 2006a. Eg5 steps it up! Cell Div 1, 31.

Valentine, M.T., Fordyce, P.M., Krzysiak, T.C., Gilbert, S.P., Block, S.M., 2006b. Individual dimers of the mitotic kinesin motor Eg5 step processively and support substantial loads in vitro. Nat Cell Biol 8, 470-476.

van Ham TJ, Brady CA, Kalicharan RD, Oosterhof N, Kuipers J, Veenstra-Algra A, Sjollema KA, Peterson RT, Kampinga HH, Giepmans BN (2014) Intravital correlated microscopy reveals differential macrophage and microglial dynamics during resolution of neuroinflammation. Disease models & mechanisms 7:857-869.

van Ham TJ, Mapes J, Kokel D, Peterson RT (2010) Live imaging of apoptotic cells in zebrafish. FASEB J 24:4336-4342.

Verity, C., Firth, H., and Ffrench-Constant, C. (2003). Congenital Abnormalities of the Central Nervous System. J Neurol Neurosurg Psychiatry *74*, i3–i8.

Watters, C., 2006. Video views and reviews: neurulation and the fashioning of the vertebrate central nervous system. CBE Life Sci Educ 5, 99-103.

Westerfield M (2007) The Zebrafish Book, A guide for the laboratory use of zebrafish *(Danio rerio)*. Eugene: University of Oregon Press.

Wilson, P.G., Simmons, R., Saighal, S., 2004. Novel nuclear defects in KLP61F-deficient mutants in Drosophila are partially suppressed by loss of Ncd function. Journal of cell science 117, 4921-4933.

Wu D, Miyamoto O, Shibuya S, Mori S, Norimatsu H, Janjua NA, Itano T (2005) Co-expression of radial glial marker in macrophages/microglia in rat spinal cord contusion injury model. Brain Res 1051:183-188.

Yasui, Y., Amano, M., Nagata, K., Inagaki, N., Nakamura, H., Saya, H., Kaibuchi, K., Inagaki, M., 1998. Roles of Rho-associated kinase in cytokinesis; mutations in Rho-associated kinase phosphorylation sites impair cytokinetic segregation of glial filaments. J Cell Biol 143, 1249-1258.

Yoon, K.J., Koo, B.K., Im, S.K., Jeong, H.W., Ghim, J., Kwon, M.C., Moon, J.S., Miyata, T., Kong, Y.Y., 2008. Mind bomb 1-expressing intermediate progenitors generate notch signaling to maintain radial glial cells. Neuron 58, 519-531.

Zhang, C., Li, Q., Jiang, Y.J., 2007. Zebrafish Mib and Mib2 are mutual E3 ubiquitin ligases with common and specific delta substrates. J Mol Biol 366, 1115-1128.

Zhang SC (2001) Defining glial cells during CNS development. Nat Rev Neurosci 2:840-843.